



FACULTEIT WETENSCHAPPEN

Acoustic Properties of the South Pole Ice for Astrophysical Neutrino Detection

Yasser M. Abdou

Department of Physics and Astronomy, Faculty of Sciences,
Ghent University
Academic year 2011-2012



FACULTEIT WETENSCHAPPEN

Acoustic Properties of the South Pole Ice for Astrophysical Neutrino Detection

Yasser M. Abdou

Promotor: Prof. Dr. Dirk Ryckbosch

Thesis submitted in fulfilment of the requirements for the degree of
Doctor in Sciences: Physics (PhD)

Department of Physics and Astronomy, Faculty of Sciences,
Ghent University
Academic year 2011-2012

In memory of my father

Acknowledgements

First and foremost I would like to express my deepest gratitude to my supervisor Prof. Dirk Ryckbosch for accepting me as a member of his group and giving me a great opportunity to work with IceCube project, the biggest neutrino telescope ever built. It has been an honor to be a Ph.D. student working with him. Thank you, Dirk for all encouragement and support you have given during my study.

Many special thanks for all members of SPATS group who offered a great co-operation, discussion and guidance to establish my work. I have learned much from all of them in many ways and on many levels.

I would like to acknowledge Dr. Julien Bolmont for his co-operation and guidance to use his adapted version of CORSIKA to perform the simulation study which presented in this work. Also, I would like to thank Dr. Tanguy Pierog, Dr. Dieter Heck and Dr. Johannes Knapp, the developer of the original version of CORSIKA, for their co-operation and patience which make me familiar with CORSIKA and be able to use it as it was needed to perform the simulation work.

I also want to warmly thank all the members of the Department of Physics and Astronomy at Ghent University. I have spent a very pleasant time during my study with all of you. It was very interesting to meet cool, funny and interesting people. Special thanks to IceCube mates for their encouragement and helpful discussions during my study and those from other experiments with whom I did not work, but shared nice moments at Monday morning meetings and annual group meetings.

I would like to acknowledge Dr. Michael Carson, I appreciate all his time, ideas and discussion during my study to make this work visible. Also, I would like to thank him for his valuable suggestions he gave to me while reading my thesis.

Special thanks goes to my office mate Dr. Michael Tytgat for his patience, encouragement, understanding and reading Dutch letters, frequently.

I would like to thank all of my Egyptian friends at Ghent university and other friends from different nationalities for their friendship and assistance. Special thanks to Dr. Khaled Mostafa who welcomed and guided me to establish my new life in the beginning.

My heartfelt gratitude to my parents, sister and brothers for their endless encouragements, support and patience.

Special warm thanks to my beloved wife (Shereen) and my sweet kids (Mohamed and Kenzie) for their unending love, support and understanding during all the years of my study.

I would also like to thank the members of the exam committee for their guidance, reading and suggestions to improve this thesis.

Bedankt allemaal,

Yasser

Contents

List of Figures	vii
List of Tables	xi
Introduction	1
1 Cosmic Rays and Astrophysical Neutrinos	3
1.1 High energy cosmic rays	3
1.2 Acceleration mechanism	5
1.3 Neutrino Astronomy	7
1.3.1 Neutrino production	7
1.3.2 GZK Cut-off	8
1.3.3 Cosmogenic neutrino flux	9
1.3.4 Possible astrophysical neutrino sources	14
1.3.5 Current neutrino flux limits	17
2 Ultra High Energy Neutrino Detection	21
2.1 Deep Inelastic Scattering	21
2.2 Cascades	22
2.2.1 Electromagnetic cascade	23
2.2.2 Hadronic cascade	23
2.2.3 LPM effect	23
2.3 Neutrino detection methods	24
2.3.1 Optical neutrino detectors	26
2.3.2 Radio neutrino detectors	28
2.3.3 Acoustic neutrino detectors	32
2.4 SPATS and the retrievable transmitter	34
2.4.1 Geometry	34
2.4.2 Hardware	34
2.4.3 Retrievable transmitter (Pinger)	37
2.4.4 Recent SPATS results	41
3 Acoustic Neutrino Detection	45
3.1 Thermo-acoustic model	45
3.2 Acoustic signal production	50
3.2.1 Acoustic signal properties	51
3.3 Ice properties	52
3.3.1 Sound speed	54
3.3.2 Refraction	56
3.3.3 Ambient noise	56
3.3.4 Acoustic signal propagation	57

4	Pinger data analysis	63
4.1	Geometry	63
4.1.1	Depth Measurements	64
4.2	Laboratory tests	65
4.3	Data acquisition	66
4.4	Systematic effects	66
4.5	Data processing	70
4.5.1	Clock-drift correction	70
4.5.2	Averaging	72
4.6	Data Quality: expected signal	72
4.7	Attenuation analysis	73
4.7.1	Data set selection	73
4.7.2	Fitting	75
4.7.3	Attenuation frequency dependence	76
4.7.4	Attenuation results	78
4.8	Sound speed measurements	84
4.8.1	Frequency dependent results	86
4.8.2	Ice fabric results	89
4.9	Conclusion	92
5	Simulating the Acoustic Signal from Neutrino Interactions	93
5.1	Propagation and interaction of UHE neutrinos	93
5.2	Modified CORSIKA in water/ice	94
5.3	Neutrino induced cascades in ice	97
5.3.1	ACORNE parameterisation	98
5.3.2	Shower properties in ice	100
5.3.3	Longitudinal shower distribution	100
5.3.4	Radial shower distribution	102
5.4	Acoustic signal	103
5.4.1	Generation	103
5.4.2	Attenuation	107
5.4.3	Distance dependence	109
5.4.4	Angular dependence	112
5.5	Large acoustic neutrino detector simulation	113
5.5.1	Effective volume and GZK fluxes	116
5.6	Conclusion	118
6	Discussion and outlook	121
A	Discrete Fourier Transform	125
A.1	Basic equations	125
A.2	Continuous Fourier Transform	125
A.3	Discrete Fourier Transform	126

A.4 Power Spectral Density	126
A.5 Relation between PSD and Signal RMS	127
B Attenuation fit	129
C Simulation results	133
C.1 Longitudinal profile	133
C.2 Radial profile	134
Bibliography	137

List of Figures

1.1	Cosmic ray spectrum for all particles.	4
1.2	Updated Hillas (1984) diagram.	6
1.3	Energy loss lengths for UHE protons propagating through the universe.	9
1.4	Development of the proton energy with the travelled distance.	10
1.5	Observation of cut-off on cosmic ray spectrum.	11
1.6	The GZK neutrino flux.	13
1.7	Different GZK flux models.	14
1.8	Unified scheme of the probable mechanism powering AGNs and GRBs.	15
1.9	Unified model of AGN.	16
1.10	The fireball shock model for GRBs.	17
1.11	Observational neutrino limits from IceCube-40.	18
1.12	Observational neutrino limits from acoustic and radio experiments.	19
2.1	The total νN cross-section at high energy.	22
2.2	Cherenkov light patterns.	25
2.3	The IceCube detector.	27
2.4	Schematic of the ANITA concept for UHE neutrino detection.	29
2.5	ANITA-II neutrino flux limits.	30
2.6	Geometry of lunar neutrino cascade event detection.	31
2.7	Schematic of the SPATS array.	35
2.8	The SPATS geometry.	36
2.9	SPATS stage.	38
2.10	The pinger setup: view of the pinger stage and pinger in hole.	40
2.11	Sound speed for both pressure and shear waves.	42
2.12	The transient events recorded by SPATS.	44
3.1	Schematic drawing of neutrino-induced cascade.	47
3.2	Sound waves in solids.	48
3.3	The acoustic bipolar pulse in water and ice.	51
3.4	The phase diagram of water and crystal structure of ice-Ih.	53
3.5	Glacier ice crystal structure at different depths.	53
3.6	Density and temperature profiles of the South Pole ice cap.	54
3.7	Pressure waves profile and their ray trajectories in South Pole ice cap.	55
3.8	Sound speed vs the propagation angle relative the c-axis	56
3.9	Absorption in South Pole ice.	58
3.10	Absorption and scattering in South Pole ice.	59
4.1	The SeaStar and RW payout depth measurements for pinger hole 16.	65
4.2	Acoustic signal studies in the laboratory.	67

4.3	An example of a Clockdrift corrected average waveform	68
4.4	The IRIG-B 100 pps timing signal.	71
4.5	Clock drift correction and waveform averaging.	72
4.6	Waveforms recorded by the same channel from different pinger holes.	74
4.7	Power spectra for signal, noise and noise-subtracted signal.	77
4.8	The distribution of the reduced chi-square χ^2/ndf of all fits.	80
4.9	Example for the fit on the data to obtain the attenuation coefficient.	81
4.10	Attenuation coefficient and corresponding error at 30 kHz.	81
4.11	Attenuation coefficient and corresponding error at 45 kHz.	82
4.12	Attenuation coefficient depth dependence.	82
4.13	The weighted mean for attenuation coefficients vs. depth.	83
4.14	Contribution to scattering due to grain boundaries.	83
4.15	Zoom on for the beginning of a 30 kHz pulse.	85
4.16	Sound speed at depth 250 m.	87
4.17	Sound speed at depth 320 m	88
4.18	Sound speed at different frequencies	89
4.19	Measured sound speed compared to the previous measurements.	90
4.20	Schematic diagram for the pinger at 540 m and string C.	91
4.21	sound speed vs different angles	91
5.1	The inelasticity for ν and $\bar{\nu}$ for different neutrino energies.	94
5.2	Startup widow for CORSIKA-IW.	96
5.3	Average longitudinal profile for CORSIKA and GEANT4.	96
5.4	The energy density deposited by hadronic shower, using π^+ , in ice.	100
5.5	Longitudinal shower parameters.	101
5.6	Averaged longitudinal energy deposited for 100 showers.	102
5.7	Shower peak depth versus energy.	103
5.8	The averaged radial energy distribution at different depths.	104
5.9	A schematic view of the deposited energy from the hadronic cascade.	105
5.10	Sketch showing the integration from different shower portions.	106
5.11	Pressure pulse generation.	107
5.12	The acoustic pressure amplitude at the source.	108
5.13	The acoustic pressure signal at 1 km from the source.	109
5.14	Maximum pressure signal amplitude and its asymmetry vs distance.	110
5.15	Pressure signal amplitude and its frequency composition.	110
5.16	Median frequency for the acoustic signal versus distance.	111
5.17	The maximum and minimum pulse heights versus energy.	111
5.18	The angular variation of the peak signal amplitude and its a symmetry.	112
5.19	Pressure signal amplitude spread and its frequency composition.	113
5.20	Median frequency for the acoustic signal versus angle.	114
5.21	The attenuated acoustic signal amplitude versus distance.	115
5.22	Detection range as a function of the neutrino energy.	115
5.23	Detected events versus energy as a function of the ASM density.	117

5.24 Effective volume versus energy as a function of the ASM density. 117
5.25 The updated neutrino flux models. 119

List of Tables

2.1	Deployment details for SPATS.	37
3.1	Grüneisen parameter γ_G for ocean-water, ice and salt.	50
4.1	Horizontal distances between pinger holes and SPATS strings.	63
4.2	Stops for different pinger holes.	63
4.3	Nominal and measured stopping depths for Hole 16.	65
4.4	Azimuthal spread of the pinger holes.	73
4.5	Sound speed at different frequencies.	86
4.6	Sound speed directional dependence.	92
5.1	The expected total number of GZK neutrinos per 1 yr for 1 km ³ detector. .	118

Introduction

Neutrinos belong to a family of particles called “leptons” (from the Greek word leptos, meaning small or fine) and are denoted by the Greek letter (ν). They were first postulated in 1930 by Wolfgang Pauli to explain why energy and momentum conservation seemed to be violated in β -decay. They were first observed in 1956 by Reines and Cowan, using antineutrinos from a nuclear reactor at Savannah River, North Carolina [1]. Later it was discovered that there are three kinds (flavors) of neutrinos: the electron neutrino (ν_e), the muon neutrino (ν_μ) and the tau neutrino (ν_τ). The neutrino is an electrically neutral, weakly interacting elementary particle with a half-integer spin and has almost zero mass. It is able to pass through ordinary matter almost unaffected.

Astroparticle physics studies elementary particles of astronomical origin (e.g. cosmic rays, γ -rays and neutrinos) to get information about their origin and how they are accelerated. Whereas charged particles are deflected by magnetic fields, and photons are absorbed by interstellar matter and softened by radiation fields, the neutrino traverses the cosmos retaining its energy and directionality until it eventually undergoes a collision far away from its place of origin. The neutrino cross section is very small [2] compared to that for photons or charged cosmic rays, thus its mean free path length is much higher and it can therefore travel, virtually unimpeded, from more distant sources. On the other hand, a large volume of target material is required to get a reasonable number of detectable neutrino interactions.

The expected astrophysical neutrino flux is very low and is steeply falling with energy, thus a very large instrumented volume is necessary in order to detect a significant amount of neutrinos. Natural resources like the oceans and the Antarctic ice sheet are used as a detection medium. Currently, there are several neutrino experiments (e.g. ANTARES and IceCube) optimized to detect “ultra high energy” (UHE) neutrinos in the energy range ($10^{12} - 10^{17}$ eV) from distant astrophysical sources. The IceCube detector is not large enough to detect “extremely high energy” (EHE) neutrinos above 10^{17} eV, where the neutrino rate is less than 1 neutrino/km³/yr. Therefore, a detection volume of the order of 10-100 km³ is required to detect the EHE neutrinos.

The South Pole ice as a medium is predicted to be well suited for neutrino detection. The neutrino interacts with ice and produces three detectable signals: optical, radio and acoustic. The number of detectors that are required to build such a very large volume neutrino telescope depends on the attenuation length of the observable signal that is generated by the neutrino interaction with the medium. The optical attenuation length is measured to be about 100 m in South Pole ice, while it is expected to be larger for both acoustic and radio signals [3]. Using the acoustic/radio technique could help to enlarge the detector volume at a reasonable cost.

The acoustic technique is based on the thermo-acoustic effect. When a neutrino interacts, it produces a lepton and a hadronic cascade which gives rise to a large energy deposition in a small volume in a very short time. The volume is overheated and the

medium around it expands, which gives rise to a pressure signal in the plane perpendicular to the shower axis and therefore the incident neutrino direction. The South Pole Acoustic Test Setup (SPATS) was deployed in January 2007 at the South Pole to measure (or to constrain) the South Pole ice acoustic properties in the 10 to 100 kHz region. A measurement of these parameters will allow us to obtain a realistic sensitivity estimate for a possible future acoustic neutrino telescope in the Antarctic ice. SPATS was capable of measuring the acoustic attenuation length, sound speed profile, noise floor, and transient noise sources in situ at the South Pole.

The acoustic attenuation length of the Antarctic ice is a fundamental quantity to design a future acoustic neutrino detector at the South Pole. The longitudinal waves in the South Pole ice are expected to be attenuated via absorption and scattering [4], where the attenuation due to scattering depends on the frequency ($\approx f^4$). In this work, recent measurements from SPATS will be used to investigate the frequency dependence of sound in the South Pole ice. This will allow us to distinguish between the two different attenuation mechanisms (absorption or scattering). Further, this information will be used to calculate expected event rates of GZK neutrinos in a future, large-scale, acoustic detector.

The thesis is structured as follows. Chapter 1 gives a short overview of cosmic ray physics and the production mechanism of high-energy astrophysical neutrinos. The expected fluxes, as well as current observational limits are described. In chapter 2, the interaction of UHE neutrinos with a dense medium and possible detection methods are given. An overview of the SPATS array is presented. In chapter 3, the thermo-acoustic mechanism and the acoustic pressure pulse properties are introduced. Also, the acoustic ice properties are presented. In chapter 4, the frequency dependent acoustic attenuation length is determined from in-situ measurements with SPATS, using a retrievable transmitter (pinger). Further, frequency dependent studies of sound speed and the ice fabric at the South Pole are performed. In chapter 5, the in-situ measured attenuation length is used to perform a simulation study for the neutrino induced cascades and the acoustic signal in ice. Further studies have been done to check the feasibility of an acoustic neutrino telescope in the South Pole ice and to derive its detection rate to a diffuse flux of neutrinos. Finally, a discussion and outlook are presented in Chapter 6.

Cosmic Rays and Astrophysical Neutrinos

In this chapter, an overview is given about cosmic rays and the astrophysical neutrinos. First, the composition of cosmic ray spectrum, its features and different acceleration mechanism models are discussed. Then, the GZK cut-off of cosmic rays and astrophysical neutrinos source candidates are explained. Some of the neutrino flux models are explained and finally the neutrino current flux limits that predicted by many experiments are shown.

1.1 High energy cosmic rays

Each second, streams of relativistic particles (protons, electrons, α -particles, and heavier nuclei) hit the atmosphere. These particles have relatively high energies and range over many orders of magnitude, while the Earth's magnetic field shields the atmosphere from the low-energy charged particles mainly from the Sun. Not all of these particles can reach the Earth's surface: most of them interact with air molecules and create a cascade of many of secondary particles (ionizing particles and electromagnetic radiation) which we call an "air shower". Experimentally, cosmic rays are observed via induced air showers by using a large surface array using different techniques [5]. Even 100 years after the discovery of cosmic rays, questions regarding the nature, the origin and acceleration mechanism are still unanswered.

To understand the nature of cosmic rays, the flux, the shape of the energy spectrum and the composition of these high-energy particles were measured experimentally. It has been found that the main component is charged nuclei ranging from protons to the heaviest stable elements, but also electrons, positrons, anti-protons and gamma-rays have been identified. So far, the only two detected sources of astrophysical neutrinos ν are the sun and the supernova explosion SN1987A [6].

The flux of cosmic rays has been studied in detail over an enormous range of energies. Fig. 1.1 shows the differential energy spectrum of cosmic rays. It follows a power-law:

$$\frac{dN}{dE} \sim E^\gamma \quad (1.1)$$

where $\frac{dN}{dE}$ is the differential flux, γ is the spectral index and E is the particle energy. The differential energy spectrum of cosmic rays was observed over more than 12 orders of magnitude in energy and has two spectral breaks, called the "knee" at around $3 \cdot 10^{15}$ eV and the "ankle" at around 10^{19} eV. The spectral breaks probably point to different classes

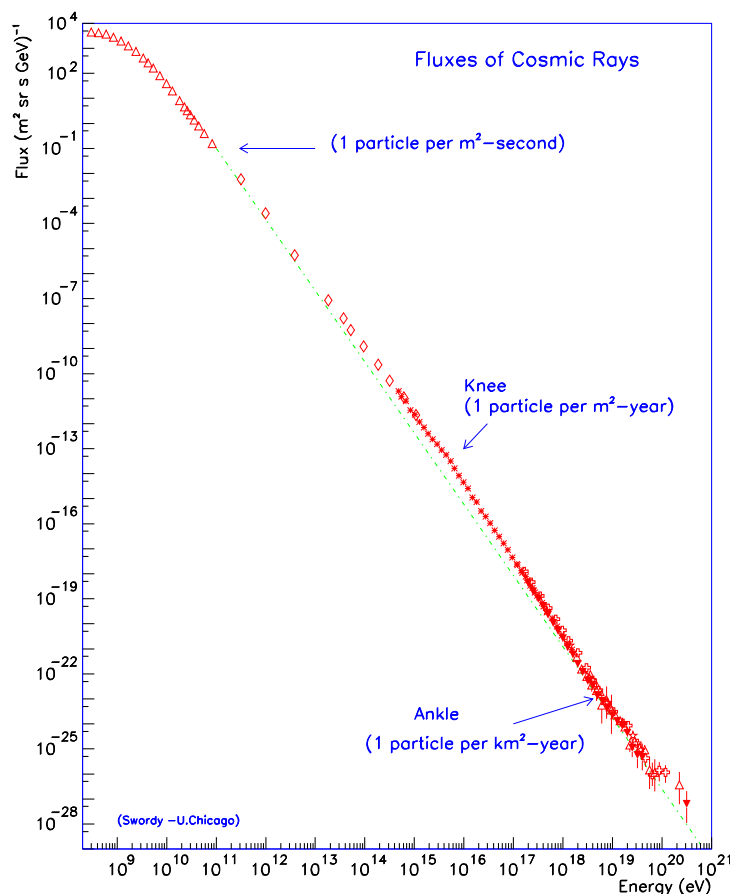


Figure 1.1: Observed energy spectrum of cosmic rays for all particles. A power law spectrum represents the data very well, from [7].

of sources. The low energy cosmic ray flux, up to few TeV, is very high and follows $\gamma = -2.7$. The flux is composed of ionized atomic nuclei with relative amounts similar to those found in the solar system, but accelerated to very high energies. Around the knee, γ changes from -2.7 to -3.1 . Only 1 particle per m^2 per year is observed. Going to higher energies, around the ankle, γ changes again to -2.7 . The event rate is reduced to 1 cosmic ray per km^2 per year.

Cosmic rays below the knee are thought to be of galactic origin from galactic supernovae [8]. Cosmic rays above the ankle are thought to be of extra-galactic origin because the galactic magnetic fields are not sufficient to contain particles of these energies within the galaxy. There are no known galactic phenomena which could accelerate particles to these energies. The exact origin of these particles is unknown. At around $6 \cdot 10^{19}$ eV, protons have sufficient energy to interact with the Cosmic Microwave Background (CMB) and produce a Δ -resonance. This then decays into pions, leading to a suppression in

the cosmic ray spectrum above this energy. This is called the Greisen-Zatsepin-Kuzmin (GZK) cut-off [9, 10]. This suppression of the flux, compared to power law extrapolations, has recently been observed by air shower experiments [11, 12].

In general, almost all the observed charged cosmic rays consist of 90% protons, 9% helium nuclei (α -particles) and 1% heavier nuclei, electrons, positrons or antiprotons [8].

1.2 Acceleration mechanism

Mechanisms for accelerating particles to high energies are presently not exactly identified. Principally, models can be divided into two classes:

- **”bottom-up” models:**

Energetic cosmic-ray (protons and nuclei) are accelerated within galactic and/or extragalactic astrophysical engines (e.g. regions of intense magnetic fields). These engines could have galactic origin such as Supernova Remnants (SNRs), or have extragalactic origin, such as Gamma-Ray Bursts (GRBs), active galactic nuclei (AGN) and Galaxy Clusters. Expected flux of charged cosmic rays, neutrinos, and photons are produced.

There are two possible acceleration models, postulated by Fermi, called Fermi-acceleration [13]. In first-order Fermi-acceleration, particles are accelerated by a large, planar shock front which is moving at a velocity v . The fractional energy gain is proportional to $\beta = v/c$. In second-order Fermi-acceleration, particles are accelerated by a moving gas cloud, and the fractional energy gain is proportional to β^2 . The mechanism of Fermi-acceleration is thought to be responsible for accelerating cosmic ray particles and it is capable of explaining the observed power-law spectrum [13, 14].

First-order Fermi-acceleration at shock fronts in supernova blast waves is thought to be responsible for accelerating the bulk of the cosmic rays up to the knee, and it is also a possible mechanism for accelerating very high energy protons and electrons in GRB and AGN. In this mechanism charged cosmic rays are elastically scattered on magnetic fields back and forth across a shock front and are thereby accelerated. In the generic case, Fermi-acceleration yields a spectral index close to 2. However for most realistic calculations the resulting spectrum is steeper, with $\gamma = 2.1 - 2.4$ [8].

However, this mechanism will only work as long as the particle is trapped within the accelerating area where it gains its energy before leaving the accelerator. The particle is accelerated by the electric field and confined by the magnetic one. This geometrical criterion is expressed in terms of the particle’s Larmor radius r_L which should not exceed the linear size of the accelerator. When the particle’s Larmor radius r_L exceeds the linear size of the accelerator, the particle will leave the accel-

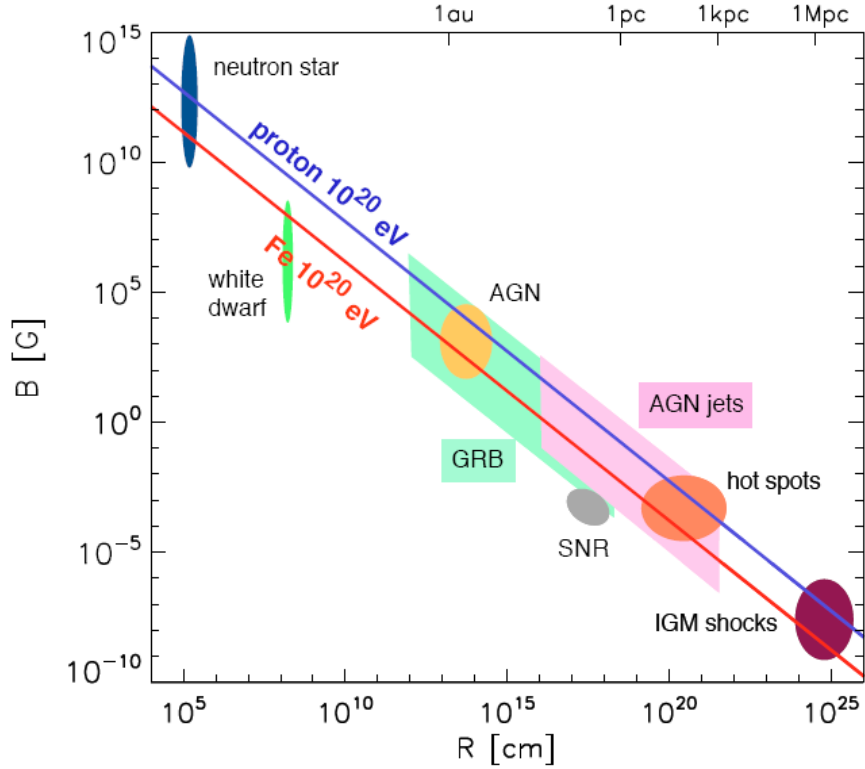


Figure 1.2: Updated Hillas (1984) diagram. Size and magnetic field strength of possible astrophysical particle accelerators. The most powerful candidate sources are shown with the uncertainties in their parameters. From [15].

eration area with maximum energy E_{\max} [5]:

$$E_{\max} \sim 2\beta cZe\mathcal{B}r_L, \quad (1.2)$$

where \mathcal{B} is the magnetic field, βc is the characteristic velocity of the scattering centres (shock fronts, magnetised clouds, etc.) and Ze is the charge of the cosmic ray.

Fig. 1.2 shows the size and magnetic field strength of possible accelerators for cosmic ray energies above 10^{20} eV. Objects that lie below the blue (red) line do not fulfill the condition of Eq. 1.2 and can not accelerate protons (iron nuclei) to 10^{20} eV. Above the blue (red) line protons (iron nuclei) can be confined to a maximum energy of $E_{\max} = 10^{20}$ eV.

- **”top-down” models:**

In these models, cosmic rays are produced as secondaries in the decay of heavy particles (from bottom-up models). The high-energy cosmic rays are actually the stable decay products of supermassive X-particles, called ”exotics”. Such particles

are associated with spontaneous symmetry breaking and could either be remnants of the early universe or have as their source topological defects left over from phase transitions in the early universe (e.g. magnetic monopoles). Generally, when the exotic particle decays, its energy is split and gives the observed flux.

Primary cosmic rays propagate through the interstellar medium and produce secondary cosmic rays. A certain fraction of the cosmic rays hits the Earth atmosphere. The composition of cosmic ray flux varies according to which part of the energy spectrum is observed. The composition of cosmic rays is dependent upon the mechanisms of cosmic ray production, acceleration, and propagation.

1.3 Neutrino Astronomy

Neutrino is neutral and only interact weakly, so that it is considered to be the ideal astrophysical messenger. It can not be deflected by the electromagnetic fields, unlike charged cosmic rays. It can not be absorbed by astrophysical bodies as photons or charged cosmic rays. Therefore, it gives a complementary information about the cosmos and its astrophysical objects without losing directional information or energy.

1.3.1 Neutrino production

High-energy neutrinos are expected to be products of decays and/or interactions of previously accelerated high-energy charged cosmic ray particles. In principle, there are two different acceleration mechanisms, leptonic and hadronic. Electrons and hadrons can be accelerated by astrophysical objects in, respectively, leptonic and hadronic accelerators. The neutrinos are produced only in hadronic accelerators. The Fermi-accelerated protons interact with ambient matter or photons in and around the source. These interactions can be divided into two types: proton-proton (p-p) and proton-photon (p- γ) interactions. The products of these reactions are:

$$p + \gamma \rightarrow \Delta^+ \rightarrow \begin{cases} p + \pi^0(2/3), \\ n + \pi^+(1/3) \end{cases} \quad (1.3)$$

$$p + p \rightarrow \begin{cases} p + p + \pi^0(2/3) \\ p + n + \pi^+(1/3) \end{cases} \quad (1.4)$$

The neutral mesons decay into photons:

$$\pi^0 \rightarrow \gamma + \gamma \quad (1.5)$$

The decay of neutral pions produces potential observable γ -rays. Therefore γ -ray sources are considered as potential sources of high energy neutrinos. Charged mesons decay into, among others, neutrinos:

$$\pi^+ \rightarrow \nu_\mu + \mu^+, \quad \mu^+ \rightarrow \bar{\nu}_\mu + \nu_e + e^+, \quad (1.6)$$

$$\pi^- \rightarrow \bar{\nu}_\mu + \mu^-, \quad \mu^- \rightarrow \nu_\mu + \bar{\nu}_e + e^- \quad (1.7)$$

If the neutrons decay before interacting, it will produce an extra flux of $\bar{\nu}_e$:

$$n \rightarrow p + e^- + \bar{\nu}_e. \quad (1.8)$$

Short lived mesons are predicted to be produced among the resulting particles of Δ^+ decay. These mesons are mainly pions and a lesser extent kaons. The ratio of charged to neutral pions is 1 : 2. The decay of charged pions and kaons produces muons, which in turn leads to a flux of neutrinos (and antineutrinos). The initial neutrino flavour ratio at the source, $(\phi_{\nu_e}:\phi_{\nu_\mu}:\phi_{\nu_\tau})$ is nearly 1:2:0. Such a flux ratio results from an implicit assumption that the muon decays into neutrinos before it loses a significant fraction of its energy, however this ration depends on the neutrinos energy and hence on their production scenario [16]. Tau neutrinos are not produced in astrophysical sources, but the detected flavour composition at Earth will be different due to neutrino oscillation. The neutrino mixing angles predict that the three neutrino flavours should be observed in equal numbers at Earth for neutrinos from astrophysical sources [17], $\phi_{\nu_e} : \phi_{\nu_\mu} : \phi_{\nu_\tau} = 1 : 1 : 1$.

1.3.2 GZK Cut-off

Shortly after the discovery of the CMB in 1965 [18], a theoretical limit to the high-energy tail of the spectrum ($> 5 \cdot 10^{19}$ eV) was predicted in the mid-60s, independently by both Greisen [9] and Zatsepin and Kuz'min [10]. This is the so-called GZK cut-off of the cosmic ray spectrum. This cut-off is expected due to the energy loss of cosmic rays by photo-pion production processes in the interaction with the CMB [19], Eq. 1.3.

The energy threshold for the Δ^+ -resonance is $E_{\text{th}}^\Delta = 5 \cdot 10^{19}$ eV. Therefore this mechanism is significant for cosmic rays with energies above this threshold. The CMB is opaque for the highest cosmic-ray energies and their flux is attenuated with traveling distance. Figure 1.3 shows the energy loss length (the propagation length before the energy is decreased by a factor of $1/e$) of UHE protons as a function of their energy. Another process called the Bethe-Heitler (BH) e^+e^- pair production, $p + \gamma_{\text{CMB}} \rightarrow p + e^+ + e^-$, is shown. The energy threshold for BH pair production is $E_{\text{th}}^{\text{BH}} = 5 \cdot 10^{18}$ eV and it is the main contribution to the energy loss below E_{th}^Δ , after which the Δ^+ -resonance becomes dominant and leads to the GZK cut-off. The effect from the Hubble expansion (redshift)¹ is also shown.

¹The propagation of CRs will be affected by the cosmological evolution for sources at large redshift. This leads to a redshift energy loss.

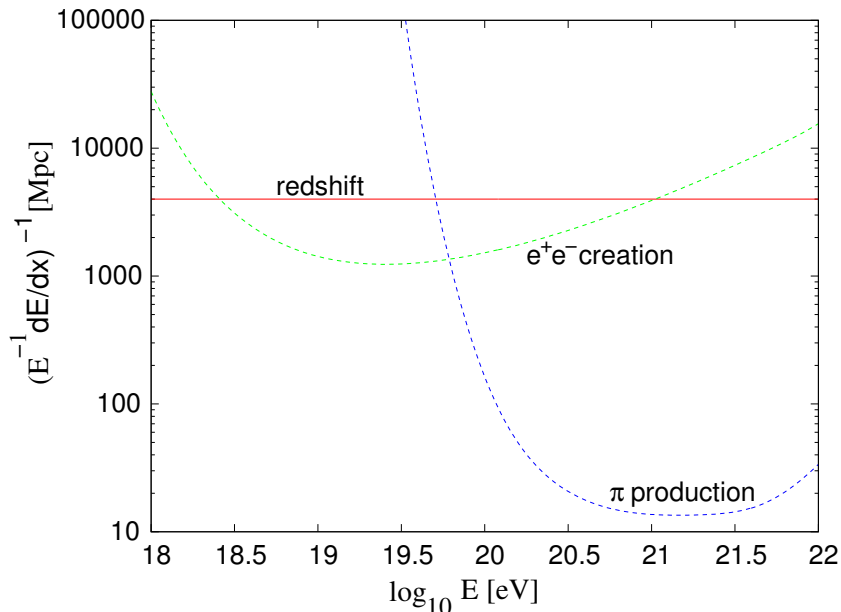


Figure 1.3: The energy loss length for UHE protons propagating through the Universe, due to e^+e^- creation and pion production. The effect from the Hubble expansion (redshift) is also drawn. From [19].

High energy heavy element (e.g. iron) cosmic rays interact with the CMB via photo-disintegration [20] to produce lighter elements. The energy of the primary cosmic ray is shared between multiple nucleons and thus reduces the flux at the highest energies. In each photo-disintegration interaction, a proton is produced (neutrons are produced too but decay relatively fast into protons). As shown in fig. 1.4, the energy of a cosmic ray proton starting with 10^{22} , 10^{21} and 10^{20} eV, respectively, is calculated after a certain propagation distance. The interaction cross section is larger for higher energies. After having traveled a distance of ~ 100 Mpc all protons end up with the same energy ($\sim 5 \times 10^{19}$ eV [21]).

The confirmation of the GZK cut-off increases our confidence that the GZK mechanism is a "guaranteed" source of EHE neutrinos. The GZK cut-off was confirmed by recent observations from the Pierre Auger Observatory [11] and the HiRes experiment [12], as shown in Fig. 1.5(a).

The expected GZK neutrino flux varies with cosmic ray composition. The elementary composition was measured around 10^{19} eV by the Pierre Auger Observatory and the HiRes experiment, as shown in Fig. 1.5(b). The HiRes data is consistent with a proton-dominated composition, while the Auger data favors a transition towards a heavier dominated composition (iron-like) [22].

1.3.3 Cosmogenic neutrino flux

Cosmogenic neutrinos are produced by the decay of charged pions generated by photo-pion production of propagating protons with CMB photons. These neutrinos reach the

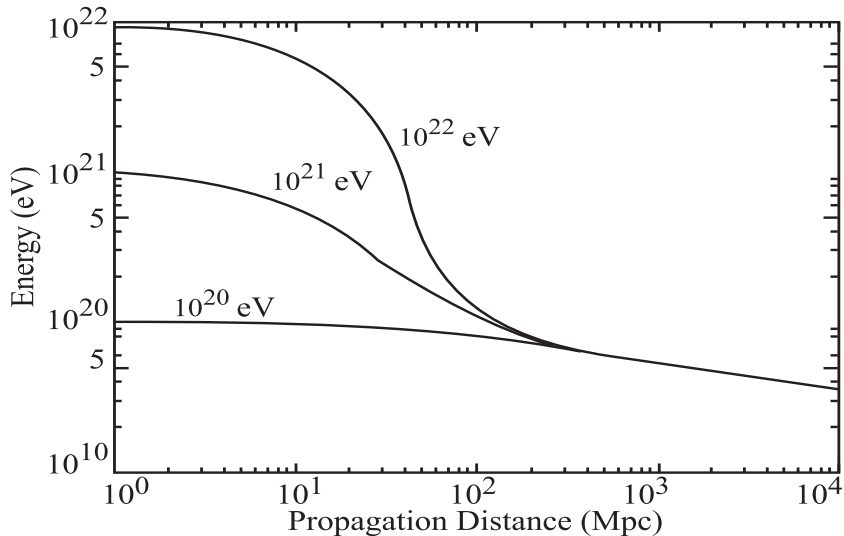


Figure 1.4: The development of the proton energy with the travelled distance for different initial energies. From [21].

Earth with energies around 10^{18} eV, and their interactions with matter can be measured using different experiments (e.g. Auger, IceCube).

Many attempts were made to calculate the expected neutrino fluxes from the GZK mechanism; a brief historical review is given in ref [23]. The different models predict fluxes which vary by more than an order of magnitude [24, 25]. These variations are due to the choice of the injected energy spectrum, the composition of the primaries, the cross sections involved, the CMB photon density, the magnetic field strength, the effect of neutrino oscillations and the cosmological evolution of the sources.

The models can be classified into two categories depending on the production mechanism, "top-down" models and "bottom-up" models. In the top-down models, the cosmic rays are produced by the decay of heavy exotic particle with a higher energy. The topological defects model [26] is one of the popular models belongs the top-down models. According to the top-down model, the very massive (GUT-scale²) unknown particles decay and generate the observed cosmic rays above the GZK-cut-off energy. These unknown particles themselves are remnants of the early Universe (e.g. magnetic monopoles) [26]. Signatures for a cosmic flux of such topological defects, namely magnetic monopoles, are discussed in [26]. Another popular model is the Z -burst model which is based upon the interaction of ultra-high energy neutrinos ($E_\nu > 10^{21}$ eV) with the relic neutrino background (which is analogous to the CMB or may consist of super-heavy relic neutrinos) and generate Z -bosons ($\bar{\nu} + \nu \rightarrow Z$) which decay into a local flux of nucleons, pions, photons and neutrinos [27]. The originally incident high-energy neutrinos could be produced in cascades from proton-interactions in high redshift sources. Both topological defects and Z -burst models are disfavored by the present observations.

²The GUT-scale is the energy scale for the Grand Unified Theory, around 10^{23} eV.

1.3. Neutrino Astronomy

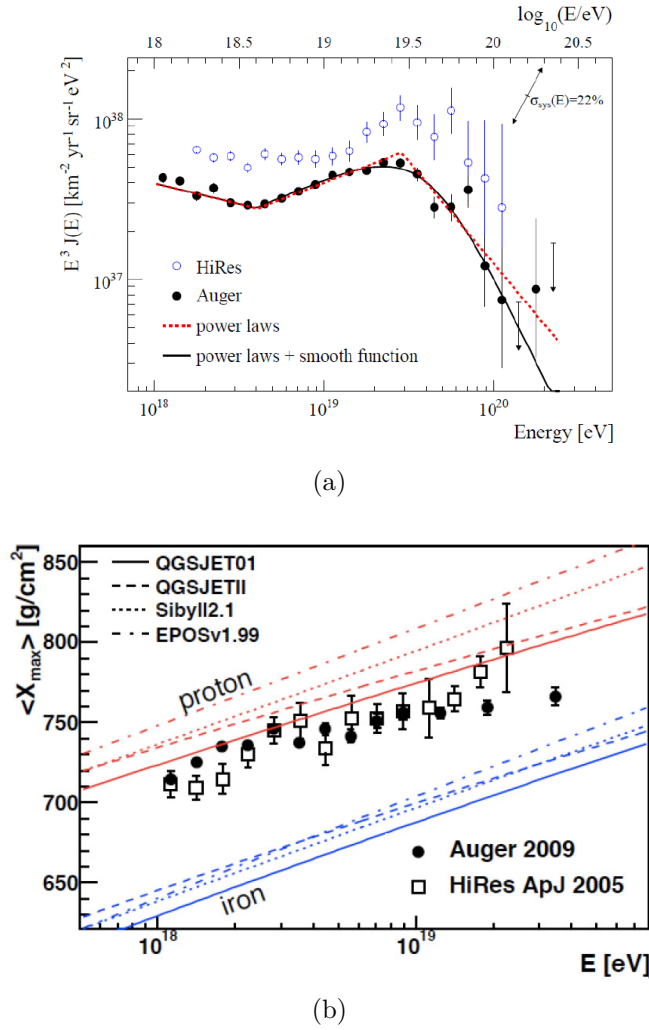


Figure 1.5: (a) The cosmic-ray energy spectrum at high energies observed by the Pierre Auger Observatory and the HiRes instrument. The spectrum is multiplied with E^{-3} to accentuate the cut-off at high energies which is predicted by the GZK effect. From [11]. (b) Measurement of the shower maximum X_{max} in comparison with theoretical predictions from various particle interaction models, indicating a transition to a heavy composition at high energies for the Auger data. From [22].

In the bottom-up models, the flux of neutrinos is expected to accompany the flux of ultra-high-energy cosmic rays as a result of the interaction of accelerated hadrons. The best known models are the Engel, Seckel, and Stanev (ESS) model [23], the Waxman-Bahcall (WB) model [24], and the Mannheim-Protheroe-Rachen (MPR) model [28].

In this model only a fraction of the primary proton energy is transferred to neutrinos independent of the energy of the proton. Where 20% of the primary proton energy is equally distributed to the pion decay products, this leads to $E_\nu \sim 0.05E_p$. The flux from

a single emitting source follows the proton injection spectrum is given by:

$$\frac{dN}{dE} \sim E^{-\gamma} \times \exp(-E/E_c), \quad (1.9)$$

where $\gamma = 2$ unless otherwise stated and E_c is the cut-off energy $\sim 10^{21.5}$ eV.

The ESS model assumes a uniform distribution of sources with a power law cosmic ray injection spectrum with spectral index between 1.8 and 2.7, and a cut-off energy $\sim 10^{21.5}$ eV, and energy scaling due to redshift and the expansion of the universe. Fig. 1.6(a) shows the predicted neutrino flux as a function of the energy for different proton propagation lengths as derived in the ESS model.

Since neutrinos get a fixed percentage of the proton energy, the predicted neutrino flux spectrum shifts to lower energy than the GZK cut-off. The muon neutrino spectrum peaks at $\sim 10^{18.5}$ eV. The electron neutrino spectrum has a double-peak shape. The higher peak, containing mostly ν_e , coincides with the muon neutrino one. The lower energy peak at $10^{16.5}$ eV contains only $\bar{\nu}_e$ from neutron decay, see Eq. 1.8.

The predicted neutrino flux depends on the cosmological source evolution and the strength of the magnetic field which affect the primaries propagation pattern and therefore their flux at Earth. Another important factor is the injection spectrum of UHE cosmic ray. Generally, a primary cosmic ray has to be accelerated to energies above 10^{20} eV to generate significant neutrino fluxes from their propagation. If a substantial fraction of the cosmic-ray primaries are heavy nuclei, the flux of these primaries at high energies is reduced by photo-dissociation. Therefore, the number of particles available for the GZK mechanism is lower than in the case of a pure proton composition, leading to a smaller contribution to the neutrino flux. The expected GZK neutrino flux has been calculated for various heavy nuclei [29]. As shown in Fig. 1.6(b), these calculations were performed assuming a pure proton, helium, oxygen or iron composition, respectively. While the high-energy neutrino flux is suppressed for heavy nuclei, there is an additional contribution of $\bar{\nu}_e$ from decaying neutrons at lower energies. The spectral shape is not highly dependent upon the composition at the source.

The expected neutrino flux, making hypotheses on the sources features and distribution, can be used to set an upper bounds on expected high-energy neutrino fluxes. The WB and MPR models derived an upper bound on the diffuse neutrino flux from extragalactic sources, which is a few times higher than the most probable one. These two limits are usually used as a conservative reference to be compared to neutrino detector sensitivity. The WB model derived an upper bound on neutrino fluxes assuming a generic E^{-2} spectrum for all extra-galactic isotropically distributed sources which are optically thin (e.g. AGN and GRBs). It uses the observed spectrum of cosmic rays with energies above 10^{18} eV as an input and assumes that these are protons of extra-galactic origin. The predicted upper limit is:

$$E_\nu^2 \frac{d\phi}{dE_\nu} < 4.5 \cdot 10^{-8} \text{GeVcm}^{-2}\text{s}^{-1}\text{sr}^{-1}. \quad (1.10)$$

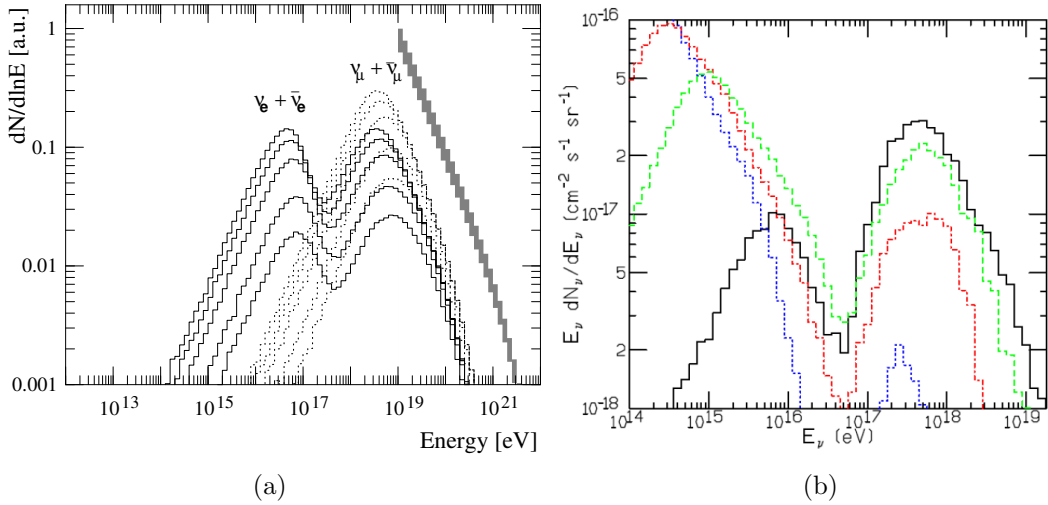


Figure 1.6: (a): Neutrino fluxes produced during the propagation of protons over 10, 20, 50, 100 and 200 Mpc (from bottom up) in a 1 nG magnetic field [23]. The heavy grey histogram shows the assumed proton injection spectrum. (b): The all-flavor neutrino spectrum produced in the interaction of cosmic rays with the Cosmic Microwave Background. The calculations for heavy nuclei (helium (green, dashed), oxygen (red, dot-dashed) and iron (blue, dots)) are compared to the result for protons (black, solid line) [29]. For heavy nuclei, the flux is reduced at higher energies.

The WB model is considered to be not completely model-independent, since the assumption of the optically thin sources with the generic E^{-2} spectrum could imply a Fermi-acceleration mechanism and did not include other neutrino sources.

The MBR model derived an upper bound on neutrino fluxes using the estimated power law coefficient from fitting the cosmic ray flux between $10^{17.6}$ and 10^{20} eV, assuming that all the cosmic rays have an extra-galactic origin and are produced by neutron decay (Eq. 1.8). Both neutron-transparent and neutron-opaque sources are considered. The limit for opaque sources is:

$$E_\nu^2 \frac{d\phi}{dE_\nu} < 2.0 \cdot 10^{-6} \text{GeVcm}^{-2}\text{s}^{-1}\text{sr}^{-1}, \quad (1.11)$$

which is about two orders of magnitude larger than the WB limit. This is because an opaque source is assumed to let very few charged cosmic ray escape, but it is transparent to neutrinos and γ -rays. The MBR limit has been partially excluded by the AMANDA-II observational limit [30]. Fig. 1.7 shows different flux models overlaying the WB bound, for more details see [31].

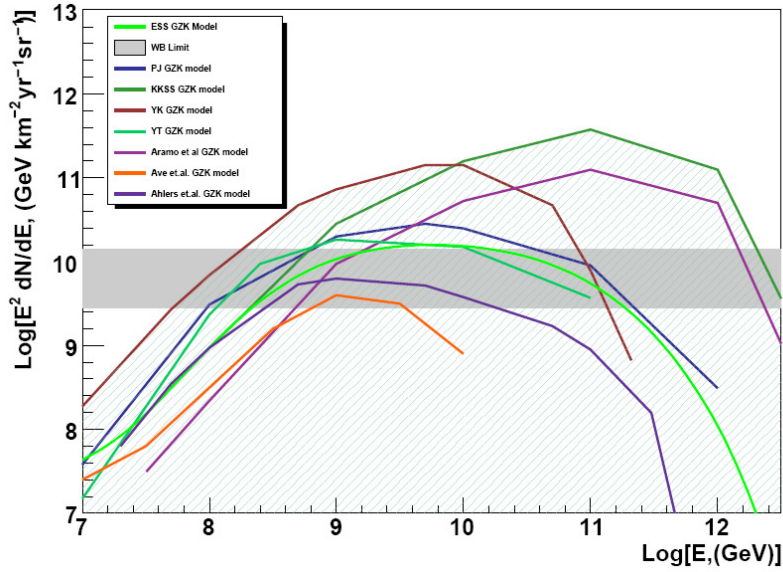


Figure 1.7: Different GZK flux models overlaying the WB bound. From [31].

1.3.4 Possible astrophysical neutrino sources

The UHE cosmic rays are currently considered to originate from an extra-galactic sources, because they are not known inside our galaxy. Both neutrinos and high-energy photons could originate from hadronic cosmic ray accelerators. By assuming that most of the observed γ -rays originate from π^0 -decays, γ -ray sources are considered as good candidates for neutrino sources. Charged cosmic ray and γ -ray observations allow predictions of the expected extra-galactic UHE neutrino flux. There are several expected candidates for extra-galactic sources: the most possible sources are AGN and GRBs. They are thought to rely on the same kind of mechanism, i.e. the accretion of matter onto a black hole powering a relativistic jet, as sketched in Fig. 1.8.

Active Galactic Nuclei (AGN)

AGNs are assumed to be galaxies with supermassive black hole ($\sim 10^8$ solar mass) exists inside the center of most galaxies [32]. It is considered to be the most luminous sources of electromagnetic radiation in the universe. It absorbs matter from nearby stars into a rapidly rotating accretion disk. This matter is accelerated to very high energies and is eventually ejected in far-reaching jets along the rotational axis of the disk. The jets can extend over several Mpc, pointing away from the core in opposite directions. The magnetic fields and shocks thought to be present in jets and accretion disks in AGNs make them a strong candidate for cosmic ray acceleration, where each type of AGN has an associated particle acceleration model.

Accelerated proton, generated in hadronic accelerators, interact with ambient matter or photons in and around sources and neutrinos are produced through pion production.

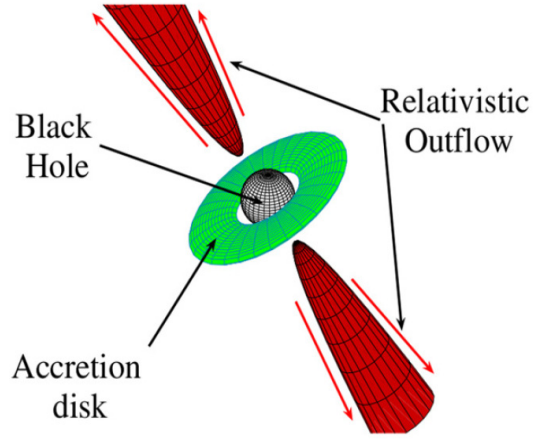


Figure 1.8: Unified scheme of the probable mechanism powering AGNs and GRBs. From [15].

In AGN, there are two possible production regions: the region close to the central engine and the AGN jets [33]. Protons could be accelerated by the Fermi-acceleration mechanism due to the shock wave in the central region, which is created due to the pressure of the accreting matter, or in the AGN jet. The accelerated proton interacts with internal synchrotron photons or with thermal photon backgrounds around the accretion disk and produces neutrinos through pion production.

According to the unified models, AGN have been classified into a number of different subcategories based on the angle between their jet and the observation axis, the size of the accretion disk, and the mass of the black hole. Fig. 1.9 shows different types of AGN depending on the viewing angle of the accretion disc. "Blazars" are radio loud AGN and the jets are pointing in the direction of the observer (Earth). Blazars are expected to be a source of high-energy cosmic ray. The Pierre Auger Observatory observed that the correlation between the positions of AGN and the source direction of cosmic rays above 6×10^{19} eV is not strong [34]. The correlating fraction is about 38% for anisotropic cosmic rays, however it was expected to be about 21% for isotropic cosmic rays.

Cosmic rays are likely to be dominated by heavy nuclei at UHE. Cosmic ray composition relies on shower simulations that use hadronic interaction models to extrapolate particle interaction properties two orders of magnitude in centre-of-mass energy beyond the regime where they have been tested experimentally. A knowledge of CR composition is important for deciding which of several source scenarios is more likely. On the other hand, if the evidence for anisotropy is substantiated by future data, then it should also become possible to discriminate between different astrophysical scenario using different models.

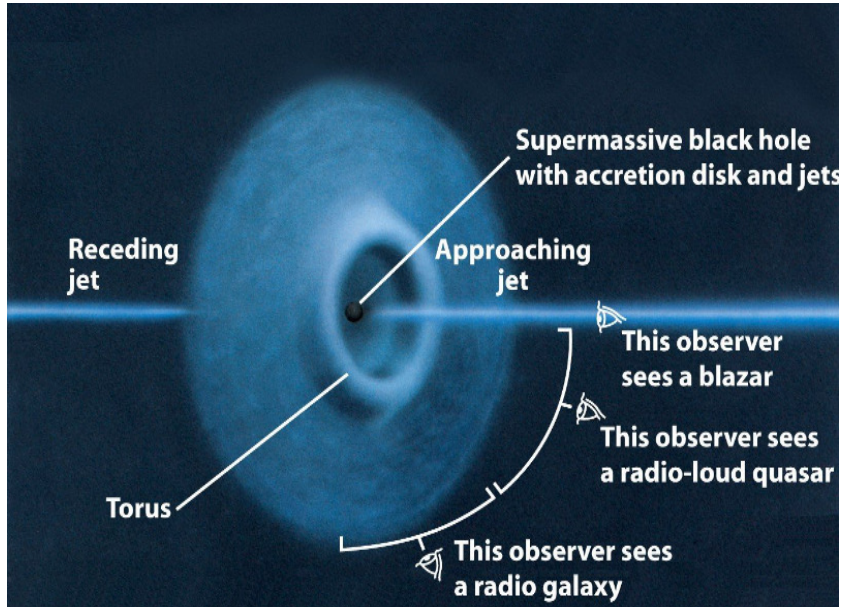


Figure 1.9: Unified model of AGNs. Different types of AGN is shown depending on the viewing angle of the accretion disc. From [35].

Gamma Ray Bursts (GRB)

GRBs are assumed to be the highest luminous objects in our universe and located at large cosmological redshifts. They are isotropically distributed over the sky. They are classified into two categories: long (of duration > 2 s) or short (of duration < 2 s). Long bursts are believed to appear with the core-collapse supernovae of massive stars to form a neutron star or black hole [36]. Short GRBs are thought to result from merging two stars, double neutron stars, or a neutron star and a black hole [37].

There are two models considered to explain the GRB mechanism: the fireball model [38] and the cannonball model [39]. The "fireball" (FB) model has been widely used as a standard GRB model [38]. In the beginning of creation, the optical depth is large enough to prevent the emission of photons from the fireball. After the expansion that is reduced the kinetic energy of the fireball and the optical depth is diminished, synchrotron radiation by accelerated electrons produces part or all of the observed gamma rays. Another model called "cannonball" (CB) [39] has been used which considers mass ejecta in the form of discrete bullets or cannon-balls ejected at relativistic velocities. These two models have been used extensively to analyze GRBs and their afterglows to provide a faithful physical description of the production of high-energy cosmic-ray emission in GRBs. In both models, an accretion disk is created after a stellar collapse around the newly formed compact object (solar-mass black hole). Therefore highly relativistic jets are emitted in opposite directions along the rotation axis, see Fig. 1.10.

The observed afterglow γ -ray emission is explained by synchrotron radiation from accelerated high-energy electrons in internal shocks and/or inverse Compton scattering in

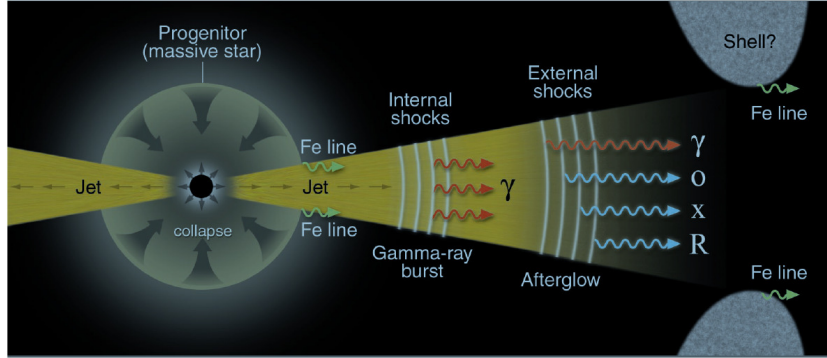


Figure 1.10: The fireball shock model for GRBs. From [40].

the outflows. Because of the strong magnetic fields, GRBs are considered as candidates for the acceleration of cosmic rays to high energy [41]. Neutrinos can also be produced if proton acceleration occurs. The neutrino flux will depend on the ratio of proton to electron acceleration.

Recently, an upper limit on the flux of energetic neutrinos associated with GRBs is estimated by IceCube experiment. The estimated limit is found to be at least a factor of 3.7 below the predictions. This implies either that GRBs are not the only sources of cosmic rays with energies exceeding 10^{18} eV or that the efficiency of neutrino production is much lower than has been predicted [42].

1.3.5 Current neutrino flux limits

Experimentally, the diffuse flux of the UHE neutrinos, which arises from the superposition of all astrophysical neutrinos, might give rise to a detectable signal. As shown in Fig. 1.11, the IceCube collaboration reported an upper limit, using almost half the IceCube detector, with energies above 10^{16} eV [43]. This limit constrains various cosmogenic neutrino flux models. A significant lower limit is expected from the full IceCube detector. No evidence for such neutrinos has been found and upper limits have also been calculated by the Auger [44] and HiRes [45] experiments.

Regarding to the acoustic neutrino detection, the neutrino flux limits were estimated, at extremely high energy (EHE), by different experiments as shown in Fig. 1.12. An upper limit has been set by the SAUND experiment [46], the ACoRNE [47] and the SPATS [48] collaborations. Also as shown in Fig. 1.12, the neutrino upper limits have been presented by various experiments using the radio method, namely RICE [49], ANITA [50], FORTE [51] and GLUE [52].

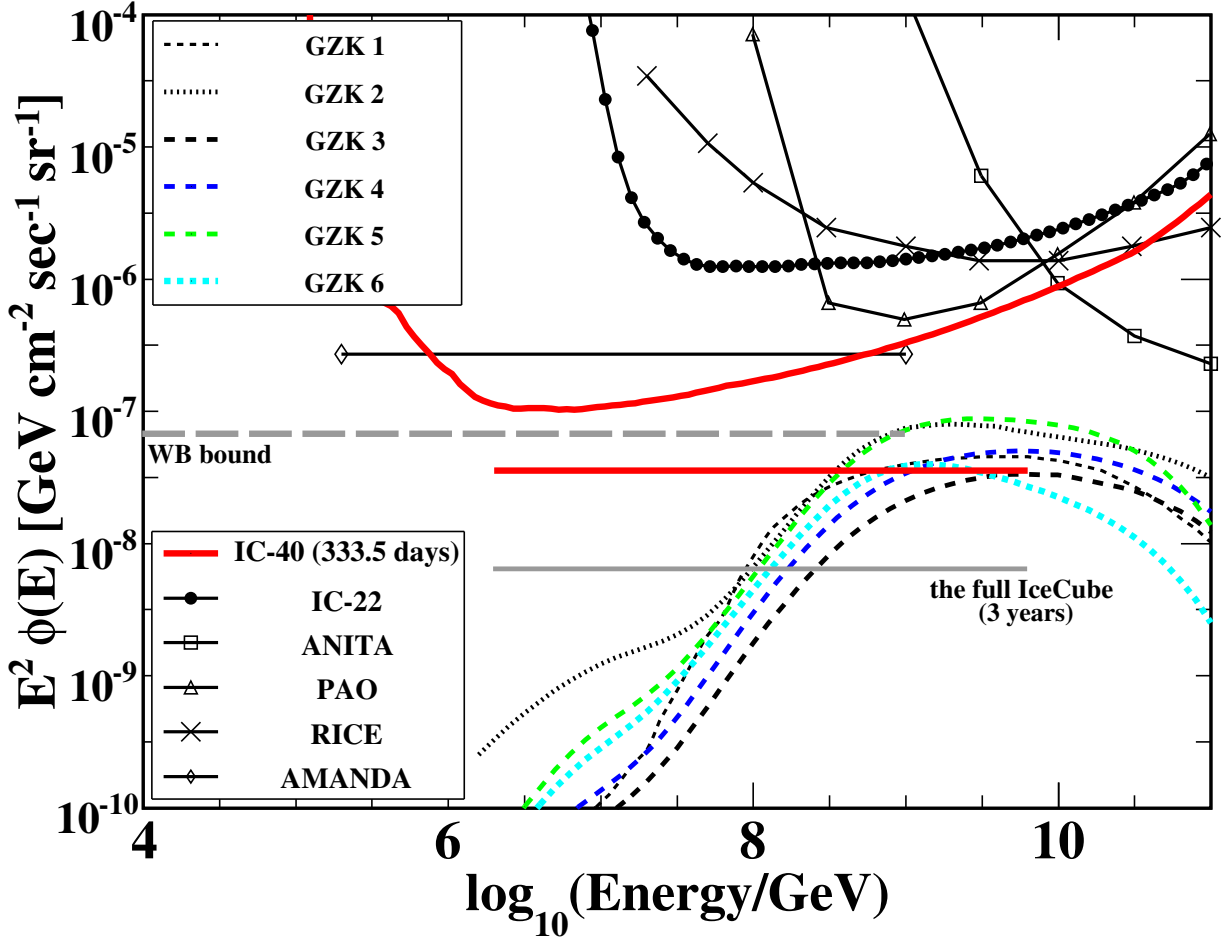


Figure 1.11: The all flavor neutrino flux differential limit and the E^{-2} spectrum integrated limit from the IceCube-40 extremely-high-energy (EHE) analysis (red solid lines) [43]. Various model predictions (assuming primary protons) are shown for comparison, see reference for details. Limits from other experiments are shown for the Pierre Auger Observatory, RICE, ANITA, and Amanda (for references, see [43]). The previous result from IceCube-22, the estimated limit for three years of observation with the full IceCube detector and the Waxman-Bahcall bound with cosmological evolution are shown. From [43].

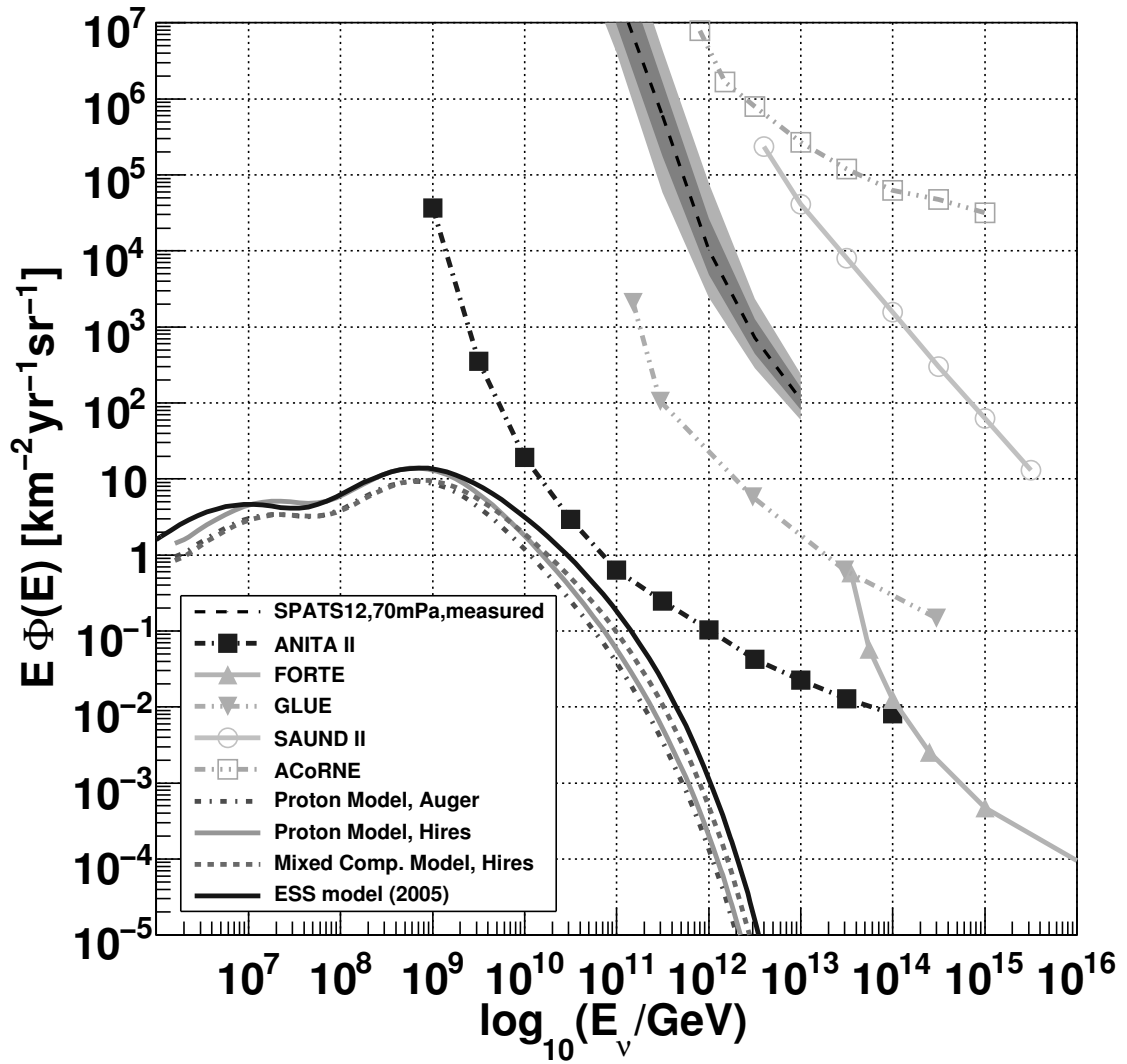


Figure 1.12: Neutrino flux upper limit on the high-energy neutrino flux from various experiments that use either the radio (ANITA II, FORTE, GLUE) or the acoustic (SPATS, SAUND, ACoRNE) detection method. From [48].

Ultra High Energy Neutrino Detection

UHE neutrinos interact with the medium's nucleons and creates both hadronic and electromagnetic cascades. The deposited energy from the neutrino-induced cascades produces detectable optical, radio and acoustic signals. An overview of the neutrino interaction in dense medium and its different detection methods will be presented. Also, a brief overview about the SPATS array, which is deployed in the South Pole ice to investigate the feasibility of acoustic neutrino detection, will be given.

2.1 Deep Inelastic Scattering

In the Standard Model, high-energy neutrinos interact only weakly via deep inelastic scattering (DIS) with a nucleon of a nucleus in the target material. Interactions can be charged current (CC), mediated by the charged W^\pm boson [53]:

$$\nu_l(\bar{\nu}_l) + N \rightarrow l^-(l^+) + X \quad (2.1)$$

or neutral current (NC), mediated by the neutral Z^0 boson:

$$\nu_l(\bar{\nu}_l) + N \rightarrow \nu_l(\bar{\nu}_l) + X \quad (2.2)$$

where N is the nucleon of the target material, $l = e, \mu, \tau$ is the leptonic flavour and X is the hadronic shower. In CC interactions, the neutrino converts into the corresponding lepton and the kinetic energy transferred to the nucleon generates a hadronic shower. In NC interactions the outgoing neutrino can not be detected, so the only visible part of the final state is the hadronic shower. The interaction probability depends on the cross sections of the two processes. Fig. 2.1 shows the contributions of these two components to the total neutrino-nucleon cross section ($\sigma_{\nu N}^{tot} = \sigma_{\nu N}^{CC} + \sigma_{\nu N}^{NC}$). About 80% of the initial neutrino energy stays in the leptonic channel, while the rest goes to the hadronic shower [54]. The emerging charged lepton can give rise to a track and/or an electromagnetic cascade. Neutrino-nucleon interactions dominate over neutrino-electron interactions due to the small electron mass and the composite structure of the nucleon. The exception exists in the resonance reaction (Glashow resonance [54, 55]) of a $\bar{\nu}_e$ with an electron:

$$\bar{\nu}_e + e^- \rightarrow W^- \rightarrow \text{anything} \quad (2.3)$$

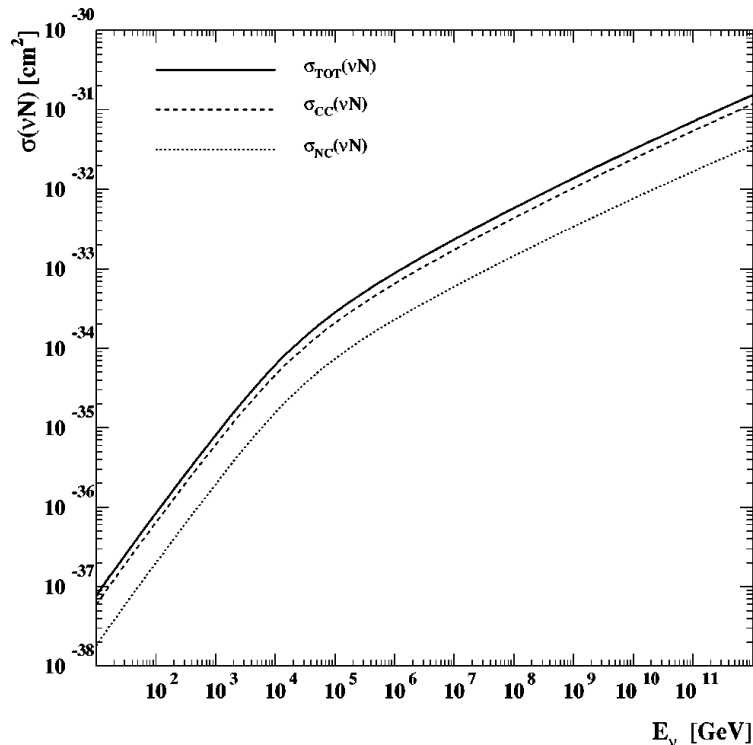


Figure 2.1: The total νN cross-section and its decomposition into contributions from charged current and neutral current plotted as a function of the laboratory neutrino energy. From [56].

which happens at an energy around $E_\nu = 6.3 \text{ PeV}$, where the resonant W^- -boson production enhances the cross section by two orders of magnitude.

In [56] the CC and NC neutrino cross section are calculated as a function of the laboratory neutrino energy. Fig 2.1 shows the νN cross section as a function of energy of the neutrino E_ν . One observes a strong rise, nearly 8 decades, with increasing energy from 10 to 10^{12} GeV. One also notes that the charged current contribution is dominating over the neutral current by factor of 3.

2.2 Cascades

UHE neutrino interacts with medium's nucleons and creates both hadronic and electromagnetic cascades. Hadronic cascade will be produced at the interaction point and carry about 20% of the incident neutrino energy. Leptonic cascade will carry the rest of the total energy and travel further in the medium.

2.2.1 Electromagnetic cascade

When a high-energy electron (e^-) or photon (γ) hits a material target, an electromagnetic cascade is created inside the material. Bremsstrahlung and pair production are the dominant high-energy processes at the beginning of the shower development. Due to Bremsstrahlung, an e^- loses $1/e$ of its energy on average over a distance X_0 , the radiation length. The secondary γ can then produce an e^+e^- pair. The number of particles thus grows exponentially. e^- and e^+ lose energy due to ionization as they travel inside the material. After reaching a critical energy (E_c), when the energy loss due to Bremsstrahlung becomes equal to the energy loss due to ionization, e^- and e^+ lose their energy mostly due to ionization and the cascade eventually stops. A rough estimate of the critical energy is $E_c \sim 605/Z$ [MeV] where Z is the atomic number of the medium [57]. The longitudinal development is governed by the high-energy part of the cascade, and scales as the radiation length X_0 (39.05 cm in ice) in the material. The transverse development of electromagnetic showers in different materials scales fairly accurately with the Moliere radius R_M , which is for example about 13 cm in ice.

2.2.2 Hadronic cascade

An hadronic cascade is produced in both CC and NC DIS neutrino interactions. Generally it can be treated similar to electro-magnetic cascades. However, hadronic cascades are less affected by the LPM effect [58]. The average energy transferred to the hadronic cascade is about 20% of the initial neutrino's energy. There are, however, large fluctuations in this interaction so in some cases the majority of the energy of the incoming neutrino can be transferred into the hadronic cascade. The particles in the hadronic shower, mostly high-energy pions, will maintain the direction of the primary neutrino because their average transverse momentum is expected to be in the few hundred MeV range. The cumulative angular deviations are very small even after several generations of hadronic particles. The hadronic shower will consist of a hard penetrating central core which feeds electromagnetic subshowers fundamentally through π^0 decay into two photons. Because the medium is dense, charged pions are expected to interact before decaying. Assuming energy equipartition between all flavor pions, a fraction of $1/3$ would go into electromagnetic subshowers every time there is an interaction.

2.2.3 LPM effect

The Landau-Pomeranchuk-Migdal (LPM) effect [59, 60] is a reduction of the bremsstrahlung and pair production cross sections at high energies or high matter densities. It increases the electron and photon interaction lengths above some threshold energy E_{LPM} (about 2 PeV for ice [61]). The LPM effect becomes important for the cascade development at the highest energies, $E_\nu > 10^{18}$ eV where the pair production and Bremsstrahlung cross-sections are significantly decreasing with increasing energy of the incident particle or photon. The electromagnetic showers are elongated dramatically by LPM effect, while

hadronic showers show much smaller elongation because most of the electrons and photons in the hadronic shower come from the decays of π^0 produced in the hadronic interactions. Pions undergo more interaction than decay, which happens in ice above 40 PeV. Therefore, a small fraction of the hadronic shower is subject to LPM elongation [61]. The deposited energy density from hadronic showers is larger than the energy from electromagnetic showers (which takes on average 80% of the incident neutrino energy).

2.3 Neutrino detection methods

The interactions of high-energy neutrinos in a dense medium (water, ice or salt) produce optical, radio and acoustic signals. Each of these signals therefore provides a possible method of detecting the neutrinos. This section gives an overview of the current optical, radio and acoustic high-energy neutrino detection methods.

- **Optical method:**

The idea of the optical neutrino telescope based on the detection of the secondary particles produced in neutrino interactions was first formulated in the 1960s by Markov [62]. He proposed to install detectors deep in a lake or in the sea and to determine the direction of the charged particles with the help of Cherenkov radiation.

The optical detection method is based on measuring the *Cherenkov radiation* that is emitted by the charged secondary particles (muons) produced from νN interaction when they travel with a velocity greater than the speed of light. The charge of muons causes the surrounding medium to become polarised. Subsequent depolarisation of the medium results in the emission of Cherenkov photons along the relativistic charged particle track. Constructive interference between photons can occur if the muon's speed is greater than the light speed in the detection medium to produce the Cherenkov radiation (if $(\beta = v/c) > 1/n$, where v is the muon's speed and n is the refractive index of the medium). The radiation is emitted at a characteristic angle with respect to the track. This angle is called the Cherenkov angle, θ_c and is given by

$$\cos \theta_c = \frac{1}{\beta n} \tag{2.4}$$

where β is the velocity of the particle expressed as a fraction of the speed of light in vacuum, c , and n is the index of refraction of the medium.

There are mainly two types of events which can be detected by Cherenkov light: cascades and tracks. An illustration of both types of events is shown in Fig. 2.2. For cascades nearly the whole energy is deposited in a small interaction region. In this case, the Cherenkov light propagates spherically with only a small extra amount of light in the forward direction of the neutrino. Charged particles produce Cherenkov light along their track during their propagation through matter. The optical detector

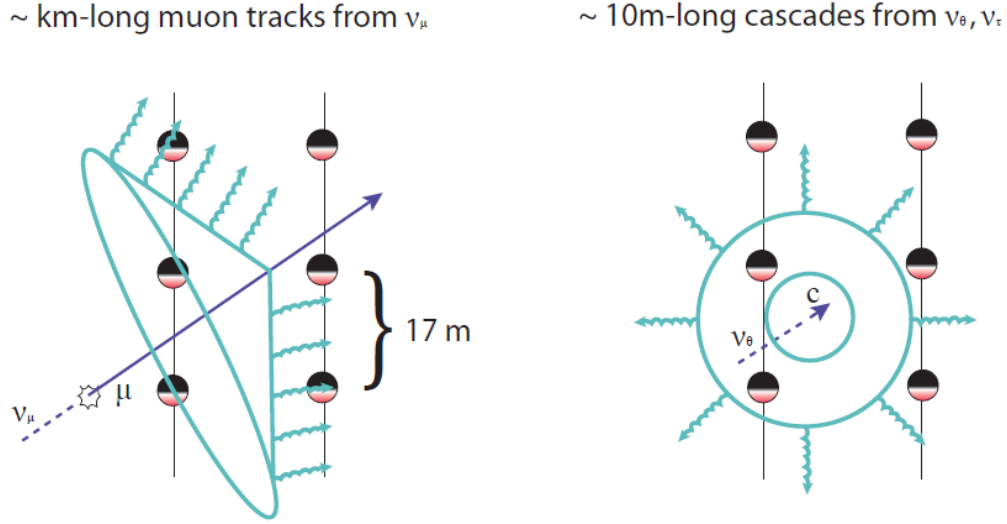


Figure 2.2: Cherenkov light patterns produced by muons (left) and by showers initiated by electron and tau neutrinos (right) and by neutral-current interactions [63].

operates by detecting the intensity and arrival time of this Cherenkov light, produced from the νN interaction, on a three-dimensional array of photo multiplier tubes (PMTs). From these measurements, the properties of the neutrino are inferred.

- **Radio method:**

Neutrinos can be detected through the radio signal generated via the Cherenkov radiation of charged particles produced by the neutrinos interacting in some material on Earth or in its vicinity. The dominant mechanism responsible for this radio emission depends on the nature of the propagation medium, but in all cases the relevant parameter is the size of the shower, which sets the scale of frequencies where the radio signal is emitted coherently. The radio pulses could be produced through the interaction in the Earth's atmosphere or in dense medium [15]. A short overview of the field can be found in [64].

- Radio emission from air showers: The radio pulses are produced by the synchrotron emission of electrons and positrons of the shower when a primary interacting in the Earth's atmosphere. The coherent radio signal propagates into the forward direction of the shower and peaks at about 1 MHz. It is detected using an arrays of antennas deployed at ground level, often in the same location as other extensive air-shower detectors. The detection of radio pulses from air showers is well suited for the detection of charged cosmic rays, which readily interact in the atmosphere. However UHE neutrinos could be detected by looking for nearly horizontal air showers.
- Radio emission in dense media (the Askarian effect): When neutrinos of very

high energy interact in matter, the development of the subsequent shower progresses with electrons being Compton scattered into the shower, while positrons annihilate. This leads to a net 20% – 30% negative charge excess [65], an observation first described by Askarian in 1962 [66]. Askarian also predicted that at the same frequencies where the radio Cherenkov signal is coherent, long attenuation lengths can be found in media that occur naturally in large volumes such as ice, salt and sand.

- **Acoustic method:**

High-energy neutrino interacts in dense medium and produce an acoustic signal based on the thermo-acoustic mechanism. This mechanism was first discussed by Askarian in 1957 [67]. The acoustic signals will be created from the thermal expansion that created by the deposited energy from the neutrino interaction. The acoustic pressure pulse depends on the spatial and temporal development of the deposited energy density and the physical properties of the detection medium. More details about the thermo-acoustic effect are given in § 3.1.

2.3.1 Optical neutrino detectors

- **Water**

In water, the pioneering project for the construction of an underwater neutrino telescope was due to the DUMAND collaboration [68, 69], which attempted to deploy a detector off the coast of Hawaii in the 1980s. Work began in about 1976 but the project was cancelled in 1995 due to technical difficulties. Although it was never completed, DUMAND was in a sense a precursor of the upcoming neutrino telescopes. In parallel, the BAIKAL collaboration [70] started to realize a workable detector system under the surface of the Baikal lake [70]. The pioneering DUMAND experience is being continued in the Mediterranean Sea by the ANTARES [71], NEMO [72, 73] and NESTOR [74] collaborations, which have demonstrated the detection technique [62].

- **Ice**

In deep ice, a major step towards the construction of a large neutrino detector was taken by the AMANDA collaboration [75]. AMANDA deployed and operated optical sensors in the ice layer of the Antarctic starting from 1993. After the completion of the detector in 2000, the AMANDA collaboration proceeded with the construction of a much larger apparatus called IceCube [76] which started in 2006. IceCube completed construction in December 2010.

The IceCube [76] project transforms 1 km³ of deep and ultratransparent Antarctic ice into a neutrino telescope (see Fig. 2.3). The IceCube neutrino telescope is located in Antarctica, at the site of the South Pole Amundson-Scott station. The IceCube neutrino observatory consists of 80 strings in a hexagonal structure spaced by 125 m, each with 60 Digital Optical Modules (DOMs) installed between a depth

2.3. Neutrino detection methods

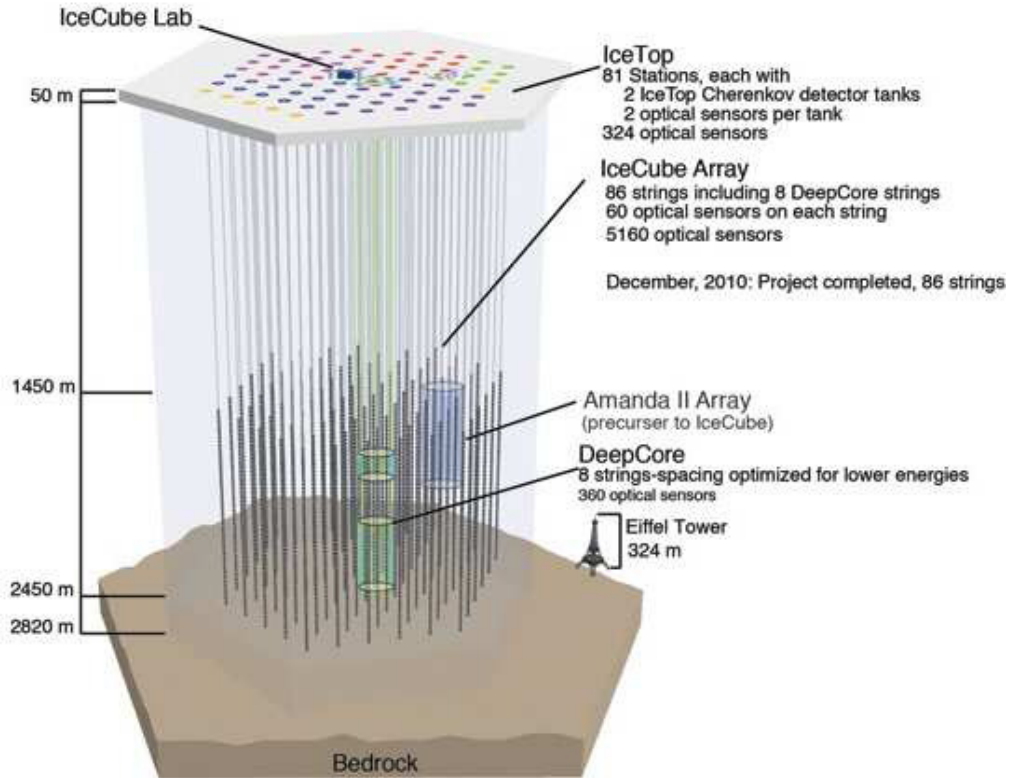


Figure 2.3: The IceCube detector: the IceTop cosmic-ray EAS detector is situated on top of the ice. 80 IceCube strings will each have 60 Digital Optical Modules (DOM) instrumenting in total 1 km^3 of ice. A DeepCore of 6 additional strings (also carrying 60 DOMs) forms the low-energy extension in the heart of the detector.

of 1450 m and 2450 m resulting in a total of 4800 DOMs. String spacing is chosen corresponding to the attenuation length of light $\mathcal{O}(120 \text{ m})$ in the South Pole ice and is optimized for energies between TeV and PeV. In addition, a DeepCore of 6 additional strings are deployed. The DOMs of those strings are deployed in two depths between 1750 m and 1860 m and 2107 m and 2450 m, with a DOM spacing of 7 m and a distance of 72 m between the strings. The in-ice array is complemented by a surface array, IceTop, which is an Extensive Air Shower (EAS) detector that consist of 160 ice-tanks, in pairs, near the top of each IceCube string.

The DOMs detect the Cherenkov light emitted by secondary particles produced when neutrinos interact with nuclei in the ice. Each DOM is a complete data acquisition system including a PMT, digitization electronics, control and trigger systems, and light-emitting diodes for calibration. The light patterns reveal the

type (flavor) of neutrino interaction and the energy and direction of the neutrino, making neutrino astronomy possible. The scientific missions of IceCube include such varied tasks as the search for sources of cosmic rays, the observation of galactic supernova explosions, the search for dark matter, and the study of the neutrinos themselves.

2.3.2 Radio neutrino detectors

In the following the experiments working in the field will briefly be introduced according to their detection medium.

- **Ice**

Antarctic ice is used as a detection medium for most current and proposed radio Cherenkov experiments. This is due to its large ice volume, the long attenuation lengths observed at the frequencies of interest, and the existing infrastructure and science programs on the continent. Finally, one advantage of building a radio array at the South Pole is the possibility of observing events in coincidence with IceCube. In the following, the recent radio activities in the Antarctic ice will briefly be introduced.

- **ANITA (ANtarctic Impulse Transient Antenna)**

ANITA is an Antarctic balloon-borne experiment based on the Askarian effect to detect the Cherenkov radiation from neutrino-induced electromagnetic showers in the Antarctic ice. Fig. 2.4(a) shows the ANITA detection concept for UHE neutrinos. The primary goal of ANITA is to search for astrophysical neutrinos with energies $E > 3 \times 10^{18}$ eV. ANITA consists of an array of 32 broadband (200-1200 MHz) dual-polarization quad-ridged horn antennas that view the Antarctic ice sheet from its in-flight altitude of 37 km, where it is in view of 1.5×10^6 km² of the ice surface. ANITA completed two flights; the first one was (ANITA-I [77]) launched in December 2006 and second one (ANITA-II [50], see Fig. 2.4(b)) launched in the 2008–2009 Antarctic season. The derived limits on the UHE neutrino flux obtained from both flights in the energy range predicted by GZK neutrino models are shown in Fig. 2.5. To enhance the sensitivity to UHE neutrinos, a third ANITA flight (ANITA-III), which has a number of improvements relative to the ANITA-II payload, is planned for the austral summer of 2012/2013 [78].

- **FORTE (Fast On-orbit Recording of Transient Events)**

FORTE was a satellite antenna launched in 1997 that was able to monitor the ice over Greenland until 1999 [51]. It recorded bursts of electromagnetic waves, originating from coherent Cherenkov emission induced by cascades in the Greenland ice sheet, in the radio frequency (RF) range of 30 MHz to 300 MHz with a dual polarisation antenna. The derived FORTE limit on the UHE neutrino flux is shown in Fig. 1.12.

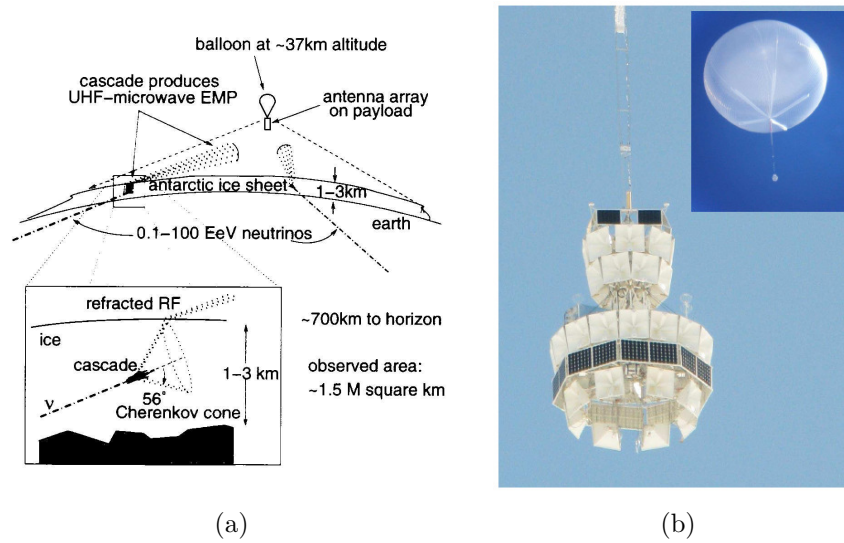


Figure 2.4: (a): Schematic of the ANITA concept for UHE neutrino detection [78]. (b): The ANITA-II payload on ascent with the lower eight horn antennas deployed. The inset shows the balloon and payload viewed telescopically at float altitude of 35 km.

– **RICE (Radio Ice Cherenkov Experiment)**

RICE is an array of 16 broadband antennas (200 MHz-1000 MHz) deployed together with AMANDA in the Antarctic ice cap that has been taking data since 1999. The antennas are contained within a cube of ice 200 m on a side with its center approximately 150 m below the surface [49]. RICE is primarily searching for radio Cherenkov signals from electromagnetic and hadronic cascades induced by UHE neutrinos colliding with nuclei in the ice. No neutrino candidates were found from the full RICE data set. The derived RICE limit on the UHE neutrino flux is shown in Fig. 2.5. Also, an updated limits on the diffuse UHE neutrino flux, based on twelve years of data taken between 1999 and 2010 is derived [81]. No convincing neutrino candidates were found from the full RICE data set.

– **ARIANNA (Antarctic Ross Ice-shelf ANTenna Neutrino Array)**

ARIANNA is a proposed detector for ultra high-energy astrophysical neutrinos. It will detect coherent radio Cherenkov emissions from particle showers produced by neutrinos with energies above about 10^{17} eV. ARIANNA will be built on the Ross Ice Shelf just off the coast of Antarctica, where it will eventually cover about 900 km^2 in surface area. There, the ice-water interface below the shelf reflects radio waves, giving ARIANNA sensitivity to downward going neutrinos and improving its sensitivity to horizontally incident neutrinos. ARIANNA detector stations will each contain 4-8 antennas which search for short pulses of 50 MHz to 1 GHz radio emission from neutrino interactions [82].

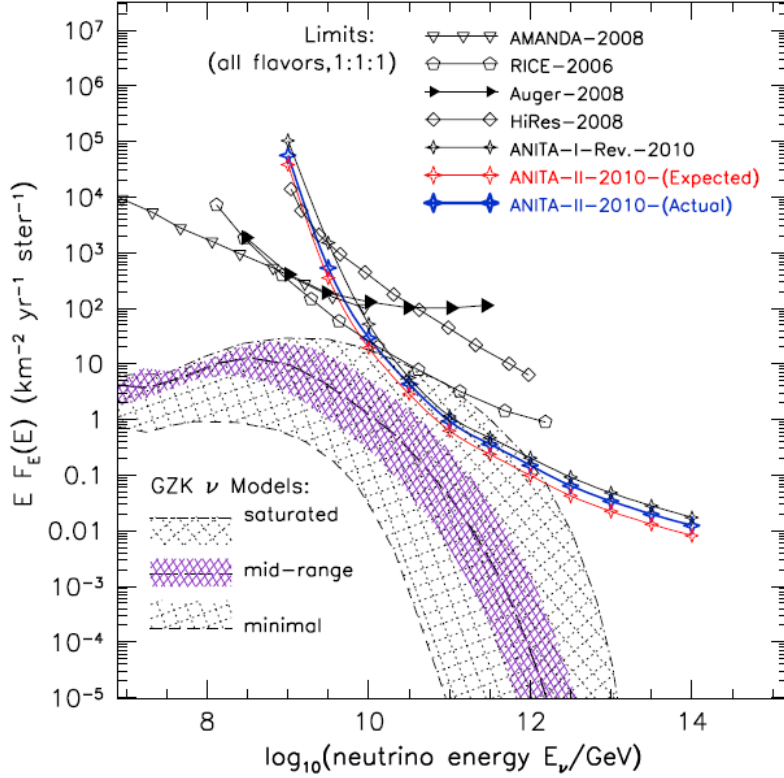


Figure 2.5: ANITA-II neutrino flux limit for 28.5 days of live. Other limits are shown: AMANDA [75], RICE [79], ANITA-I [77], Auger [80], HiRes [45], FORTE [51]. The GZK neutrino flux is determined by a variety of different cosmic ray composition models, see [50] for details.

– **Future radio neutrino detectors at South Pole**

Many neutrino arrays at the South Pole, are under investigation using the IceCube technology and based on the concept of the RICE experiment. The hybrid neutrino detection using IceCube and radio antenna coincidences is possible. These arrays would serve as future large area radio arrays centered around IceCube.

1. **AURA (Askaryan Under ice Radio Array)** is an ongoing project which aims to study the possibility of in-ice radio detection of high energy neutrinos [83]. An AURA antenna cluster consists of 4 broad band antennas centered at 400 MHz to be deployed at a shallow depth at the South Pole.
2. **The NARC (Neutrino Array Radio Calibration)** experiment will serve as a testbed for future development of an eventual large-scale neutrino radio-detection array. NARC is under construction as a part of the IceCube DAQ activities, and used for calibration studies as well as for the

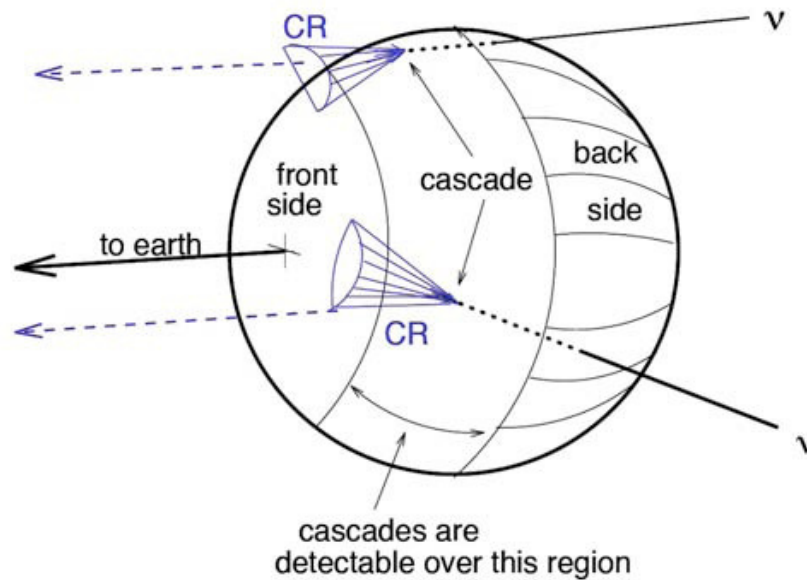


Figure 2.6: Configuration of incoming neutrinos striking the moon, generating high energy cosmic ray particles, which decay to produce photons with peak emission at radio wavelengths. Peak radio emission is expected on the edge of the moon [85].

characterization of the ice properties and of the ambient radio noise [15].

3. **IceRay** is an ongoing experiment which aims to build a very large array to detect GZK neutrinos [84]. Its initial phase consists of large two-dimensional arrays of antenna stations in shallow and deep ice. Efforts are going on to lower the detector energy threshold below 10^{17} eV. This would both increase the total event rate and provide enhanced opportunities for hybrid events with the IceCube detector.

- **Lunar**

As already proposed by Askarian, radio waves from particle showers generated in the lunar regolith by cosmic-rays could be detected. The Moon provides a large and radio-quiet target. Neutrinos, high-energy particles, and photons from the cosmos collide with the Moon rock in the regolith and a coherent sub-ns radio pulse is emitted which can escape through the surface and be detected on Earth as shown in Fig. 2.6. The lunar radio Cherenkov activities will briefly be introduced.

- **GLUE (Goldstone Lunar Ultra-High Energy neutrino experiment)**
GLUE is an experiment that uses two radio telescopes of 34 m and 70 m to look for radio emission from neutrino interactions in the Lunar regolith [86].
- **LOFAR (LOW-Frequency ARray)**
LOFAR is a radio interferometric array which consists of many low-cost antennas. These antennas are organised in aperture array stations. The aim of

LOFAR is to survey the Universe at frequencies from ~ 15 MHz-240 MHz (corresponding to wavelengths of 20 m to 1.2 m) [87]. The stations (currently, 36 stations are being constructed in the Netherlands) are distributed over an area about one hundred kilometres in diameter (located in the North-East of the Netherlands). Several international stations will be built in Germany, Sweden, the UK and France. The array of antennas will be distributed over 100 km within the Netherlands and reaches out to 1500 km throughout Europe. It will provide sufficient resolution to allow radio sources to be identified with visible objects, even at low frequencies.

- **Salt**

- **SalSA (Saltdome Shower Array)**

SalSA is a neutrino radio detector using rock-salt as a detection medium. It has long been proposed that a neutrino detector could be deployed in one of the large salt formations that exist in many locations around the world [88, 89, 90]. Salt as target can be advantageous as it has a higher density compared to ice (2.2 g/cm^3 versus 0.92 g/cm^3), which gives ~ 2.5 times the interaction probability in salt compared to ice. Although the peak power of the emitted radio Cherenkov signal is lower than in ice, the width of the Cherenkov cone is broader [91]. Salt domes are also more accessible than Antarctica. In addition, soil or water above salt domes provide good RF insulation. Disadvantages are probably the high drilling costs for installing radio sensors in salt, when a dense array is needed.

2.3.3 Acoustic neutrino detectors

Neutrinos can be detected when they interact with a dense medium using the acoustic signal that can be produced [66]. There are a number of experiments investigating the feasibility of acoustic particle detection. These experiments are integrated into optical neutrino telescopes as R&D efforts or established as stand-alone experiments. In the following the experiments working in the field will briefly be introduced according to their detection medium.

- **Water**

- **ACORNE (Acoustic Cosmic Ray Neutrino Experiment)**

ACORNE is a military array of hydrophones near the Scottish coast. It has access to the military Rona hydrophone array in North West Scotland. The array consisted of eight hydrophones located at a depth of about 100 m and about 1.5 km distant to each other. Data are taken continuously since December 2005 [92]. The derived limit on the UHE neutrino flux is shown in Fig. 1.12.

– **AMADEUS (Antares Modules for Acoustic DEtection Under the Sea)**

AMADEUS is an integrated R&D project with the ANTARES [71] neutrino telescope and is located in the Mediterranean Sea near Marseilles. It consists of six local clusters of six acoustic sensors, each placed at water depths between 2000 m and 2300 m. The spacing between the clusters varies from 15 m to 330 m, the distances between the hydrophones within a cluster is about one meter. AMADEUS allows for extensive studies of both transient signals and ambient noise in the deep sea, as well as signal correlations on several length scales and localisation of acoustic point sources. Thus the system is excellently suited to assess the background conditions for the measurement of the bipolar pulses expected to originate from neutrino interactions [93]. First results displayed an 80% correlation coefficient between wind speed and the mean detected noise rate, leading to the conclusion that deep-sea noise is dominated by agitation at the surface. The mean power spectral density was measured as 21.8 mPa over an 8-week data-taking period.

– **Lake Baikal**

Along with the Baikal neutrino telescope NT200+, the Lake Baikal collaboration has installed an autonomous acoustic setup in April 2006. It was designed to investigate the possibility of acoustic particle detection. The setup consists of four hydrophones arranged in a tetrahedral geometry, located in Lake Baikal at a depth of about 150 m and is capable of detecting and classifying acoustic signals with different shapes, as well as signals from neutrino induced showers [94]. The measurements showed that the integral noise power in the frequency band 20-40 kHz can reach levels as low as about 1 mPa. The main source of the noise including bipolar pulses is the near-surface zone of the lake. From the sound wave arrival directions analysis, no any bipolar pulses were found by any sources located at large depth in the lake.

– **O ν DE (Ocean Noise Detection Experiment)**

O ν DE was successfully operated at the NEMO Test Site at a depth of 2000 m, 25 km offshore from Catania (Sicily) from January 2005 to November 2006. Comprising four hydrophones arranged in a tetrahedral configuration it took 5 minutes of data every hour enabling detailed noise and transient signal studies [95]. Average noise levels of 5.4 ± 2.2 (sys.) ± 0.3 (stat.) mPa were observed.

– **SAUND (Study of Acoustic Ultra-high-energy Neutrino Detection)**

SAUND is a hydrophone array which uses part of the US military AUTECH hydrophone array in the Bahamas off the eastern coast of Andros Island. The array consists of seven wide-band hydrophones deployed in water to a depth of about 1500 m. Between 2003 and 2004, 195 days of data were recorded leading to the calculation of an upper limit for the neutrino flux. SAUND was the first group to publish a limit on the neutrino flux using acoustic techniques [96]. The SAUND II project represents an upgrade to 49 hydrophones and has been

data taking since summer 2006. The derived limit [46] on the UHE neutrino flux is shown in Fig. 1.12.

- **Ice**

- **SPATS (South Pole Acoustic Test Setup)**

SPATS is the only acoustic detection activity carried out in ice. It consists of four strings deployed in a trapezoid array in the first 500 m of IceCube holes. Each string has 7 acoustic stages, each stage consists of a transmitter module, a receiver module and a temperature sensor alternatively and for the deepest stage a pressure sensor is mounted. SPATS was built to evaluate the acoustic characteristics of the ice in the 10 kHz to 100 kHz frequency range. SPATS has been operating successfully since January 2007 and has been able to measure or constrain South Pole ice parameters, e.g. the attenuation length, the speed of sound, the background noise level and the transient rate. The limit on the UHE neutrino flux at energies $E_\nu > 10^{11}$ GeV was derived from acoustic data taken over eight months, see Fig. 1.12. More detail about SPATS will be presented in the next section.

2.4 SPATS and the retrievable transmitter

SPATS is a 4 string array built to investigate the feasibility of acoustic neutrino detection at the South Pole. Fig. 2.7 shows the SPATS array layout with its in-ice and on-ice components. SPATS was deployed in the 2006/2007 and 2007/2008 polar seasons [97]. A retrievable transmitter, called *pinger*, was developed and used during three seasons to study the attenuation length. More technical details about SPATS can be found in [97].

2.4.1 Geometry

The current geometrical configuration (see Fig. 2.8) is the result of a compromise between the geometry necessary to achieve the physics goals and the actual IceCube geometry. SPATS has a good horizontal coverage, where the uncertainty on the horizontal position of each string is fixed and known to be ± 0.5 m, so that the relative error decreases with increasing string-to-string distance (so called baseline). Long baselines allow for a more precise measurement of the arrival times of the signal.

As shown in Fig. 2.7, each of the four strings has seven acoustic stages at specified depths. Table 2.1 gives the the corresponding levels for each string and baselines for SPATS. The vertical distance between the acoustic transducers was chosen to increase with depth following the measured temperature and density profiles of the ice [98, 99].

2.4. SPATS and the retrievable transmitter

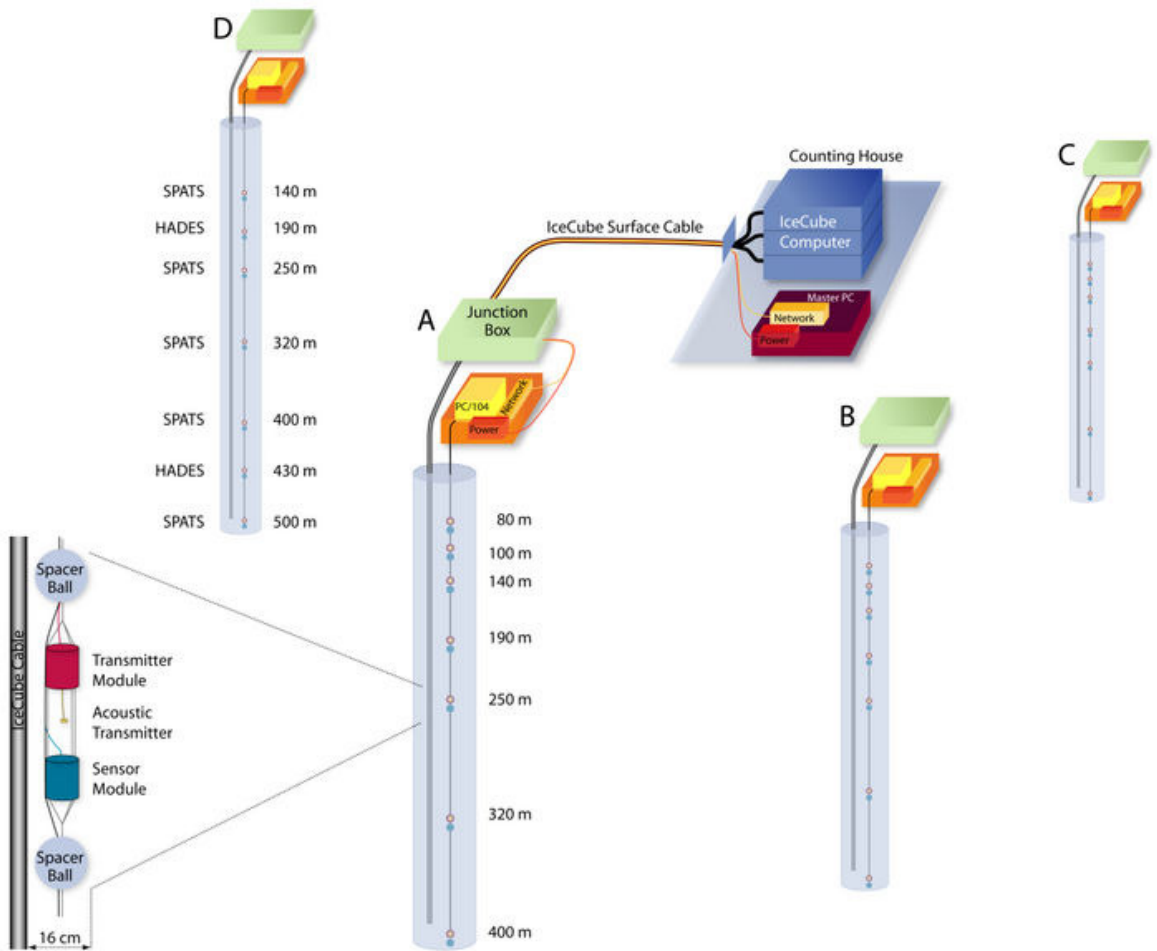


Figure 2.7: Schematic of the SPATS array, with the four strings consisting of seven acoustic stages.

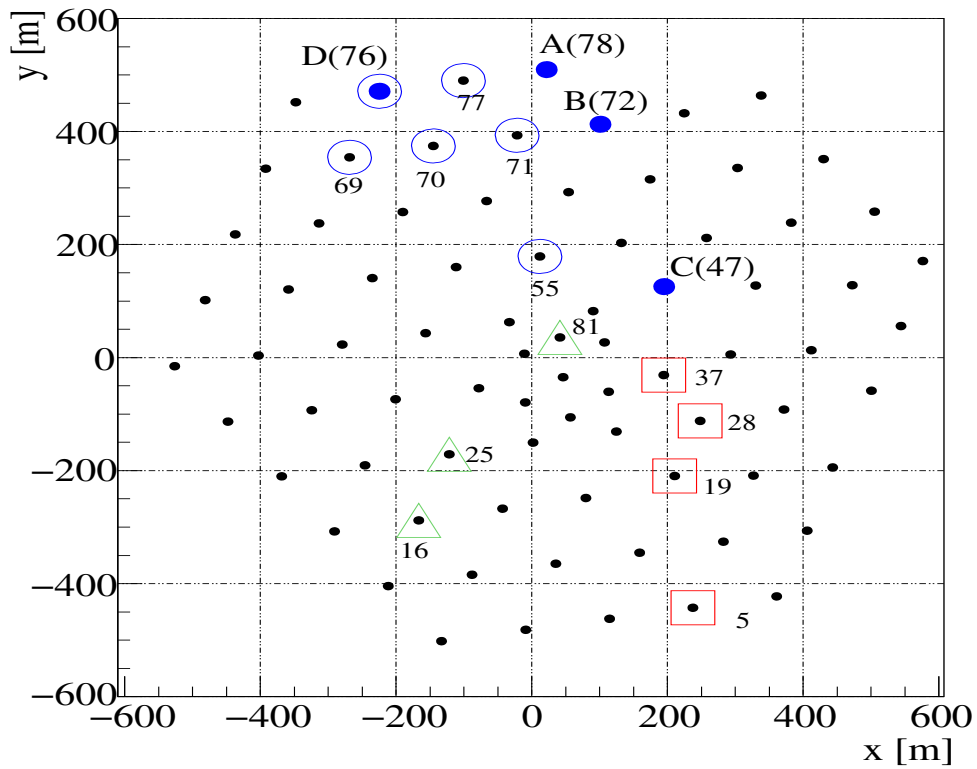


Figure 2.8: SPATS strings (blue circles) overlaid on the IceCube geometry as of February 2009 (black dots). The String ID (A,B,C or D) is given followed by its corresponding IceCube hole number. The blue open circles, red open squares and green open triangles show the positions of the 2007/2008, 2008/2009 and 2009/2010 pinger holes (the *pinger* is a retrievable acoustic transmitter) with the corresponding IceCube hole number respectively. From [97].

String	Deployed (2007)	Baseline (m)	Breakouts (m)
A	14 th January	(A-B) 125	80,100,140,190,250,320,400
B	11 th January	(B-C) 302	80,100,140,190,250,320,400
C	22 nd December	(C-A) 421	80,100,140,190,250,320,400
D	24 th December	(D-C) 543	140,190,250,320,400,430,500

Table 2.1: Deployment details for SPATS.

2.4.2 Hardware

Each string has an *acoustic junction box* (AJB), a read-out box buried under roughly 3 m of snow, that is a robust aluminium box located on the top of each string. Each AJB has an industrial PC, called string-PC, used for digitization, time stamping, and storage of the data. Each string-PC is connected by a symmetric DSL connection to the SPATS master-PC that is housed in the IceCube laboratory. The master-PC collects the data from all four string-PCs, distributes a GPS timing signal to them, and prepares the data for transfer to the northern hemisphere via satellite or tape storage.

Each acoustic stage consists of a separate transmitter and sensor module. All the electronic circuits are located in steel¹ pressure housings. An entire stage is about 1.5 m long and maximum 16 cm wide with a total weight of 10 kg. The transmitter module is mounted about 45 cm above the sensor module (see Figure 2.9). The stages are assumed to be positioned at predefined nominal depths within an error of ± 2 m. Each acoustic stage is connected to the Acoustic Junction Box (AJB) that is located at the surface.

The SPATS transmitters use the same lead zirconium titanate (PZT) material, namely PIC151, manufactured by PI-ceramics². This is a soft piezo-ceramic material with a high piezoelectric charge constant ($d_{33} = 500$ pC/N), high permittivity and high coupling factor. It is traditionally used for low-power ultrasonic transducers and low-frequency sound transducers.

A SPATS sensor module has three piezo-ceramic elements, each placed 120° apart to ensure good angular coverage. A so-called SPATS sensor channel consists of a cylindrical (10 mm diameter and 5 mm height) piezo-ceramic element (same PZT-type as for the transmitter) that is pressed against the steel housing. The piezo-ceramic element is directly soldered to a 3-stage amplifier. Three different types of sensors, first and second generation SPATS sensors and the HADES (Hydrophone for Acoustic Detection at South Pole) sensor [101, 102] were deployed.

We refer to each sensor channel by the string identifier letter (A, B, C, or D), a capital S for sensor, the number of the stage (1-7, counting from top to bottom) and the number of the channel (0-2). For example, AS6(0) indicates channel 0 of the sensor module number 6 of string A.

¹Stainless steel grade 304/1.4301

²<http://www.piceramic.com>



Figure 2.9: View of an acoustic SPATS stage. The transmitter module is mounted about 45 cm above the sensor module. The two spacer balls are used to assure a minimum distance of the stage to the IceCube main cable and the wall of the hole. From [100]

2.4.3 Retrievable transmitter (Pinger)

To measure the attenuation length the signal emitted by a transmitter was recorded by different sensors from different distances. With the SPATS array, all transmitters and sensors are frozen in the ice, therefore their location cannot be changed. In addition, systematic uncertainties are high since each sensor/transmitter has a different sensitivity/transmittivity, depending on both the azimuthal angle and the polar angle. Each module can rotate during the freeze-in of the hole, so nothing is known about the orientation of the sensors/transmitters after deployment.

A retrievable acoustic transmitter called the *pinger* (for more detail see [103, 97]) was used to minimize the systematic uncertainties. The pinger was used in multiple water-filled holes, prior to IceCube deployment. The pinger holes were aligned to SPATS array providing an independent polar and azimuthal sensor sensitivity for possible transmitter/sensor combinations. The pinger is an autonomous transportable device consisting of a high-voltage pulser and emitter, to be lowered in water, and an on-ice box providing the power and the trigger signal, called the Acoustic Pinger Box (APB). The two parts are connected through the cable which is spooled on a winch used to lower and raise the stage.

- **The Acoustic Pinger Box (APB)**, contains a 4×6 V sealed lead acid rechargeable battery pack, specified to work at low temperatures down to -65° , to drive the high voltage pulser board. It was connected to a GPS receiver and the GPS clock is used to generate a Pulse Per Second (PPS) trigger pulse.
- **The high voltage pulser board**, based on a modified transmitter board, is located in a steel housing (diameter: 10 cm; height: 15 cm). This board generates the high voltage pulse which excites the piezo element of the pinger ball. The board hardware was modified during the different deployment seasons.
- **The transmitting piezo element**: as a transmitting element the ITC-1001³ was chosen. It consists of two hemispheres in high precision Channelite-5400 lead zirconate titanate ceramic which form the transmitter ball and emits a spherical beam. The specified maximum working depth is 1250 m.

The retrievable transmitter was deployed in 13 water-filled IceCube holes during three successive seasons. The corresponding holes for each season are shown in Fig. 2.8. The pinger, pulsing at a fixed repetition rate, went down to the pre-defined maximum depth and was then raised back to the surface. The movement was stopped for a maximum of 5 minutes at selected instrumented SPATS levels. During these stops, the pinger signal was recorded for 18 s at a sampling frequency of 200 kHz by all three channels of the sensor module simultaneously. A string completed a loop over all sensor modules in less than 4 min. The four SPATS strings can record the same module at the same time within 10 ms due to the NTP synchronisation and the fact that the data-taking script is restarted every 4 min.

³Model ITC-1001 from the International Transducer Corporation. <http://www.itc-transducers.com/>



(a)



(b)

Figure 2.10: (a): View of the pinger stage. (b): Top view of the pinger going down in a water-filled IceCube hole, from [103].

First Pinger Season (2007/2008)

The first-generation pinger used the 1 pps pulse from the GPS as trigger for the HV-pulse and the maximum repetition rate 1 Hz. The pinger was deployed in 6 water-filled IceCube holes down to a maximum depth of 500 m. The data collected were found to be affected by many unforeseen effects; e.g. the pinger's lateral position in the hole was off-center and varying, so that the recorded waveforms were so unstable in amplitude that they could not be used to measure the attenuation length. The study of these data allowed for a better understanding of the systematics related to the pinger operation. The pinger data was used to measure the sound speed vs. depth in South Pole ice for both pressure waves (P waves) and shear waves (S waves) as explained in [104].

Second Pinger Season (2008/2009)

In the second season the pinger was equipped with mechanical centralizers, suitable to keep the acoustic emitter close to the central axis of the hole, see Fig. 2.10(a). This prevented the stage from swinging and stabilized the acoustic pulse transmitted in the ice. The pinger was deployed in four water-filled IceCube holes down to a maximum depth of 500 m. For the second-generation pinger, the APB routes the 1 pps signal to a GPS-synchronized pulse generator (frequency-multiplying) board called the LG-board⁴. The maximum repetition rate was set to 10 Hz. The modifications implemented in the hardware (electronics and mechanics) gave a high stability of the waveforms and an overall improvement of the signal-to-noise ratio that allowed the measurement of the acoustic attenuation length [105].

Third Pinger Season (2009/2010)

In the third season the centralized pinger was used in *burst* mode. The pinger was modified to emit lower bandwidth pulses at three well defined frequencies (30, 45, and 60 kHz) and deployed in three boreholes going down to 1000 m depth. The measured data are used to study the frequency dependence of the attenuation length and the sound speed in the South Pole ice. More details are presented in § 4.

2.4.4 Recent SPATS results

- **Sound speed**

The speed of sound was measured in the dense ice between 80 m and 500 m as a function of depth using the SPATS pinger setup, using the 2007/2008 pinger data. Fig. 2.11 shows the sound speed data points for both pressure and shear waves. The measured sound speed for the pressure (v_p) and shear (v_s) waves and their variation

⁴After its designer, Leif Gustafsson.

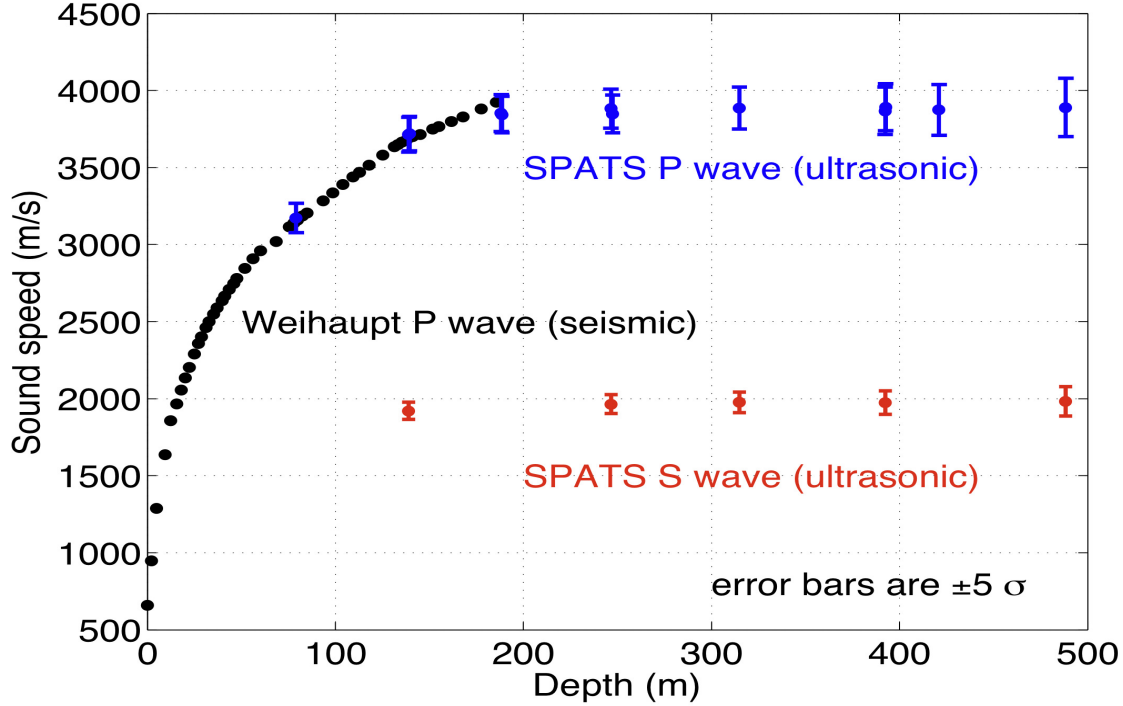


Figure 2.11: Sound speed for both pressure and shear waves, at ultrasonic frequencies, versus depth in the South Pole ice. A previous measurement, made by Weihaupt, at seismic (Hz) frequencies is shown for comparison. From [104].

with depth (gradient g) were found to be [104, 106]:

$$\begin{aligned} v_p(375\text{m}) &= (3878.3 \pm 12.2)\text{m/s}, \\ g_p &= (0.087 \pm 0.133)(\text{m/s})/\text{m}, \\ v_s(375\text{m}) &= (1975.0 \pm 8.0)\text{m/s}, \\ g_s &= (0.067 \pm 0.086)(\text{m/s})/\text{m}. \end{aligned}$$

Both sound speed measurements were performed with a better than 1% precision. The vertical sound speed gradient for both pressure and shear waves is consistent with zero and therefore there is no refraction between 200 m and 500 m depth. The negligible refraction of acoustic waves deeper than 200 m indicates that the neutrino direction and energy reconstruction, as well as separation from background events, could be done easily and accurately. More details can be found in [106, 104]. Analysis has been done using multi-frequency pinger data to investigate the frequency dependence of the sound speed, see § 4.8.

- **Properties of noise floor**

SPATS has monitored the noise in the ice at the geographic South Pole for more

than two years down to depths of 500 m. The noise is very stable and Gaussian distributed. The resulting noise level for all operative SPATS channels is presented in [48]. The contribution from electronic self-noise that has been measured in the laboratory prior to deployment is found to be 7 mPa. Subtracting this contribution quadratically from the measured mean noise level leads to an estimated mean noise level in South Polar ice of 20 mPa above 200 m and 14 mPa below 200 m integrated over the frequency range relevant for acoustic neutrino detection of 10 kHz to 50 kHz. The origin and significance of the decrease in the noise level with depth remains unclear. One possible qualitative explanation for the observed depth dependence is a contribution of noise generated on the surface. Due to the gradient in the sound speed with depth [104], all noise from the surface will be refracted back towards the surface, thus shielding deeper regions from surface noise.

- **Transient noise events**

Using a threshold trigger mode, the SPATS sensors registered acoustic pulse-like events from the IceCube detector volume and its vicinity. An offline coincidence window of 200 ms, corresponding to a pressure wave with the longest distance across the SPATS array of approximately 775 m, was used producing triggers on all four strings. The vertex positions for all transient events were reconstructed using an idealized global positioning system algorithm [48]. The horizontal positions of all reconstructed vertices are shown in Fig. 2.12. All sources of transient noise are well localized in space and have been identified as being man made; IceCube boreholes re-freezing after the deployment of the optical module produce cracking noise for a period of about 20 days. Rodriguez Wells, caverns melted in the ice at a depth of 50 m - 100 m as a water source for IceCube drilling, also produce a cracking noise during refreezing. The absence of any transient events observed from locations other than known sources allows a limit to be set on the flux of ultra high energy $E_\nu > 10^{20}$ eV neutrinos. Fig. 1.12 shows the neutrino flux-limit of the 2009 SPATS configuration (70 mPa threshold, ≥ 5 hits per event) compared to different neutrino flux limits [48].

- **Attenuation length**

The attenuation length was measured by three different analyses using the permanently frozen-in SPATS sensors on the four strings. The data sets from 2008/2009 were analyzed using different sound sources, the pinger, the frozen-in SPATS transmitters and transient signals from freezing IceCube holes to determine the attenuation length. All methods consistently deliver an attenuation length of ~ 300 m with a 20% uncertainty. More details about the different attenuation length analysis can be found in [105, 106, 107].

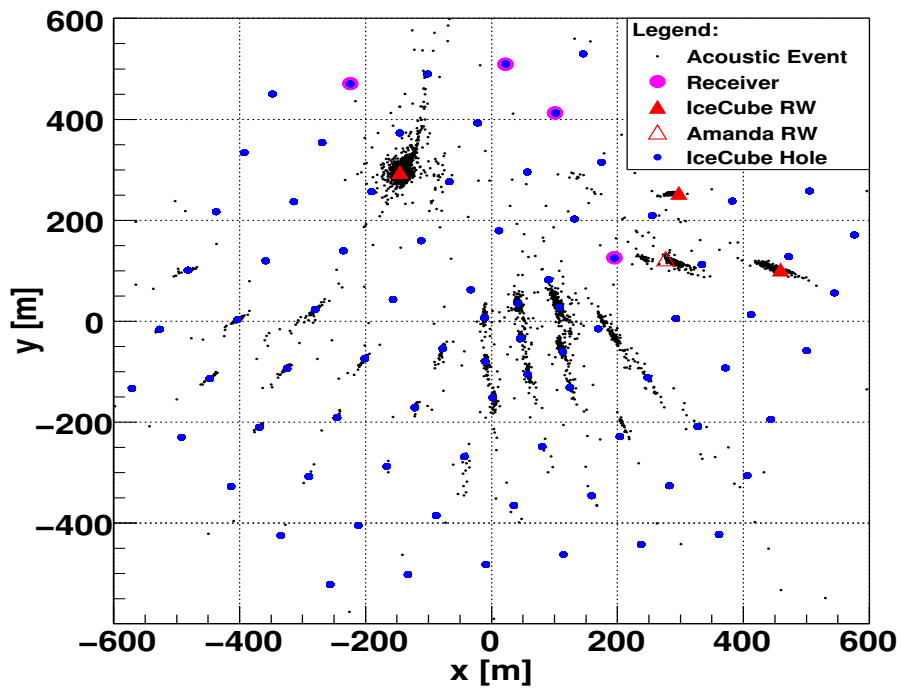


Figure 2.12: The vertex position for all transient events recorded since August 2008 in the horizontal plane of the the IceCube coordinate system. The sources of transient noise are the Rodriguez Wells (RW), large caverns melted in the ice for water storage during IceCube drilling, and the refreezing IceCube holes. Small circles: positions of IceCube holes, big circles: locations of SPATS strings, triangles: location of RW. From [48].

Acoustic Neutrino Detection

The acoustic detection of ultra-high energy neutrinos is based on the thermo-acoustic (or hydrodynamic) mechanism, first discussed by G. A. Askarian in 1957 [67]. The model was further discussed by G. A. Askarian and B. A. Dolgoshein [108], and J. Learned [109] and verified experimentally by L. Sulak and J. Learned [110]. This model describes the generating mechanism that gives rise to a detectable acoustic pulse when a neutrino interacts in a suitable target. The acoustic signal properties depend on the physical parameters of the interaction medium. The acoustic properties of ice, the medium of interest to this work, will be discussed. The predicted attenuation mechanism in ice will be presented too.

3.1 Thermo-acoustic model

According to the thermo-acoustic model, the energy deposition of particles traversing through liquids or solids is converted into acoustic energy by the thermal expansion of the medium. Knowing the medium parameters, the velocity of sound, the heat capacitance and the thermal expansion coefficient, one can calculate the acoustic pressure pulse which depends on the spatial and temporal development of the deposited energy density. In case of high energy neutrino detection, charged particles produce electromagnetic or hadronic cascades, that will pass through the medium (at about the speed of light) and deposit energy along their paths. The energy deposition in medium leads to a local heating along the cascade. This induces a fast expansion of the medium, which propagates as a shock wave perpendicular to the cascade axis, giving a bipolar acoustic signal. It is calculated that the cascade of particles deposits its energy over a cylinder with longitudinal extension $L \sim 10$ m and radial extension $2a \sim 10$ cm. The characteristic timescale τ_{hydro} of the energy dissipation by the hydrodynamic mechanism can be estimated as $\tau_{hydro} \sim 2a/v \sim 10^{-5}$ s, where v is the sound speed in ice. Shower particles propagate at about the speed of light c . The characteristic time of energy deposition can be estimated as $\tau_{dep} \sim L/c \sim 10^{-7}$ s. According to the time scales considered here, the energy deposition in the shower volume can be considered as being instantaneous relative to the energy dissipation processes.

- **Signal production in liquids**

In liquids, the differential wave equation that describes the acoustic signal is given

by [108, 109, 111]:

$$\Delta p(\vec{r}, t) - \frac{1}{v^2} \cdot \frac{\partial^2 p(\vec{r}, t)}{\partial t^2} = -\frac{\alpha}{C_p} \cdot \frac{\partial^2 q(\vec{r}', t)}{\partial t^2} \quad (3.1)$$

where $p(\vec{r}, t)$ is the pressure amplitude at a given space point \vec{r} and time t , v is the sound speed in the liquid, C_p is the heat capacity, α is the thermal expansion coefficient and $q(\vec{r}', t)$ is the energy deposition density.

A solution to Eq. 3.1 is given by the Kirchhoff integral [108]:

$$p(\vec{r}, t) = -\frac{\alpha}{4\pi C_p} \int \frac{dV'}{|\vec{r} - \vec{r}'|} \frac{\partial^2}{\partial t^2} q \left(\vec{r}', t - \frac{|\vec{r} - \vec{r}'|}{v} \right) \quad (3.2)$$

where $\frac{|\vec{r} - \vec{r}'|}{v}$ is the travel time of the acoustic signal. The pressure amplitude at a certain time t and space point \vec{r} depends on the energy deposit at another point \vec{r}' .

For a neutrino induced cascade, the energy deposition can be regarded as being instantaneous compared to the time scales of the other processes involved (thermal and acoustic time scales). The energy deposit can be approximated by a space dependent component and a step function in time,

$$\frac{\partial}{\partial t} q(\vec{r}', t) = q(\vec{r}') \delta(t - t_o) \quad (3.3)$$

where t_o is the time of the neutrino interaction.

Then the pressure amplitude is given by:

$$p(\vec{r}, t) = -\frac{\alpha}{4\pi C_p} v^2 \frac{\partial}{\partial R} \int_{S_r^R} \frac{q(\vec{r}')}{R} d\sigma' \quad (3.4)$$

where the integration is performed over the surface of a sphere with radius $R = vt$, at a time t , and whose center is at the detection point with spatial coordinates \vec{r} .

The pressure amplitude can be expressed as:

$$p(\vec{r}, t) = -\frac{\gamma_G}{4\pi} \frac{\partial}{\partial R} \int_{S_r^R} \frac{q(\vec{r}')}{R} d\sigma' \quad (3.5)$$

where γ_G is the *Grüneisen parameter* given by:

$$\gamma_G = \frac{\alpha}{C_p} v^2 \quad (3.6)$$

For water, in a very simplified model [108], the cascade of particles is assumed to deposit its energy homogeneously inside a cylindrical volume with length L and diameter d , see Fig. 3.1. The dominant frequency is given by the maximal coherence length across the shower, which corresponds to half a wavelength: $f_{\text{peak}} = v/d$.

The frequency component, at an optimal angle ($L \cos \theta / \lambda < 1$), of the sound pressure for the near-field is given by [108]:

$$|p(f)| \sim \frac{f}{a\pi^2} \frac{\alpha}{C_p} \frac{E}{\sqrt{R}} \quad (3.7)$$

where f is the frequency and E is the cascade energy. The frequency component of the sound pressure for the far-field is given by [108]:

$$|p(f)| = \frac{f}{4\pi^2} \frac{\alpha}{C_p} \frac{E \sin X}{R X} \quad (3.8)$$

where $X = \lambda/2\pi < \cos \theta$. In the cylindrical approach, the radiation will be coherent for $f < f_{\text{peak}} = v/d$, where $d \sim 2a$ approximates the diameter of the energy deposition region. The peak frequency f_{peak} is about 25 kHz [108] and the duration of the pulse is $\tau \sim d/v = 1/f_{\text{peak}}$, which is about 10^{-5} s.

- **Signal production in solids**

Thermo-acoustic excitation from deposited energy in an isotropic solid target gives rise to stress which produces two types of elastic waves. The first one is called longitudinal or pressure waves, often referred to as P (primary), where the wave particles move along the direction of propagation in the medium as shown in Fig. 3.2(a). The second one is called transverse, rotational or shear waves, often referred to as S (secondary) waves, where the wave particles move perpendicular to the direction of propagation in the medium as shown in Fig. 3.2(b).

Since the South Pole ice is not isotropic, elastic waves are not pure longitudinal or transverse waves but are some form of mixed waves and called quasi-longitudinal and quasi-transverse waves. A quasi-longitudinal wave is not a pure longitudinal wave. It consists of both longitudinal and transverse components. However the transverse component has a small contribution.

Since the distance from the region of sound generation to the free boundaries of the South Pole ice is large, the quasi-transverse waves reflected from these boundaries can be neglected. Quasi-longitudinal waves will be the dominant mode that can be excited thermo-acoustically in ice, while only a very small fraction of the energy will be converted into transverse modes due to the dynamic mechanism of sound generation. In [112] it is also shown that the level of shear stress caused by transverse waves is much smaller than the corresponding longitudinal wave pressure for the same observation point. For the quasi-longitudinal mode, the differential wave

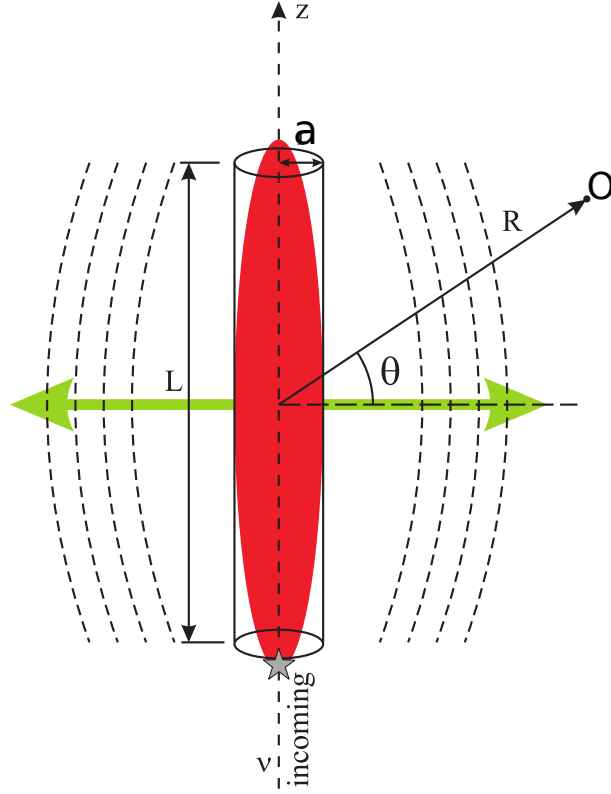


Figure 3.1: Schematic drawing of neutrino-induced cascade. The cascade energy is assumed to be deposited homogeneously inside a cylindrical volume with length L and radius a .

equation that describes the acoustic signal is given by [100],

$$\Delta T(\vec{r}, t) - \frac{1}{v^2} \cdot \frac{\partial^2 T(\vec{r}, t)}{\partial t^2} = -\frac{\alpha}{C_p} \cdot \frac{\partial^2 q(\vec{r}', t)}{\partial t^2} \quad (3.9)$$

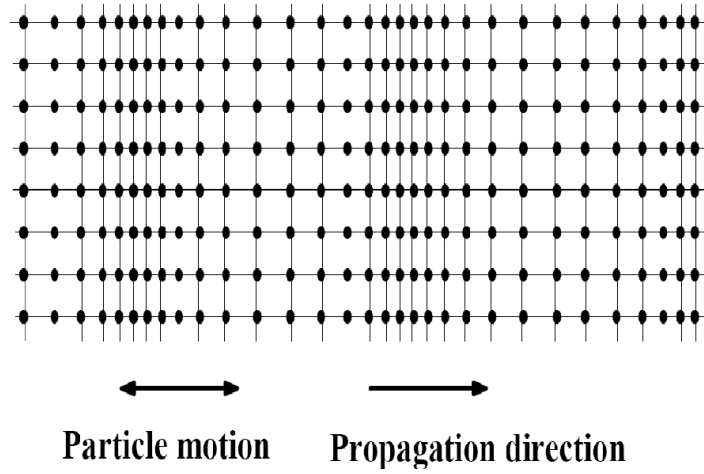
where T , the *normal traction* (similar to the scalar pressure) gives the perpendicular force exerted on the surface. Since eq. 3.9 has the same form as eq. 3.1, the same solution as shown for liquids will therefore hold also for ice. A high energy cascade will create a bipolar pulse restricted to the plane perpendicular to the cascade.

By using a different approach, the effective sound pressure was calculated in [112] for both the far-field and near-field.

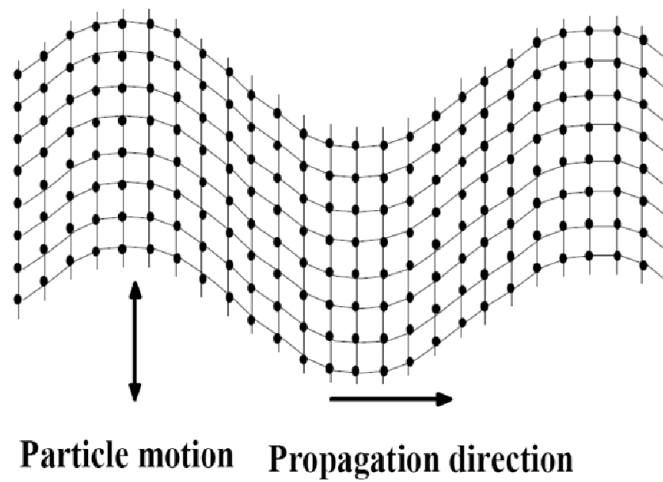
In the near-field case ($R < 100$ m), the effective longitudinal sound pressure in ice can then be derived [112]:

$$p_{\text{eff}} \sim \frac{E}{E_0} \frac{1}{\sqrt{R}} \quad (3.10)$$

where $E_0 = 10^{16}$ eV and p_{eff} is in Pa. ($E(x')$) In the far-field case ($R > 100$ m),



(a)



(b)

Figure 3.2: (a): Longitudinal waves particles move along the direction of propagation.
(b): Transverse waves particles move perpendicular to the direction of propagation.

where the observation point is close to the plane perpendicular to the cascade axis, an estimation for the effective sound pressure in ice is [112]:

$$p_{\text{eff}} \sim 10^{-1} \frac{E}{E_0} \frac{1}{R} \quad (3.11)$$

In the far-field case, where the observation point is at any angle (except for those close to the plane perpendicular to the cascade-axis), the effective sound pressure is given by [112]:

$$p_{\text{eff}} \sim 10^{-5} \frac{E}{E_0} \frac{1}{R} \quad (3.12)$$

Therefore the far-field effective pressure drops significantly when the observation point is not close to the plane that is perpendicular to the cascade-axis: the pressure field has a “pancake-shape”.

3.2 Acoustic signal production

When high-energy neutrinos interact in dense media (water or ice), a hadronic (or electromagnetic) cascade is produced, which heats a long, thin volume of the medium as shown in Fig. 3.1. This volume is on the order of 10 cm in diameter and 10 m in length. The instantaneous thermal energy is deposited faster than both the thermal and acoustic time scales. This rapid heating produces a pancake-shaped shock front that will propagate perpendicularly to the cascade-axis. The acoustic pulse expands outward from the cascade-axis in a ring shape, illuminating a disk of the medium perpendicular to the cascade. To build an acoustic high-energy neutrino detector, it is important to understand the properties of the acoustic signal and its propagation through the detector medium.

From eq. 3.5 it can be seen that the acoustic signal amplitude depends on the Grüneisen parameter. Figure 3.3 shows the acoustic bipolar pulse from a high-energy neutrino interaction in water and ice. The acoustic pulse height in ice is one order of magnitude higher than its value in water for a certain energy deposition density $q(\vec{r}')$, since γ_G in ice $\gg \gamma_G$ in water.

As shown in [112], the near-field and far-field give the same behaviour in liquids and in solids. The acoustic signal scales linearly with the total deposited energy in both cases. The effective sound pressure created at the shower in ice is expected to be approximately one order of magnitude higher than the effective sound pressure in water, other conditions (like shower length and radius) being close to equal. For the simulations presented in [113], the in-ice pulses are about a factor 6 larger than the in-water pulses. This difference is mainly caused by the fact that the Grüneisen parameter for ice is about a factor 7 larger than that for ocean water, see Table 3.1.

3.2. Acoustic signal production

	ocean	ice	salt
T [°C]	15	-51	30
v [m s ⁻¹]	1530	3920	4560
α [K ⁻¹]	2.555×10^{-4}	1.25×10^{-4}	1.16×10^{-4}
C_p [J kg ⁻¹ K ⁻¹]	3900	1720	839
$\gamma_G = v^2 \frac{\alpha}{C_p}$	0.15	1.12	2.87

Table 3.1: Grüneisen parameter γ_G for ocean-water, ice and salt [4].

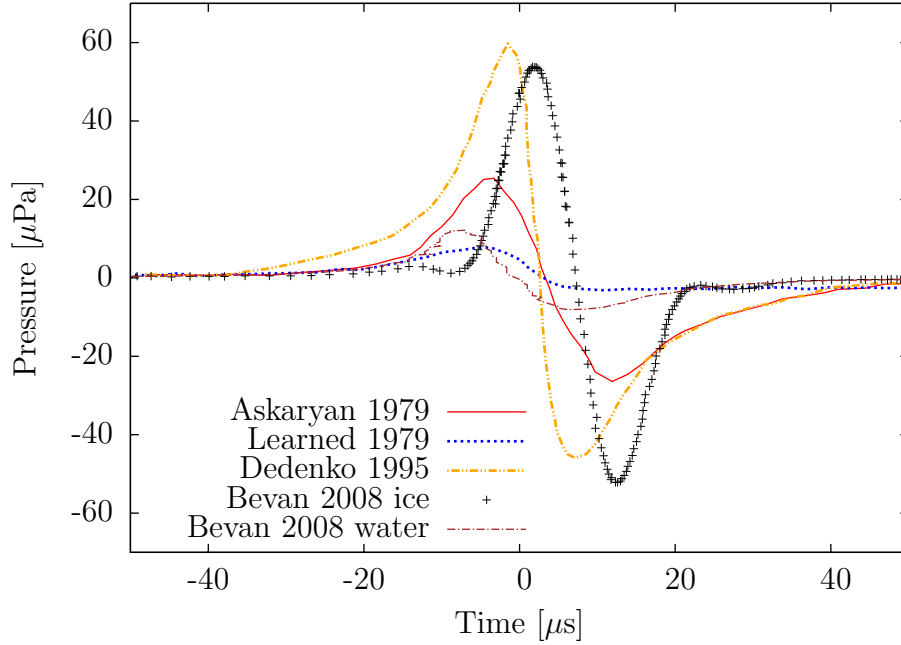


Figure 3.3: Time profile of the acoustic bipolar pulse in water at a perpendicular 400 m distance for a primary neutrino energy of $E_\nu=10$ PeV (Dedenko, Learned and Askarian) and in ice and water at distance of 1 km for $E_\nu=10$ PeV (Bevan). The in-ice pulse was delayed and scattering-dominated attenuation was applied. Adapted from [113] and [114]. From [107].

The specific solutions discussed for liquids (like the cylindrical approximation) are also applicable to the in-ice calculations [112]. This means that pulse duration τ and peak frequency f_{peak} both scale with the sound speed in ice. Therefore the pulse length in ice is expected to be shorter than for water. Similarly the expected peak frequency is higher for ice than for water.

3.2.1 Acoustic signal properties

Experimental and simulation efforts continue to be carried out on understanding the properties of the acoustic signal which are expected from a neutrino-induced high-energy cascade. The main expected signal properties are:

- The acoustic signal has a bipolar shape with a duration that depends on the radial dimension of the shower (inversely proportional) and the sound velocity (directly proportional). As shown in Fig. 3.3, the pulse is narrower in ice than in water.
- The acoustic signal peak frequency is expected to be higher in ice than in the ocean water. In ocean water, the mean frequency at 1 km distance is about 20 kHz. This depends on distance due to frequency-dependent absorption effects in ocean water. For ice, the mean frequency is claimed to be around 40 kHz in [113] and 90 kHz in [112].
- The acoustic pressure amplitude increases linearly with the deposited shower energy and therefore with the neutrino-induced cascade energy E_ν .
- The acoustic pressure amplitude increases linearly with the *Grüneisen parameter* (γ_G) which depends on the medium properties.
- The acoustic pressure amplitude depends on the distance to the shower-axis. In near-field, the shower is seen as a line-source and the amplitude scales with $1/\sqrt{R}$, where R is the distance to the shower-axis. In the far-field, the shower is seen as a point-source and the amplitude scales with $1/R$.

3.3 Ice properties

Ice is a naturally occurring crystalline inorganic solid with an ordered structure. It possesses a regular crystalline structure based on the molecule of water, which consists of a single oxygen atom covalently bonded to two hydrogen atoms, or H-O-H. It exists in about thirteen crystalline structures. All natural snow and ice on Earth have a well known hexagonal structure (called ice-Ih) with a density of 0.917 g/cm³ at 0 °C [115, 116]. Only a small amount of ice, found in the upper atmosphere, has a cubic structure (called cubic ice). Figure 3.4(a) shows the phase diagram of water, illustrating the pressure and temperature conditions under which different crystal structures of ice are stable.

Antarctica is Earth's southernmost continent, encapsulating the South Pole. About 98% of Antarctica is covered by the Antarctic ice sheet, a sheet of ice averaging at least 1.6 km thick and flows in the direction of the coast with a speed of about 10 m/year. The continent has about 90% of the world's ice. It grows at a rate of about 2.5 cm/year from the precipitation of very small ice crystals that formed due to the very low humidity. The snow densifies with depth due to pressure until it reaches maximum density at a depth of around 200 m. The upper region of the ice-sheet where the snow compactifies to ice is

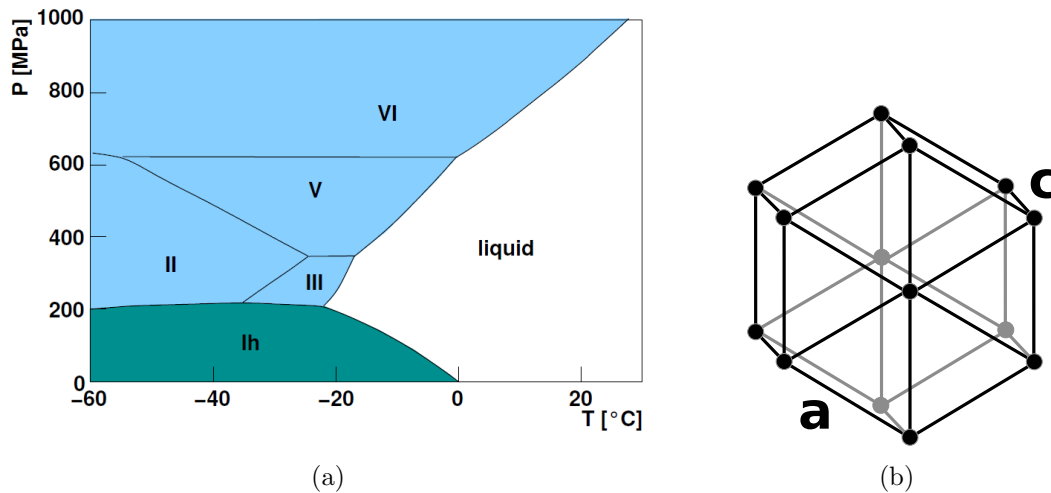


Figure 3.4: (a): The phase diagram of water/ice, illustrating the pressure and temperature conditions under which different crystal structures of ice are stable. (b): The hexagonal structure of ice-Ih with the c and a axis indicated.

called the firn. In this region, the ice becomes increasingly stiff due to scintering [117]. With increasing depth and pressure, air gaps close off and get smaller, while at the same time the crystal size is growing. At around 1400 m and below all bubbles convert into the clathrate phase, leaving a very homogeneous medium [118].

In an ice crystal the water molecules are arranged in layers of hexagonal rings. These layers are called the basal planes of the crystal, and the normal to the basal plane is called the c-axis or the optical axis of the crystal, see Fig. 3.4(b). The bonds between molecules situated in the same basal plane are much stronger than the bonds between molecules located in different basal planes. This causes the ice crystal to deform by gliding on its basal planes. Glacier ice is built up from many individual ice crystals that are packed closely together. In the top of an ice sheet the ice crystals are randomly oriented because the snow flakes have settled randomly. Some crystals are oriented favorably for basal gliding and others are not. This means that the deformation proceeds much more slowly than for a single ice crystal. As the ice deforms, the individual crystals in the ice slowly change shape as the basal planes glide past each other, just like a deck of cards changes shape when it is pushed from one side. This causes the individual crystals to rotate. Generally, the c-axes of the crystals rotate towards an axis of compression and away from an axis of extension. The effect of this is that deep down in the ice sheet the crystals are no longer randomly oriented but have a preferred direction. The colour scale of the crystal varying with its orientation as shown in Fig. 3.5.

Figure 3.6(a) shows the density profile of the upper layers of South Pole Ice [99]. The density profile from borehole measurements and seismic measurements [120] shows a strong increase in the upper layers, while the density reaches a maximum when the pressure gets high enough to compress the air gaps. Figure 3.6(b) shows a temperature



Figure 3.5: Glacier ice crystal structure at a few hundred meters depth (left) and at ~ 1500 m depth (right). In the top of the ice sheet the crystals have random orientation, so the crystals have many different colours. Deeper down, the ice crystals have a preferred direction and therefore most of the crystals have similar colours. The colour scale vary with the crystal axis orientation. From [119].

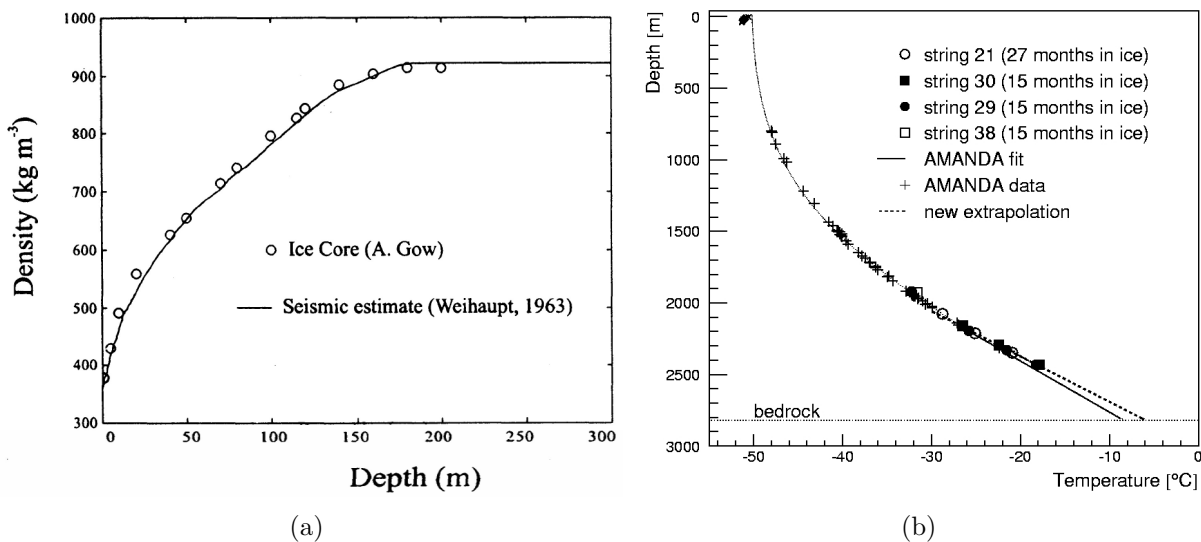


Figure 3.6: (a): Density profile of the upper layers in Antarctic ice at South Pole (from [99]). (b): South Pole ice-cap vertical temperature profile (IceCube internal document). Temperatures measured in deep AMANDA boreholes (+, measured data) and in a shallow borehole (x, Giovinetto [1960]), compared with best-fit temperature profile for the deepest 1,000 m.

profile of antarctic ice at South Pole. The temperature is lowest at shallow depth and increases towards the bottom. The temperature profile of the ice cap is dominated by heating due to the natural heat originating from Earth's crust. The temperature of the South Pole ice has been experimentally determined to increase from $\sim -51^\circ\text{C}$ just below the surface to an extrapolated $\sim -9^\circ\text{C}$ at 2800 m depth, close to the bedrock, see Fig. 3.6(b). The temperature of ice below 10 m is stable. No short-term effect on the

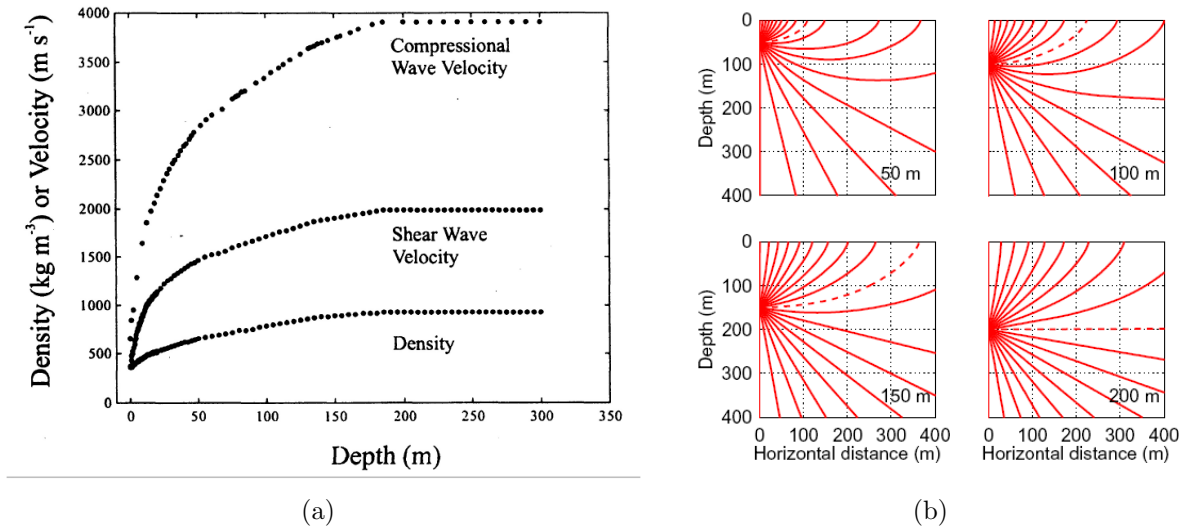


Figure 3.7: (a): Pressure wave velocity measurements at the South Pole [120], along with the shear wave velocity and density values that were derived from pressure wave measurements [99]. (b): Calculated pressure wave ray trajectories using the measured sound speed in South Pole ice as a function of depth. Each panel shows rays emitted from a source at 50, 100, 150, or 200 m. Rays are emitted every 10° from vertically upward to vertically downward. The horizontally emitted ray is indicated by a dashed line [104].

ice temperature is noticed due to seasonal and long-period temperature changes at the surface. The conductivity of ice is low and changes in temperature at the surface are attenuated exponentially with depth, so that only very-long period climatic variations can penetrate the ice for a few meters with very low amplitude [98].

3.3.1 Sound speed

Many attempts were made to measure the sound speed in South Pole ice. Sound speed in a specific medium depends on its density, temperature and grain orientation. Both longitudinal and transverse sound velocity can be derived using temperature and density profiles. As shown in Fig. 3.7(a), the derived sound speed increases in the firn as the ice becomes gradually more rigid (stiffer) due to the increasing density [99] and it is in very good agreement to the seismic measurements by J. G. Weihaupt [120]. For larger depths (below the firn), the density is stable and the speed of sound can be modelled assuming a certain temperature-dependent coefficient ($-2.3 \text{ m}/(\text{s}^\circ\text{C})$) [99].

In monocrystalline ice the sound speed depends on the direction of propagation relative to the crystal axis (i.e. the orientation of an ice crystal). Fig. 3.8 shows the dependence of the pressure acoustic wave velocity on the propagation angle relative to the c-axis in single crystal ice at depth of 1 km at South Pole. The sound speed was predicted to vary

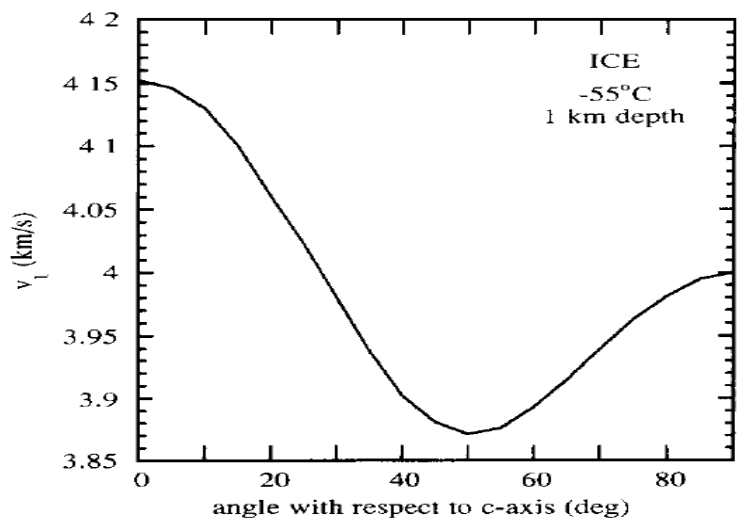


Figure 3.8: Sound speed versus the propagation angle relative to the c-axis in single crystal ice at depth of 1 km at South Pole. From [121].

by 7% depending on the propagation angle relative the c-axis [121]. The South Pole ice is polycrystalline with predicted random distribution of c-axis orientations, so that this effect averages out and leads to a uniform propagation speed [98]. Sound speed is assumed to be frequency independent, so that comparisons with sound speed results obtained from seismic measurements, are possible.

3.3.2 Refraction

Sound refraction depends on the medium density and therefore on the gradient of the sound speed [4]. For South Pole ice, in the firn, the sound speed increases with depth which gives a large speed gradient and all waves will be strongly bent towards the surface because of the ray refraction. As shown in Fig. 3.7(b), waves are bent toward regions of lower propagation speed [104]. In the bulk ice, below the firn, the sound speed is constant and therefore the refraction is negligible and all waves will propagate on nearly straight lines. Bulk ice is considered as a region of interest to build an acoustic array while the firn layer acts as a shield refracting any sound waves from any source of surface background noise.

3.3.3 Ambient noise

The ambient noise in the South Pole ice is expected to be low and stable. It is expected that the motion of the Antarctic glacier over the bedrock may provide a source of acoustic background noise from ~ 0.01 MHz to 1 MHz [4]. Anthropogenic surface noise sources is expected to provide a source of acoustic background noise. Both surface and bedrock noise

are not expected to reach the depths that are relevant for acoustic neutrino detection due to the sound speed gradient. Any ambient noise should be easily rejected by the arrival direction of the wave front in any detector array design. Also, the unique signature of the acoustic signal helps to recognize it from the background noise. Compared to ocean water, South Pole ice is predicted to be much quieter because there are no waves, currents or animals in ice.

3.3.4 Acoustic signal propagation

According to the theory developed in [4], the amplitude of the acoustic signal in ice is attenuated via scattering and absorption by a factor of $(e^{-d/\lambda})$, where d is the distance travelled by the acoustic wave and λ is the attenuation length. The total attenuation length, which is a combination of absorption length (λ_{abs}) and scattering length (λ_{scat}), is calculated by:

$$\frac{1}{\lambda} = \frac{1}{\lambda_{abs}} + \frac{1}{\lambda_{scat}} \quad (3.13)$$

Absorption

There are two main absorption mechanisms for longitudinal waves in the South Pole ice [4]. In warm ice, below 2000 m near the bedrock, the absorption is dominated by grain boundary sliding. While in cold ice, in the upper 2000 m where the ultrahigh-energy neutrino acoustic detector is considered, the absorption is dominated by proton reorientation. In the proton reorientation process, the dipole moment of the H₂O molecule may assume one of six directions in the ice crystal. This leads to a temperature dependent energy loss of the acoustic wave in internal friction. The dominant effect for this energy loss had been assumed to be connected to changes of the orientations of the dipole moments of H₂O molecules and to movements of protons from one bond site to another in response to the acoustic wave. This energy loss is characterized by a mechanical relaxation time τ_m which depends on the temperature T following the relation;

$$\tau_m = \tau_0 e^{U/kT} \quad (3.14)$$

where $U = 0.58$ eV is the activation energy, $\tau_0 = 3 \cdot 10^{-16}$ s is the relaxation constant and k is Boltzman constant. The effective absorption coefficient, $\alpha = 1/\lambda$ and λ is the attenuation length, for longitudinal waves is derived by [121]:

$$\alpha_{abs} = \frac{\delta_m 2\pi f^2 \tau_m}{(1 + 4\pi^2 f^2 \tau_m^2)c} \text{ [m}^{-1}\text{]} \quad (3.15)$$

where δ_m is an experimentally determined constant that is dependent on the wave mode and the propagation direction but not on the frequency f . The absorption coefficient increases with frequency up to $f_m = 1/2\pi \tau_m$, while for $f > f_m$ it is independent of frequency.

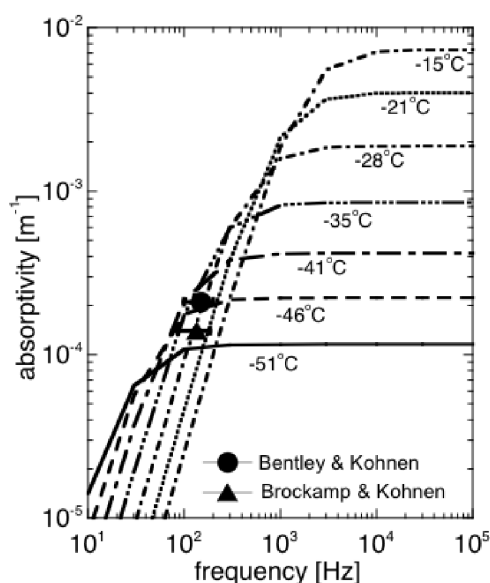


Figure 3.9: Calculated absorptivity in glacial ice as a function of frequency for different temperatures. See [4] for references (from [121]).

Figure 3.9 shows temperature- and frequency-dependent absorptivity in ice. Two data-points are indicated originating from seismic measurements in an Antarctic glacier (solid circle) and Greenland ice (solid triangle). Above 100 kHz, even for high temperatures no dependence of the absorption on frequency is expected. The range of predicted absorption lengths at near-surface temperature (-51°C) in South Pole ice, calculated from different measurements of U , τ_0 and δ_m , is roughly from 5 km to 11 km.

Scattering

In addition to absorption, scattering has to be taken into that to calculate the effective attenuation length for the South Pole ice. Scattering means the pressure wave is deviated, with or without energy loss, from its straight trajectory due to non-homogeneity of the medium. The main sources of scattering in ice are bubbles and grain boundaries [4].

- **Scattering at bubbles:** Below 1400 m all bubbles have converted into the solid clathrate crystals with density similar to ice so that the clathrate do not contribute as scatterers. The clathrate phase consists of a cubic crystal structure in which O_2 and N_2 molecules from air are trapped in clathrate cages. At shallower depths, where bubbles do occur, the individual bubbles act as independent scatterers, since the mean spacing between the bubbles is many times larger than their mean dimensions. The attenuation coefficient for scattering in South Pole ice for a certain frequency

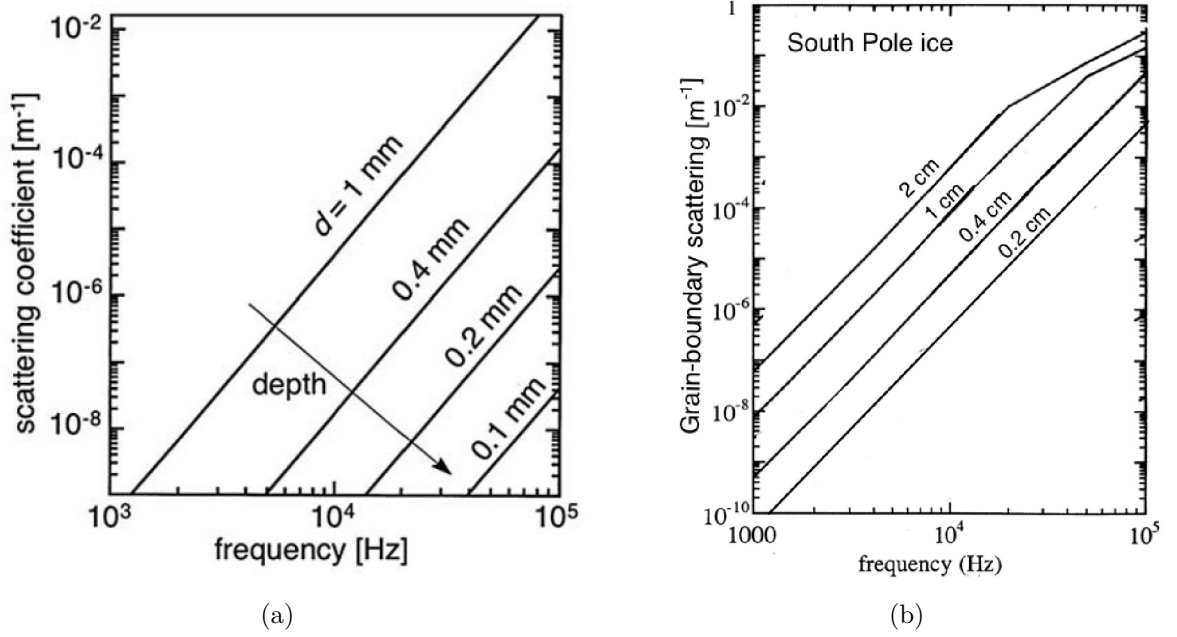


Figure 3.10: (a): Calculated scattering for air bubbles in glacial ice as a function of frequency for different depths. (b): Calculated scattering at grain boundaries as a function of frequency and grain diameter in South Pole ice (from [121]).

f following Rayleigh regime is derived by [4]:

$$\alpha_{\text{scat}}^{\text{bubble}} = 2.68 \cdot 10^{-10} \left(\frac{n_0}{200 \text{ cm}^{-3}} \right) \left(\frac{d_b}{0.02 \text{ cm}} \right)^6 \left(\frac{f}{10 \text{ kHz}} \right)^4 [\text{m}^{-1}] \quad (3.16)$$

where n_0 is the bubble density, d_b is the bubble diameter and f is the frequency. Figure 3.10(a) shows the scattering coefficient due to the scattering at the air bubbles as a function of frequency for different depths in South Pole ice. The bubble density was measured using deep core ice samples taken at Byrd Station. The maximum density of bubbles was reached at a depth of ~ 100 m where the ice contained air bubbles with a concentration n_0 of about 200 cm^{-3} [121]. The mean bubble diameter, d_b , for the Byrd Station ice core was found to be ~ 0.05 cm near the surface and ~ 0.008 cm at about 1 km depth [121].

- Scattering from grain boundaries:** Water ice freezes into crystal clusters called grains. The grain structure of the ice is determined by the conditions of the ice when it freezes. The crystal grain size increases with depth due to increasing pressure. The sound speed depends on the specific direction of the wave relative to the crystal axis. The polycrystalline ice at the South Pole consists of monocrystals that have random orientation and a certain mean grain diameter, therefore scattering of the acoustic waves will happen at the grain boundaries. Scattering occurs at grain

boundaries due to abrupt change in the acoustic speed. While some part of the acoustic wave is reflected, another part is converted from longitudinal to transverse modes and vice-versa. Here we only consider the attenuation of the longitudinal waves. The scattering of acoustic waves depends strongly on the grain size and the considered wavelength. Therefore there are three scattering regimes for scattering at grain boundaries in ice [4, 121];

1. **Rayleigh regime** ($\lambda/2\pi d_g > 1$, where λ is the wavelength)

The scattering is situated in the Rayleigh regime when the wavelength is much greater than the grain diameter d_g . The wavelength is a few tens of centimeters within the frequency range of the acoustic detection of neutrinos (up to 100 kHz) and therefore much larger than the measured grain size, so that the scattering is situated in the Rayleigh regime. The effective scattering coefficient, assuming a random orientation of the c-axis, for longitudinal waves is given by:

$$\alpha_{\text{scat}}^{\text{grain}} = 5 \cdot 10^{-4} \left(\frac{d_g}{0.2 \text{ cm}} \right)^3 \left(\frac{f}{10 \text{ kHz}} \right)^4 [\text{km}^{-1}] \quad (3.17)$$

2. **Stochastic regime** ($0.5 < \lambda/2\pi d_g < 1$)

The scattering coefficient is given by:

$$\alpha_{\text{scat}}^{\text{grain}} = 6.2 \left(\frac{d_g}{0.2 \text{ cm}} \right) \left(\frac{f}{500 \text{ kHz}} \right)^2 [\text{m}^{-1}]. \quad (3.18)$$

This scattering regime shows a weak dependency on d_g and the frequency, f , due to the coherent nature of the scattering process, because of a noticeable phase-shift of the acoustic wave over a distance $\sim d_g$.

3. **Geometric regime** ($\lambda/2\pi d_g < 0.5$)

In this scattering regime, the scattering mechanism approaches a diffusion process and the resulting scattering is independent of frequency and proportional to the average reflection coefficient $\langle R \rangle$. The scattering coefficient is given by:

$$\alpha_{\text{scat}}^{\text{grain}} = \langle R \rangle / d_g \quad (3.19)$$

In ice, the elastic anisotropy of individual crystal grains is small, the average reflection coefficient is given by $\langle R \rangle = 0.068$ [121], and $\alpha = 6.0/(d_g [\text{cm}]) [\text{m}^{-1}]$.

Figure 3.10(b) shows the scattering coefficient due to the grain boundaries as a function of frequency for different grain diameter in South Pole ice. According to the theory [4, 121], in ice with $d_g = 0.2 \text{ cm}$, the predicted scattering length is 2000 km at 10 kHz, 25 km at 30 kHz, and 2 km at 60 kHz. The acoustic attenuation length in the shallow ice below the firn is predicted to be dominated by the proton reorientation absorptive effect and to be $9 \pm 3 \text{ km}$.

3.3. Ice properties

Recently, the grain sizes were measured from 148 m to 291 m in a SPRESO (South Pole Remote Earth Science Observatory) ice core about 8 km from South Pole [122]. The mean radius was derived to be 1.77 mm at depths ≥ 148 m that overlap with depths where SPATS has measured the acoustic attenuation. Also, the new measurements of grain size show no dependence on depth, which is consistent with the SPATS attenuation length which does not depend on depth in the interval 200 m to 500 m. Taking into account the new grain size measurements and the fact that Rayleigh scattering of acoustic waves at grain boundaries varies as the fourth moment of the wavelength, the attenuation rate is predicted to be 0.003 m^{-1} between 10 kHz to 30 kHz in glacial ice at -51°C [122].

Based on the thermo-acoustic mechanism, the acoustic signal from the interaction of UHE neutrino in ice can be produced. The properties of the acoustic signal depend on the physical parameters of ice. Below the shallow ice, ice is considered as a suitable medium to build an acoustic array while the firn layer acts as a shield reflecting any noise from the surface. On the other hand, the sound speed is constant with depth and the reflection is negligible. The acoustic attenuation length was predicted to be about 9 km and dominated by scattering. In-situ measurements by SPATS shows that the attenuation length is about 300 m.

Pinger data analysis

The previous data sets, before the 2009/2010 pinger season, did not allow a distinction between absorption- or scatter-dominated attenuation length. The theory predicted that absorption is frequency independent, while scattering is expected to increase as f^4 . The new frequency dependent measurements are used to distinguish between the two attenuation mechanisms. Also, frequency dependent studies of sound speed and the ice fabric (e.g. the grain orientation as a function of position in a glacier) are done using the same data set.

4.1 Geometry

The pinger holes were chosen to be aligned as much as possible, see Fig. 2.8, in the same direction with respect to the SPATS strings location to minimize the azimuthal variation at horizontal distances between 180 m and 820 m. See Table 4.1 for the complete list of distances. The pinger was stopped at the predefined depths shown in Table 4.2, going down to 1000 m depth.

<i>Pinger Hole</i>	<i>String-A</i>	<i>String-B</i>	<i>String-C</i>	<i>String-D</i>
81	474.7	381.9	177.9	509.8
25	696.0	625.0	434.1	649.5
16	819.7	750.0	549.1	760.3

Table 4.1: Distances, in meters, between pinger holes and SPATS strings.

<i>Pinger Hole</i>	<i>Depths(m)</i>				
81	140	250	320	540	666
25	140	250	320	740	872
16	140	250	320	797	1000

Table 4.2: Stops, in meters, for different pinger holes.

4.1.1 Depth Measurements

Three methods were used to measure the pinger depth: the *Robertson winch* (RW) turn-counting, the RW cable payout system and the SeaStar sensors. Two SeaStar¹ sensors were used to measure the pinger depth. SeaStar sensors were installed on the pinger stage to measure the pinger depth at each nominal stop. These SeaStar sensors are miniature stand-alone data loggers that record temperature and pressure. They were always attached to the pinger stage at the same location, about 1.4 m above the pinger piezo-ceramic element. The pressure and temperature were recorded continuously with a time that was synchronized with a GPS-synchronised NTP (Network Time Protocol) server. The SeaStar raw data states the pressure in bar. To get the actual depth of the pinger transducer, the following formula is applied:

$$D_p = (P - P_0)C - D_w - l \quad (4.1)$$

where P is the raw pressure data recorded by the SeaStar sensor, P_0 is the pressure when the SeaStar is at about 0.4 °C (but not in water) before the actual deployment; D_w is the distance from the floor of the Tower Operation Structure (TOS) to the surface of the water in the hole (well-depth), l is the distance from the SeaStar to the pinger piezo-ceramic element (1.4 m on all occasions) and C is the conversion constant (1 bar = 10.19716213 m of water).

The payout depth measurement consists of a small wheel resting on top of the RW cable. The wheel turns when the cable is lowered or raised. A counter then indicates the length of cable that has been unspooled. The payout was set to 0 when the pinger transducer was positioned at TOS floor-level. A possible systematic error on this depth measurement can come from slipping of the cable over the wheel. This means that the cable will go over without turning the wheel, thus making the payout underestimate the amount of cable that passed by. Slippage can happen both in the down-going and up-going movement of the cable. Therefore, the payout offset, when the pinger transducer is back at TOS floor-level after pinging, could be interpreted as the maximum error due to slippage. This offset was recorded for different holes and was found to be about 1.5 m in average. Another possible source of error in the payout depth measurement is the fact that the payout device could be badly calibrated. The calibration was checked by estimating the pinger depth using the RW turn-counting and cross-checking it with the payout depth measurement.

Fig. 4.1 and Table 4.3 show the SeaStar and RW payout depth measurements for hole 16. The discrepancy between the depth measurements by SeaStar sensors can be due to differences in calibration and possibly different temperature-dependences. The average depth from the two SeaStars are in agreement within their uncertainty. Since the payout and turn-counting depth measurements agreed, the payout depth measurement is considered to be more accurate than the SeaStar measurement. The error in depth was estimated to be on the order of ± 2 m. Therefore, the payout measurement was taken as the pinger depth with a very conservative error of ± 5 m.

¹with serial numbers 4507 and 4509.

4.2. Laboratory tests

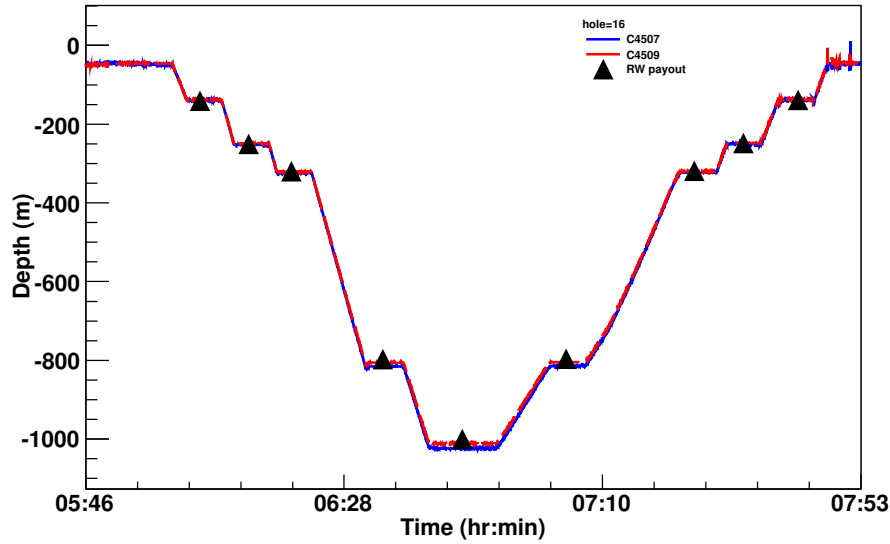


Figure 4.1: The SeaStar (C4507 and C4509) and RW payout depth measurements for hole 16. The two depth measurements are in agreement.

<i>Nominal depth</i>	<i>Depth from payout</i>	<i>Depth from SeaStar</i>
140	140.025	138.097 ± 0.91
250	249.845	249.843 ± 1.78
320	319.888	321.622 ± 1.63
797	797.052	807.465 ± 4.92
1000	1000.02	1015.95 ± 6.21
797	796.29	806.86 ± 4.64
320	318.272	320.39 ± 1.16
250	247.985	248.36 ± 1.33
140	138.196	136.96 ± 0.62

Table 4.3: Nominal and measured stopping pinger depths for Hole 16. Depth from the payout is the one calculated from the turn-counter on the winch. Depth from SeaStar is the average of the two SeaStar pressure values and the error shown is the maximum error calculated. All depths are in meter.

4.2 Laboratory tests

The acoustic signal from the pinger was studied to estimate if the signal would be strong enough to be seen in ice. Therefore the emitted acoustic signal from the pinger when excited with a continuous sine signal was simulated in the laboratory to estimate the

signal in sensors at large distances and compare it to the noise level in situ [123]. The used voltage signal was a 64 cycles sine wave at a fixed frequency (30, 45, or 60 kHz). The acoustic signal was sampled at 200 kHz and its power spectral density (PSD) was calculated. Then, the signal was convoluted with the transmit voltage response of the ITC-1001 (see §2.4.3) to determine the emitted PSD of it.

The acoustic signal was attenuated by r^{-2} and a frequency independent attenuation length of 300 m, as measured in situ by SPATS, to obtain the signal at 500 m distance to the emitter. Finally, the attenuated signal was convoluted with the sensor sensitivity, response function of the sensor, to obtain the sensor signal (Fig. 4.2(a)). This was compared to a typical noise level of $10^{-7} \text{ V}^2/\text{Hz}$, as shown in Fig. 4.2. For 30 kHz and 45 kHz the signal to noise ratio looks very good, but small for 60 kHz because of its small emitted amplitude. The amplitude decreases at higher frequencies due to the electrical properties of the ITC-1001. The recorded frequency differs from the nominal frequency due to the peaks in the sensitivity curve. This comes to an extreme for the very large peak at 65 kHz.

4.3 Data acquisition

The three channels of each sensor were recording data simultaneously at 200 kHz. The maximum duration for each channel was 18 s. The DAQ program which was used to record the data was looped continuously over the channels and sensors, in each string independently. A stop time of 5 minutes per level was established in order to guarantee that for every pinger stop all sensors at all levels had recorded the signal. The pinger repetition period was 0.6 s. Therefore the 18 s data sample has 30 waveforms of 0.6 sec duration. Each waveform consists of six pulses, two sets of 3 pulses in a (60,45,30) kHz cycle, see Fig. 4.3.

The pinger was triggered by the 5 Hz Garmin GPS, whose output was a rectangular pulse, 5 V amplitude, 100 ms low, 100 ms high state. The pinger was emitting pulses (i.e. 64 cycle sine wave) every 50 ms with a (60,45,30) kHz cycle when the trigger status is high. When the trigger went high, the first pulse was emitted followed by the second pulse after 50 ms before the trigger signal goes to low state again. The separation between two pulses is not exactly 50 ms, but 50 ms plus the duration of 64 cycles of the corresponding first sine wave. When the trigger status went high again, the third pulse was emitted and the same sequence was repeated till the end of the measuring time.

4.4 Systematic effects

Pinger data can be affected by many sources of uncertainties, called “systematic effect”. These effects include many known and sometimes unknown uncertainty sources due to the instrumentation. The best known sources are:

1. **Sensor sensitivity**

The sensitivity of the sensor modules exhibits a strong variation dependent not only

4.4. Systematic effects

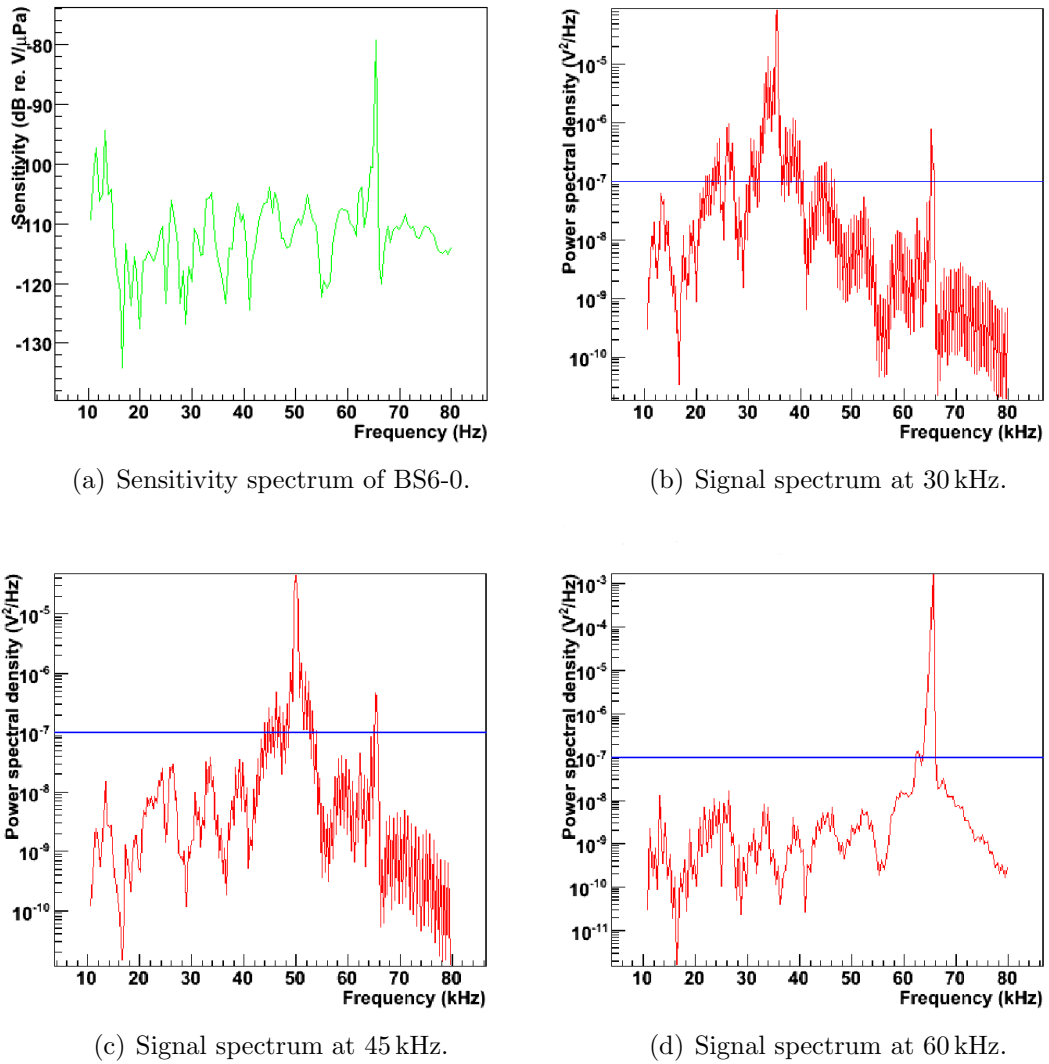


Figure 4.2: The attenuated acoustic signal, at different frequencies, at 500 m from the source is recorded using the sensor channel BS6-0. The recorded signal spectra are compared to a typical noise level of $10^{-7} V^2/Hz$ (blue line).

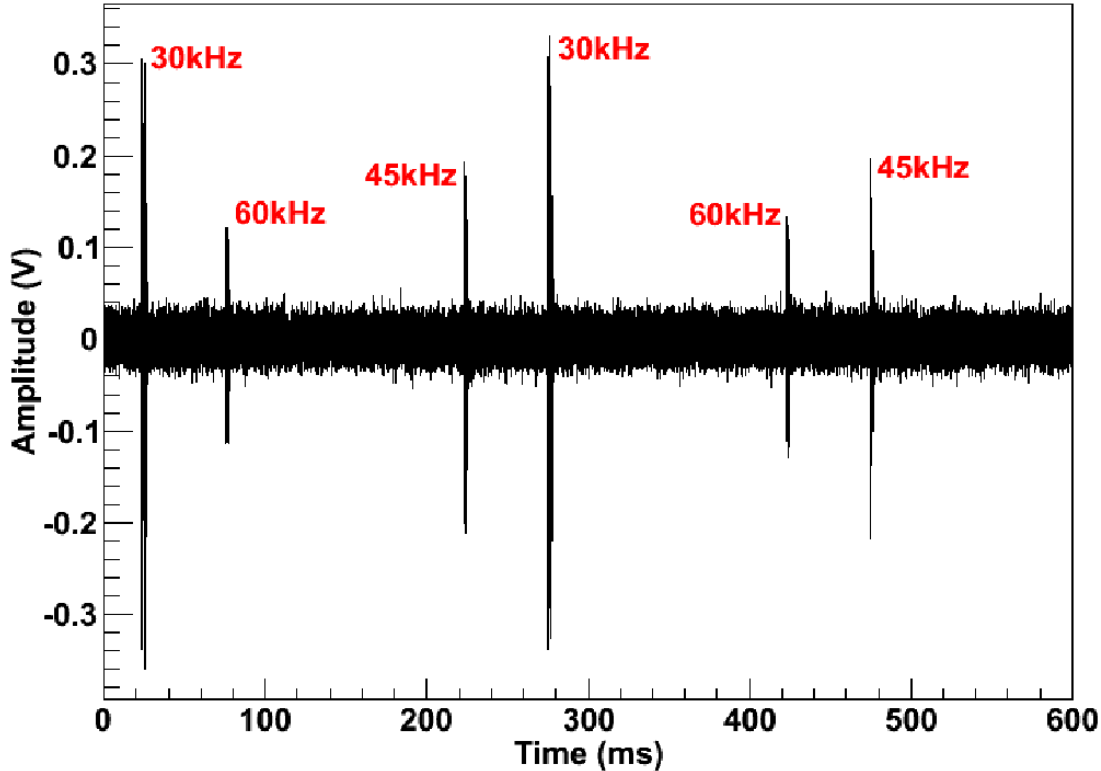


Figure 4.3: An example of a clockdrift corrected average waveform recorded by one channel of the sensor of String C installed at 320 m depth when the pinger was in Hole 25 at the same depth. The two sets of (60,45,30) kHz pulses are shown.

on the azimuthal but also on the polar angle.

- **Channel sensitivity variation:** Each SPATS sensor has three channels, and each channel is made of piezoelectric ceramics. The sensitivity of each channel depends on the d_{33} constant of the material and also on how each piezoelectric ceramic is pressed against the housing in the final mounting of the SPATS sensor [100]. Therefore each sensor channel has a different sensitivity spectrum. It is expected that waveforms recorded by different channels appear different, but waveforms recorded by the same channel should be similar in shape to each other. To perform an analysis independent of the sensitivity of the sensor channel, one should analyze the data recorded by the same channel from several pinger distances.
- **Azimuthal sensitivity variation:** The angular dependence of the sensitivity was measured in water for one SPATS sensor module over the full range of

azimuthal angles. The sensitivity variation was found on the order of 40% in water [100]. Measurements in South Pole ice indicate that the actual sensitivity varies up to 300% [103]. The pinger holes were chosen using the available IceCube holes which have a good alignment with SPATS strings. This will minimize the azimuthal variation of the SPATS sensors sensitivity.

- **Polar sensitivity variation:** The sensitivity of the sensor channel depends strongly on the polar angle. This effect was observed in pinger season 2007-2008 [103]. The polar sensitivity was found on order of 200% in water [100]. The variation of the polar angle between pinger and sensor plane can be minimized by selecting data from the same channel when the pinger is at the same depth as the sensor.
2. **Interference between transmitted and reflected waveforms:** When a sound wave propagates from water to ice, it is partially transmitted and partially reflected at the interface hole-wall, in all directions. The pressure wave which is directly transmitted from water to ice in the direction of the sensor interferes with the pressure wave which is first reflected by the back wall of the hole, and then transmitted in ice in the sensor direction, with a certain time delay compared to the one directly transmitted. The centralizer was used to force the pinger to stay near the hole center and prevented it from swinging. Therefore the interference between transmitted and reflected waveforms was forced to appear always about $500 \mu\text{s}$ after the beginning of the waveform. This also caused the shape of the waveforms, which were recorded by the same channel, to be very stable.
 3. **Hole ice**
 SPATS strings were deployed in IceCube holes filled with water that later refroze. The properties of the so called “hole-ice”, which surrounds the deployed strings, are not well known. It is assumed to have a higher concentration of bubbles and cracks than the bulk ice. These could lead to unknown and inhomogeneous absorption or scattering near the frozen sensors and to transmission inhomogeneities for the pinger signal.
 4. **IceCube cable position**
 SPATS strings were deployed with the IceCube cable in the same hole. The presence of the IceCube cable, which is about 10 cm thick, could shadow the SPATS sensor in the case of a specific location of the source. This could possibly increase the variation of the sensitivity with the azimuthal angle.
 5. **Dynamic range**
 Each sensor channel has a limited dynamic range due to the dynamic range of the differential amplifier. Output dynamic range is the range between the smallest and largest output voltage levels. The amplitude of the pinger signal must be chosen carefully to work within the sensor output dynamic range. If the signal is too

strong, the sensor output signal will be saturated and only limited information will be available in the waveform. On the other hand, if the source signal is too weak, the signal-to-noise ratio will be too poor at large distances. It is very difficult to predict which would be the signal power necessary for the pinger in order to have most of the sensors out of saturation but still capable to receive the signal. The effect of saturation, for small distances, makes a part of the collected data useless and excluded. For the attenuation length analysis, the saturation will lead to a flattened amplitude and that would lead to an overestimation of the attenuation length.

6. Noise

The recorded waveforms contain a contribution of both signal and noise. This noise is due to the sensor self-noise, the cable, the acoustic junction box electronic devices and the acoustic noise in the ice. To get the contribution from the real signal, the noise must be correctly subtracted. If the noise is not subtracted, the real signal will be embedded in the noise as shown in Fig. 4.5(b).

7. Clock drift

The clock drift effect can be corrected on the sensor side as summarized in §4.5.1. The accuracy in time of the pulses emitted from the pinger was measured in the laboratory to be approximately $10\ \mu\text{s}$ over the recording time for a single channel. The drift on the pinger side cannot be corrected, and contributes to the statistical uncertainty.

All these effects are taken into account during the analysis steps to reduce the uncertainty due to systematic effects. For the attenuation length analysis, if the data used are selected from one single channel for several pinger distances in the same direction, any local effects should be negligible.

4.5 Data processing

Data samples which were recorded by each sensor for 18 s were processed to achieve good signal-to-noise ratio with the following steps:

4.5.1 Clock-drift correction

Each SPATS string has a string-PC which uses a single clock to drive its analog-to-digital converters (ADCs). These ADCs were used to digitize the sensor waveforms and were discovered to drift over time. “Drift” means that the true sampling frequency is slightly different from the requested, or nominal, sampling frequency. The sampling frequency slightly varies with time in a non-linear way. The clock drift is typically on the order of a few parts per million. So, the nominal time increases or decreases by a few microseconds per second relative to the absolute time. Over time, the cumulative amount of drift can

4.5. Data processing

cause a strong de-coherence in the waveform averaging if the nominal rather than true sampling frequency is used. The “drift rate” was defined as:

$$\text{drift rate} = \frac{\text{actual sampling frequency}}{\text{nominal sampling frequency}} - 1 \quad (4.2)$$

The clock drift problem was properly corrected using the GPS IRIG-B signal, which is sampled synchronously with every sample of every waveform, to determine the absolute time of each sample directly. The IRIG-B signal has 100 rising edges per second, see Fig. 4.4. The time as given by the IRIG-B signal is assumed to be the true time and the rising edges to be exactly 0.01 s apart. The IRIG-B waveforms are sampled at 200 kHz, therefore the nominal bin width is $5 \cdot 10^{-6}$ s. The true bin width can then be obtained by plotting the true elapsed time since the first rising edge as a function of the bin number, see Fig. 4.5(a). The true bin width is then used to determine the absolute time of each sample, since the waveform acquisition began, as a function of its sample number.

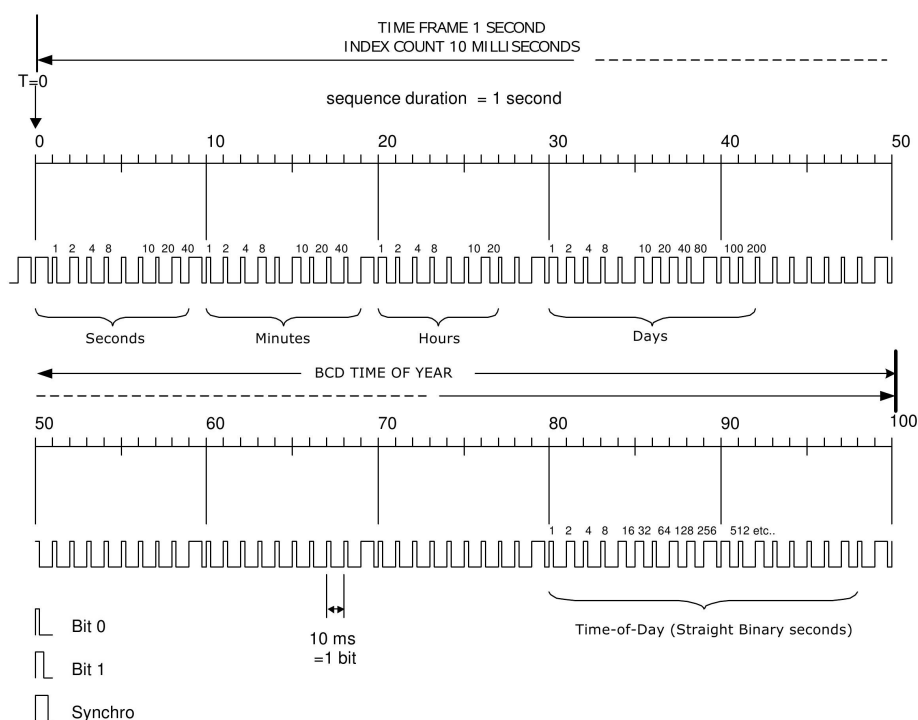


Figure 4.4: The IRIG-B 100 pps timing signal. In 1 second of data, there are 100 rising edges separated by 0.01 s. The start of the sequence is indicated by two 8 ms high separated by 2 ms low, the start of the GPS second is aligned with the second rising edge.

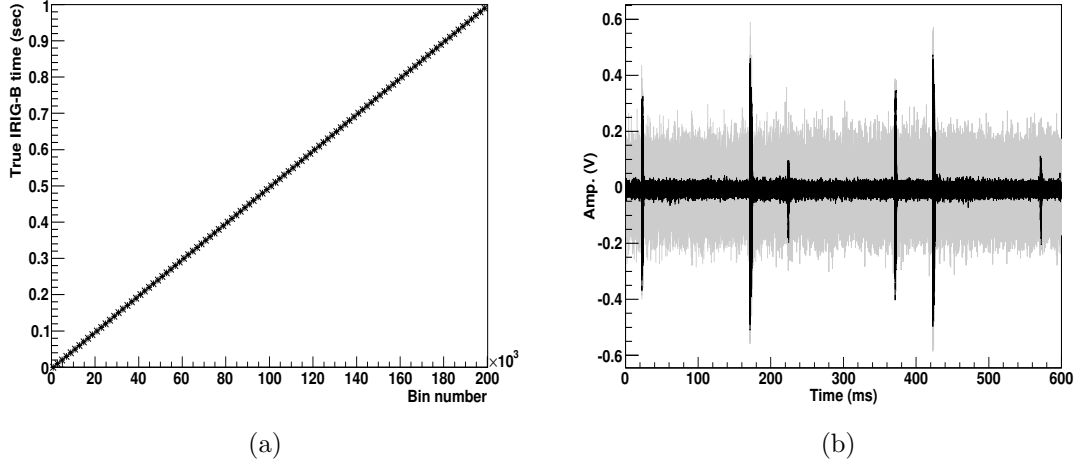


Figure 4.5: (a) True IRIG-B time since first rising edge as a function of number of bins since first rising edge for the first second of IRIG-B data. (b) An example of 0.6 s waveform before and after averaging for BS6-0 waveform.

4.5.2 Averaging

To improve the signal-to-noise ratio for the clockdrift-corrected samples, the recorded waveform is averaged. The noise level will then be reduced by a factor $1/\sqrt{N}$, where N is the number of averaged waveforms, see Fig. 4.5(b). Each 0.6 sec waveform, the repetition period for the pinger, contains N_{bins} bins according to the true sampling frequency for each run. The averaging was done by folding each waveform to the pinger repetition period of 0.6 s, this means re-binning the recorded samples in bunches of N_{bins} . The mean value of the amplitude and its corresponding standard error were computed for the samples in each bin. To get high quality pulses (good signal-to-noise ratio) for each channel-hole combination, the above procedures were applied to all files in the data set illustrated in § 4.7.1.

4.6 Data Quality: expected signal

The recorded data looks very stable and consistent from hole to hole. Fig. 4.6 shows a comparison between waveforms when the pinger was at the same depth for different holes. Each plot shows the two waveforms recorded when the pinger was on the way down and on the way up. The three plots show the waveforms recorded by the same channel. It is clear that the waveforms all look very similar not only for repeated stops in one hole, but also for stops in different holes. This stability is because of the centralizer which is used to prevent swinging and force the sound source (pinger) to stay near to the hole center and it also allows the time delay between transmitted and reflected waves to be always about $500 \mu s$. This also minimized the appearance of shear waves. It should be noticed that at

large distances shear waves will disappear due to a shorter attenuation length than that of longitudinal waves.

4.7 Attenuation analysis

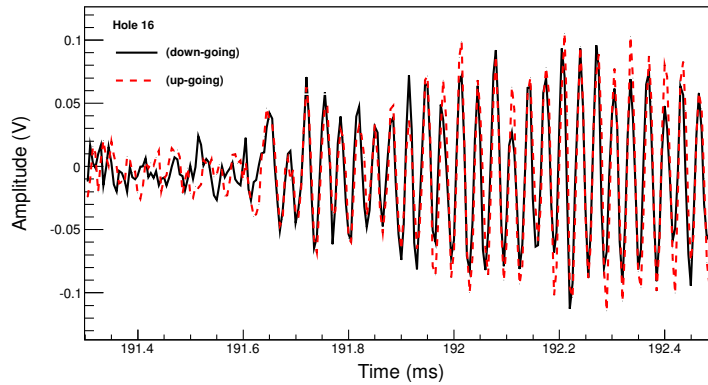
4.7.1 Data set selection

Acoustic pulses were emitted from the pinger and recorded by sensors of the SPATS array, see section §4.3. All data used for analysis have been processed as explained in section §4.5 to get high quality pulses (good signal-to-noise ratio) for each channel-hole combination. To perform an attenuation analysis with the smallest influence of systematic effects it is necessary to reduce the effect of known sources which give a systematic error:

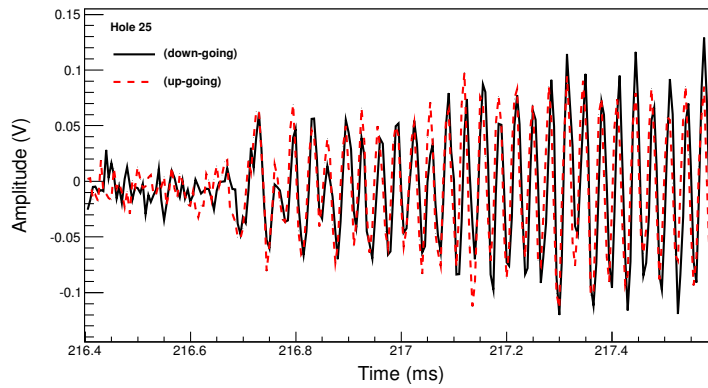
- Sensor sensitivity: selecting data recorded by each sensor channel for several pinger distances enables us to compare them. In addition, we can neglect the sensor response function, unknown in our case, assuming the following:
 - The sensor response is constant throughout the pinger data taking. This is supported by the fact that the noise spectra measured by the sensors has been demonstrated to be very stable in time.
 - The sensor output is linear in amplitude with respect to the input amplitude. This has been demonstrated in the laboratory for signals which are within the range of amplitudes considered here.
- Polar variation: selecting data recorded by each channel, when the pinger was at the same depth as the sensor, will minimize the influence of polar variation of the sensor sensitivity. The polar angle depends on the horizontal distance between the pinger hole and the string. It changes from 0.35° at 819.7 m to 1.6° at 177.9 m.
- Azimuthal variation: selecting data recorded with the pinger at multiple distances aligned in the same direction with respect to the sensor location will minimize the influence of azimuthal variation of the sensor sensitivity. The azimuthal variation depends on the positions of the pinger holes. The maximum azimuthal spread of the measurements for each string is shown in Table 4.4.

<i>String-A</i>	<i>String-B</i>	<i>String-C</i>	<i>String-D</i>
9°	6°	19°	20°

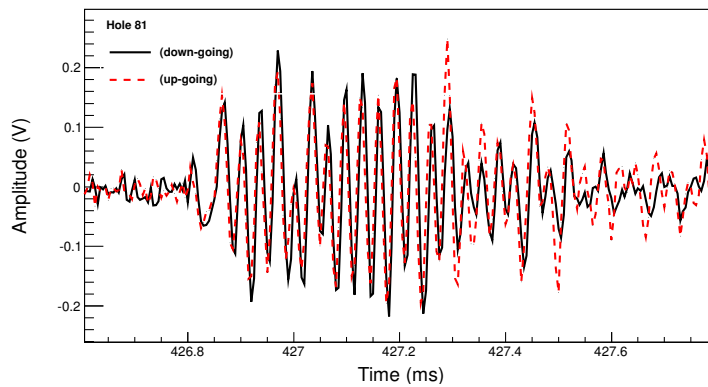
Table 4.4: Azimuthal spread of the pinger holes. The maximum difference of the azimuth angle between the 3 pinger holes for each SPATS string is shown.



(a)



(b)



(c)

Figure 4.6: Waveforms recorded by the same channel (sensor D3 and channel 0) for three different pinger holes (16,25,81) when the pinger was stopped on the way down and on the way up at the same depth of the sensor. The up-going red-dashed waveform has been artificially shifted to compare with the down-going black-solid waveform.

- Constant pinger emission: the pinger emission is assumed to be constant throughout all the measurements. This is reasonable since the chosen piezoelectric ceramic is specified to work down to 1250 m depth.

Generally, only data recorded at the same pinger depth are combined. Therefore any eventual variation of the pinger spectral emission with depth, due to dispersion, should not influence the attenuation analysis. Also, non-saturated waveforms were used for analysis while the saturated waveforms were excluded.

4.7.2 Fitting

The recorded signal amplitude A is proportional to the acoustic pressure incident on the sensor. For a point source (like the pinger) with spherical emission, the signal amplitude scales due to the distance to the source as $1/d$ and the amount of attenuation by the ice $e^{-d/\lambda}$ as:

$$A(d) = \frac{A_0}{d} e^{-\alpha d} = \frac{A_0}{d} e^{-d/\lambda} \quad (4.3)$$

This equation can be turned into a linear equation:

$$y = \ln(Ad) = -\alpha d + \ln(A_0). \quad (4.4)$$

A linear fit can be performed using the model:

$$y = -\alpha d + b \quad (4.5)$$

where:

- A is the amplitude (in V) proportional to the pressure amplitude recorded by the sensor.
- A_0 is a characteristic constant which defines the sound at the source. Sometimes it is taken to be the amplitude of the acoustic pressure at 1 m from the source.
- d is the pinger to sensor distance (in m).
- α is the acoustic attenuation coefficient (in m^{-1}).
- $\lambda = 1/\alpha$ is the attenuation length (in m).
- b is a free normalization parameter related to the sensor sensitivity.

A fit to the data then directly determines the two parameters, α and b , and their respective errors. The error on the variable y is:

$$\sigma_y = \sqrt{\left(\frac{\sigma_A}{A}\right)^2 + \left(\frac{\sigma_d}{d}\right)^2 + (\sigma_{\text{sys}})^2} \quad (4.6)$$

where:

- σ_{sys} is the systematic uncertainty, estimated in § 4.7.4.
- $\frac{\sigma_A}{A}$ represents the statistical uncertainty of the amplitude. This is calculated by error propagation of the statistical uncertainty of each sample of the mean waveform.
- $\frac{\sigma_d}{d}$ represents the uncertainty of the pinger to string location and can be expressed as:

$$d = \sqrt{d_H^2 + \Delta_z^2} \quad (4.7)$$

$$\sigma_d = \frac{\sqrt{(d_H \sigma_{dH})^2 + (\Delta_z \sigma_{\Delta z})^2}}{d} \quad (4.8)$$

where:

- d_H is the horizontal distance between the string and the IceCube hole where the pinger was deployed;
- σ_{dH} is the error on the horizontal distance, which is estimated to be of the order of $\sqrt{2}/2$ [m];
- Δ_z is the difference in depth between pinger and sensor (less than 5 m);
- $\sigma_{\Delta z}$ is the error on the real pinger depth (assumed 5 m in the worst case).

4.7.3 Attenuation frequency dependence

The frequency dependent study for the attenuation length is done using multi-frequency pinger data. Each recorded waveform x consists of the real signal s , emitted from the pinger, and the background noise n which is uncorrelated with the signal. Therefore, the the amplitude x of a sample i at time t_i is given by:

$$x(t_i) = s(t_i) + n(t_i) \quad (4.9)$$

The noise of each waveform N was estimated from the off-pulse portion of the waveform (following the methods described in [124, 125, 126]). To avoid any overlap with the signal, the noise interval is taken before the observed pulse. The power spectral density (PSD) is calculated for signal and noise [127], see Appendix A. Examples of a raw signal-plus-noise spectrum, a pure noise spectrum and a signal spectrum are shown in Fig. 4.7.

As can be seen from Fig. 4.7(c), the spectral shape is approximately constant for the same sensor, but attenuated with increasing distance, i.e. for different pinger hole measurements. The peak at 10 kHz reflects a characteristic peak in the sensor response.

The signal spectrum density S_m at each sample m after subtracting the noise density N_m from the raw signal-plus-noise density X_m is given by:

$$|S_m|^2 = |X_m|^2 - |N_m|^2 \quad (4.10)$$

4.7. Attenuation analysis

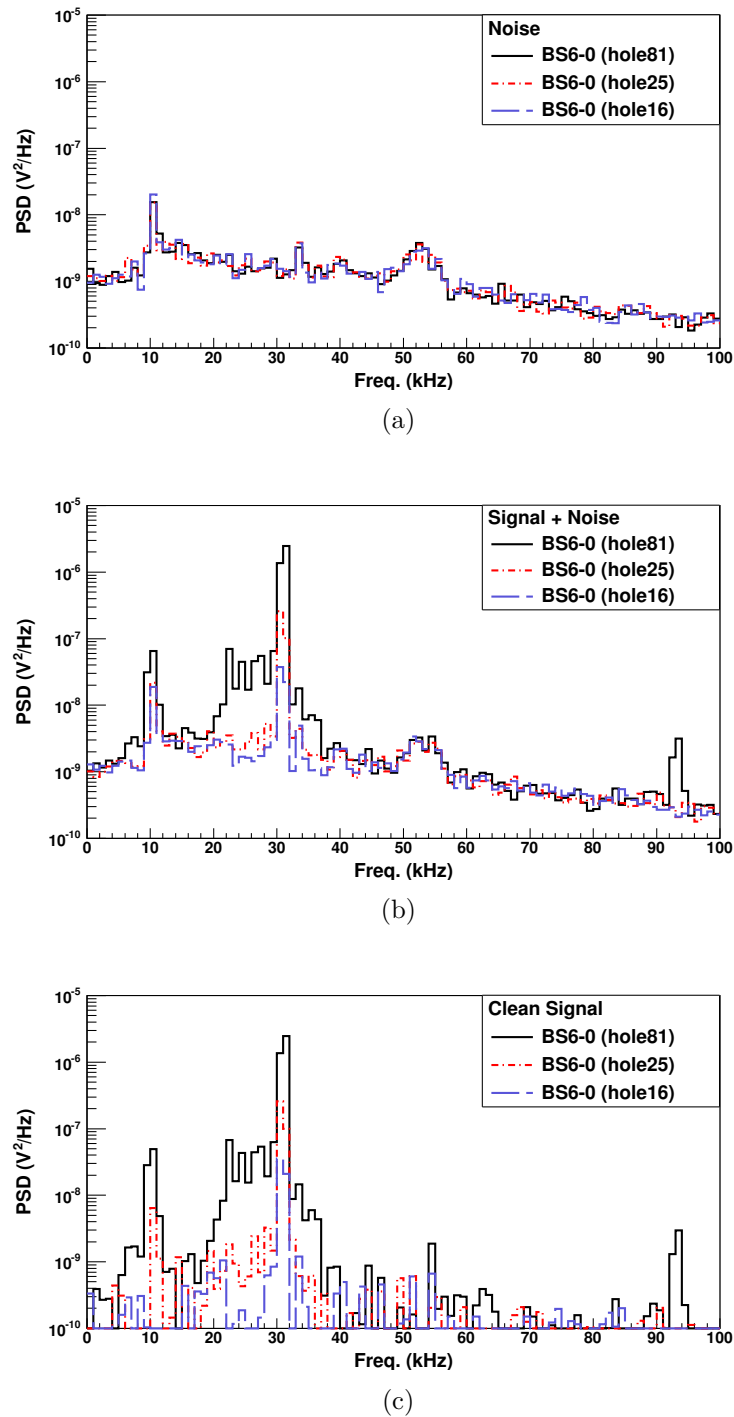


Figure 4.7: (a) Raw signal with noise, (b) noise and (c) noise-subtracted signal spectra, from different holes, recorded by the same sensor channel (BS6-0) when the pinger stopped at the same depth of the sensor.

then the effective amplitude A_{eff} can be calculated by:

$$A_{eff} = \sqrt{E} = \sqrt{\sum_m |S_m|^2} \quad (4.11)$$

where S_m are the coefficients of the noise-subtracted Fourier spectrum at each sample m and E is the waveform energy in the frequency domain. The response function of the sensors is implicitly included in A_0 which is independent of d . Therefore, the amplitude attenuation coefficient can be extracted from Eq. 4.5 using $A = A_{eff}$.

Generally, a simple cut is applied to select values with positive energy $E \geq 0$. Since the distances between sensor and pinger are known and the effective amplitudes are defined, the values of the y variable of Eq. 4.5 can be calculated. The overall uncertainty on the y variable is estimated as in Eq. 4.6. The statistical uncertainty of the effective amplitude is determined with standard error propagation:

$$\sigma_A = \frac{\sigma_E}{2\sqrt{E}} \quad (4.12)$$

which leads to:

$$\frac{\sigma_A}{A} = \frac{\sigma_E}{2E} \quad (4.13)$$

4.7.4 Attenuation results

To study the frequency dependence of the attenuation length, or attenuation coefficient, waveforms with good signal-to-noise ratio are selected. The selected waveforms are recorded by the sensor channel when the pinger was stopped at the same sensor depth in the three holes. The attenuation depends on the local properties of the ice at the measurement location. The same-level choice gives the same ice structure and minimizes any unknown systematic uncertainties. Once the waveforms are processed as explained in section § 4.5, their power spectra are calculated using the FFT transformation and the error bars are propagated by Gaussian error propagation. Each noise spectrum is subtracted from the spectrum of each waveform in order to get the noise-subtracted signal spectrum. The waveform power spectra are binned in 1 kHz bin widths. To get the waveform energy E at each frequency, the sum over the Fourier spectra is performed at the three studied frequencies by using a band width of 2 kHz. From the energy an effective amplitude A_{eff} is calculated, at each frequency, using Eq. 4.11. To calculate the attenuation coefficient α from Eq. 4.4, we should have three waveforms recorded by the same sensor channel from the three different holes. This will give a good linear fit to the data points. The slope of the linear fit yields the attenuation coefficient, whereas the intercept depends on the channel sensitivity.

- **Systematic error**

To calculate the uncertainty on Eq. 4.4, the systematic error should be estimated. To estimate the systematic uncertainty, we assume different systematic error values

in addition to the statistical error in Eq. 4.6 and check the fit quality. At least three data points (one from each hole) are required, so that the number of degrees of freedom of the fit is at least 1. This requirement is fulfilled by all selected channels. To test the fit quality, the linear regression using Eq. 4.4 for the data points from each channel is performed. The reduced chi-square χ^2/ndf values from assumed systematic values and all available channels are shown in Fig. 4.8. The systematic error value of 20%, which gives a mean value of the $\chi^2/ndf \simeq 1.5$, is used. This intermediate value of the systematic uncertainty does not affect significantly the final result, while the higher values will shift χ^2/ndf below 1 and the error becomes overestimated.

Fig 4.9 shows an example of the fit on the data points, using a systematic uncertainty of 20%, to obtain the attenuation coefficient for different frequencies recorded by the sensor channel BS5-1. All the fits for all the channels at 30 kHz and 45 kHz are presented in Appendix B. For each distance there are three data-points, corresponding to different measurements. The fit is obtained with the MINUIT numerical minimisation package [128] as it is implemented in ROOT [129].

- **Attenuation coefficient**

Since the emitted amplitude from the pinger decreases with increasing frequency, the sensor signal at 60 kHz is not above the noise as for the 30 kHz and 45 kHz signal, see section § 4.2. The contribution of 60 kHz signals is not strong enough at large distances to calculate the attenuation length. There are not enough waveforms at 60 kHz with good signal-to-noise ratio. The attenuation coefficient for all available channels at 30 kHz and 45 kHz are plotted in Fig 4.10 and Fig 4.11, respectively. The data points scatter more than their error bars indicate, implying that there are additional systematic uncertainties, e.g. arising from local ice properties or the interface between the hole ice and the sensors or other systematic uncertainties which we are not able to identify. The error represents the spread between attenuation lengths measured with each sensor. To get the mean attenuation coefficient and its error, the weighted mean and its corresponding standard deviation are calculated for the attenuation coefficient values for each plot. Finally, the mean attenuation coefficient and its error are calculated as:

$$\langle \alpha \rangle_{30 \text{ kHz}} = 3.77 \pm 0.39 \text{ km}^{-1} \quad (4.14)$$

$$\langle \alpha \rangle_{45 \text{ kHz}} = 3.35 \pm 0.76 \text{ km}^{-1} \quad (4.15)$$

which expressed as an attenuation length as:

$$\langle \lambda \rangle_{30 \text{ kHz}} = 265_{-25}^{+30} \text{ m} \quad (4.16)$$

$$\langle \lambda \rangle_{45 \text{ kHz}} = 299_{-55}^{+87} \text{ m} \quad (4.17)$$

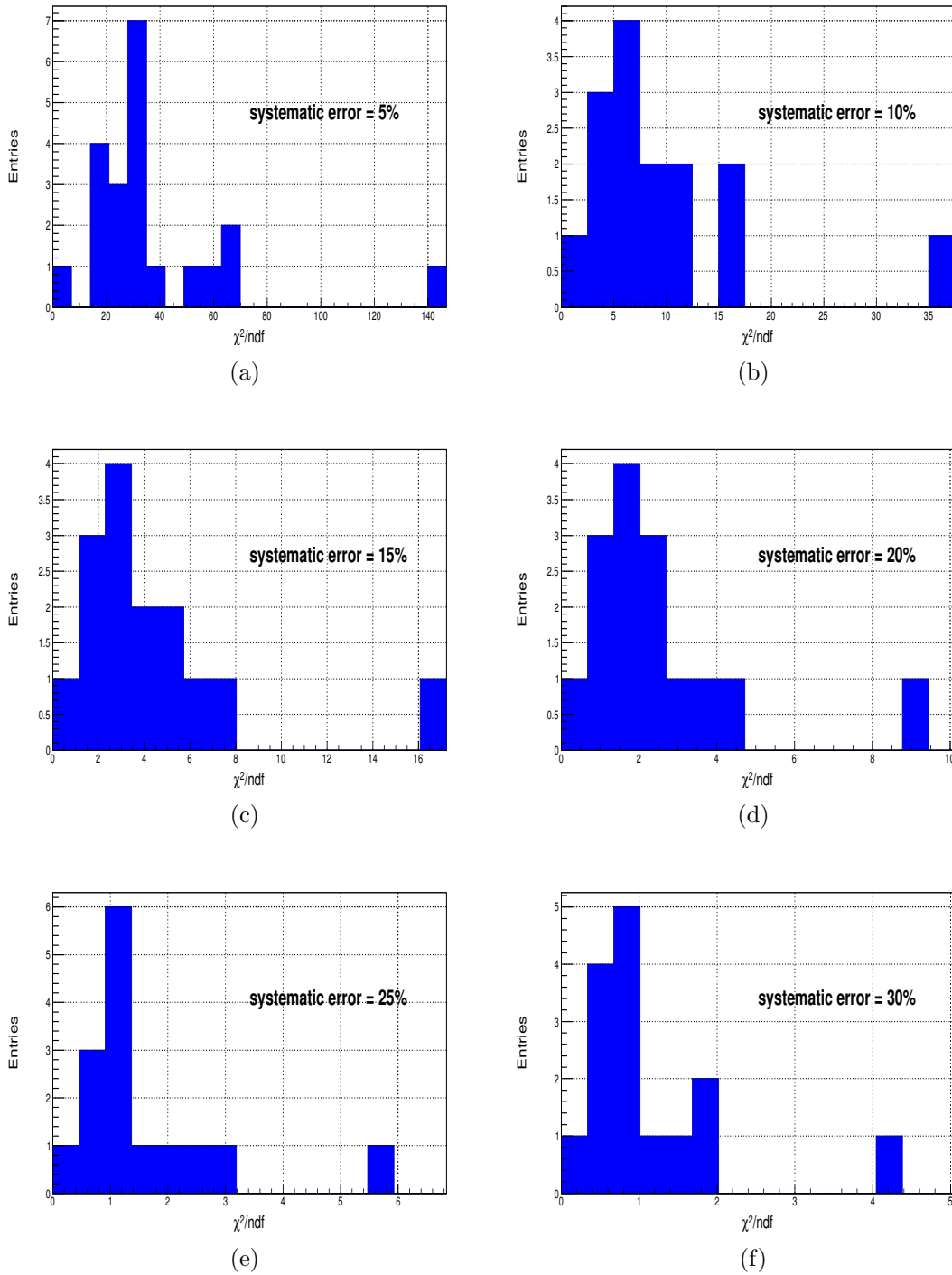


Figure 4.8: The distribution of the reduced chi-square χ^2/ndf of all fits for all channels.

4.7. Attenuation analysis

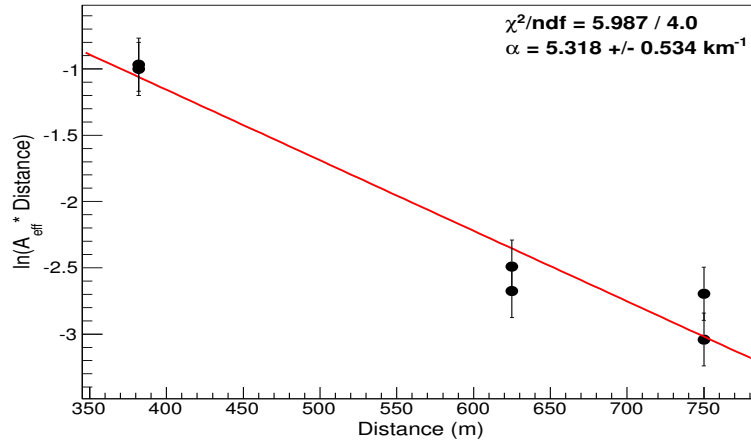


Figure 4.9: The effective amplitude A_{eff} with distance vs. distance from different pinger holes recorded by sensor BS5-1 at frequency 30 kHz. The linear fit yields the attenuation coefficient.

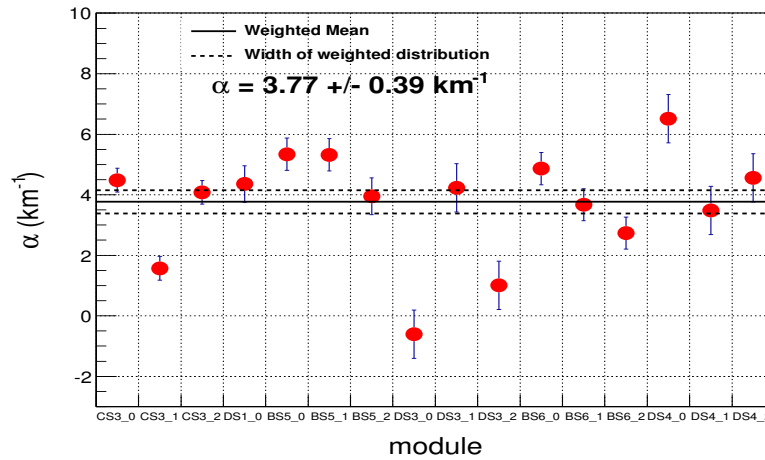


Figure 4.10: α and corresponding error at 30 kHz for each channel. The horizontal lines denote the weighted mean (solid line) and the standard deviation (dashed lines) over all channels.

- **Attenuation depth dependence**

To investigate the depth dependence of the attenuation, α at each available depth are plotted versus depth. Each data point represents α and corresponding error for different channels, see Fig 4.12. The weighted mean and corresponding error of α at each depth are calculated to get the main value and its error as shown in Fig 4.13. From the slope, α does not show a significant depth dependence between 140 m and

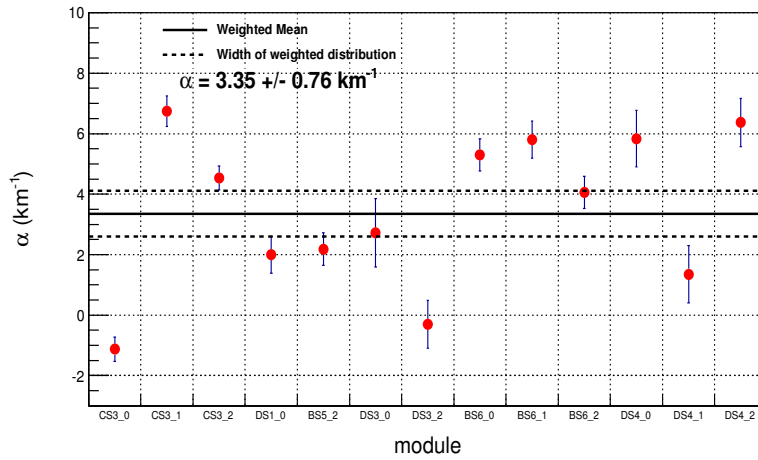


Figure 4.11: Attenuation coefficient and corresponding error at 45 kHz for each channel. The horizontal lines denote the weighted mean (solid line) and the standard deviation (dashed lines) over all channels.

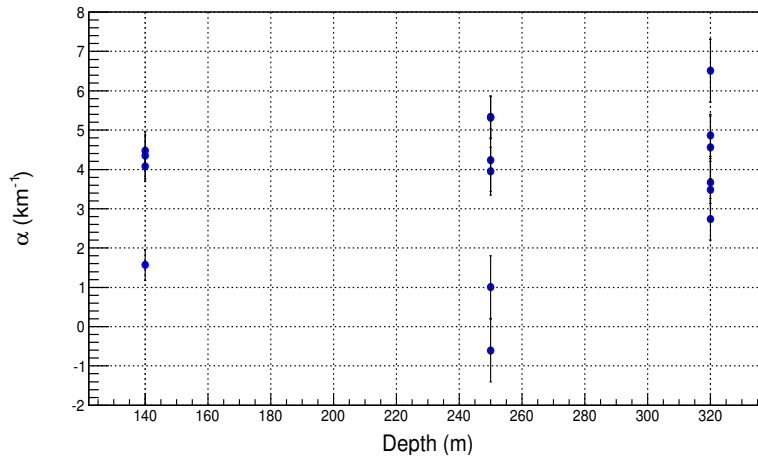


Figure 4.12: Attenuation coefficients vs. depth for 30 kHz signals.

320 m.

- **Attenuation mechanism**

α is measured at different frequencies to distinguish between the two different attenuation mechanisms: the absorption coefficient which is frequency independent, while the scattering coefficient is expected to increase with f^4 . Fig 4.14 shows the expected scattering coefficient due to the grain boundaries as a function of frequency and grain diameter in South Pole ice [4], while the measured α at 30 kHz and

4.7. Attenuation analysis

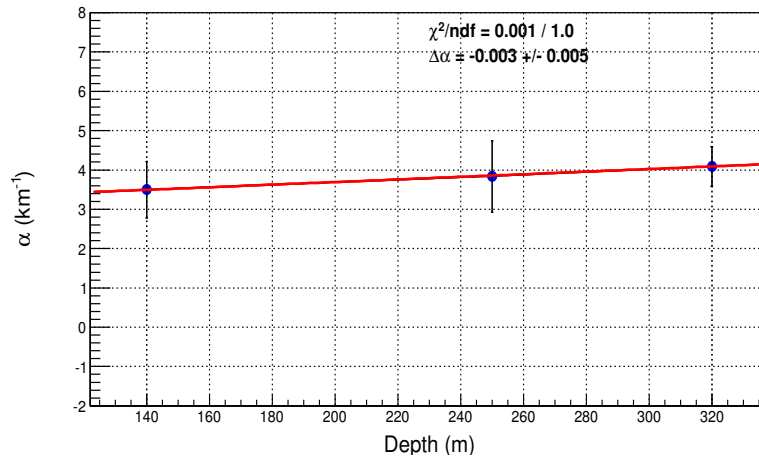


Figure 4.13: The weighted mean and corresponding error for attenuation coefficients vs. depth for 30 kHz signals.

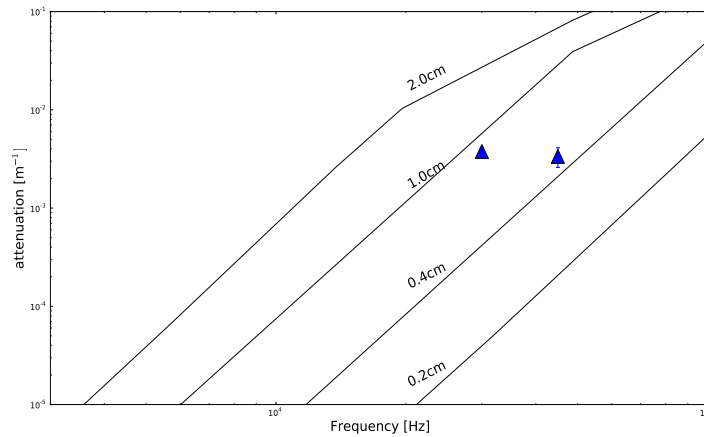


Figure 4.14: Contribution to scattering due to grain boundaries as a function of frequency and grain diameter in South Pole ice, adapted from [4]. The two measured values are shown for comparison.

45 kHz are shown for comparison. The measured α is frequency independent within the measured frequency range. Therefore, the attenuation is due to the absorption within the studied frequency range.

According to the model described in [4], the measured α corresponds to an ice temperature of -20° while it is nominally -50° . Therefore, we conclude that this model does not fit with the measured α .

4.8 Sound speed measurements

The sound speed was measured with a better than 1% precision for both pressure and shear waves as a function of depth between 80 m and 500 m depth in South Pole ice [104]. These measurements were done using 2007/2008 pinger data. The pinger used for that analysis emitted acoustic power strongly peaked in the 5 kHz to 35 kHz frequency band. The data from 2009/2010 pinger season are used now to study the sound speed frequency dependency and the South Pole ice fabric (e.g. the grain orientation as a function of position in a glacier). The procedures for both the same level and diagonal sound speed measurements using the multi-frequency pinger data will be presented.

1. **Run selection:** All data used for sound speed analysis have been processed as explained in section §4.5. Waveforms which have a good signal-to-noise ratio for the three studied frequencies were selected.
2. **Propagation time:** The start time for 30, 45, and 60 kHz pulses was extracted, see Fig. 4.15, using the following procedure:
 - zoom in each pulse in the same waveform.
 - apply a bipolar discriminator using a manually chosen threshold according to the noise level which is varying from channel to channel.
 - the pulse arrival time $T_{arrival}$ was estimated as the first threshold crossing above the noise.
 - the pulse start time T_{start} is the time since the start of GPS second T_{GPS} ;

$$T_{start} = T_{arrival} - T_{GPS} \quad (4.18)$$

this equation works for the first pulse after the start of the trigger, but the 64 cycle duration of the first pulse should be subtracted from the T_{start} of the second pulse and 150 ms in case of the third pulse, see §4.3.

The uncertainty on this arrival time determination is estimated to be ± 0.05 ms, corresponding to 1 signal oscillation period.

3. **Fitting procedure:** The relation between the pulse arrival time and its speed is given by:

$$T_{start} = \frac{d}{v} + T_{delay} \quad (4.19)$$

where:

- d is the distance between the pinger and the sensor.
- v is the sound speed.

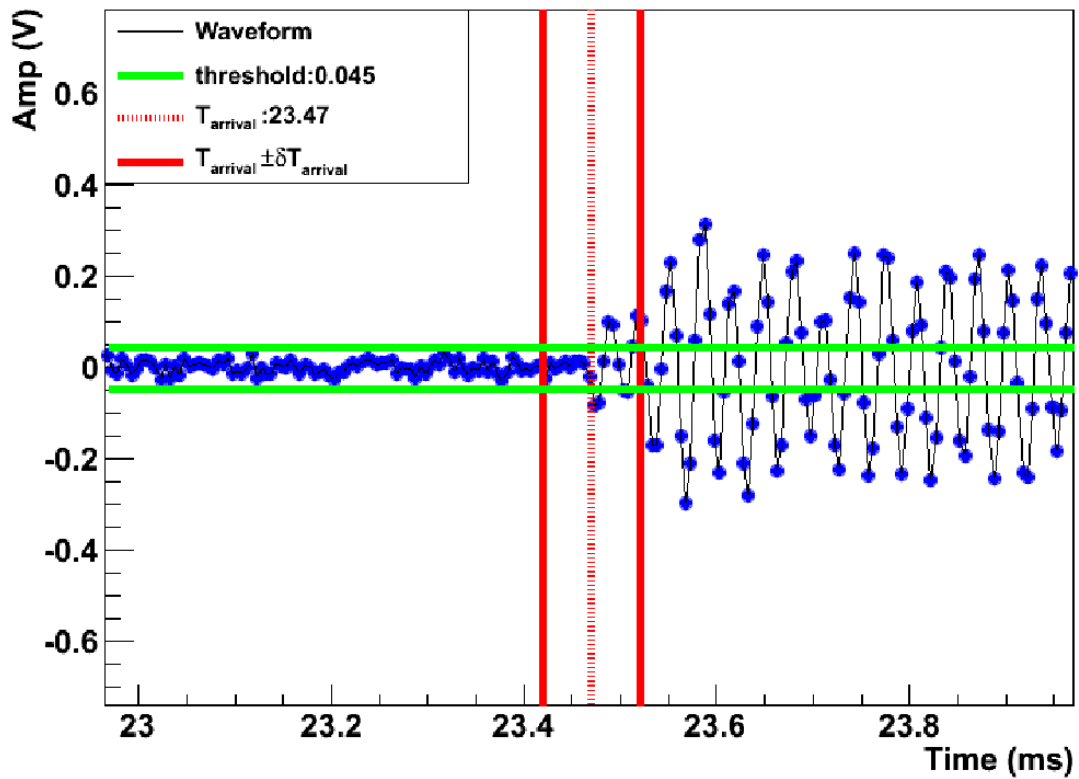


Figure 4.15: Zoom on for the beginning of a 30 kHz pulse recorded by sensor channel CS6-1 when the pinger was in hole 25. The pinger and the sensor were at the same depth (320 m). The threshold used to determine the signal start time is shown, as are the signal start time and uncertainty of the arrival time.

- T_{delay} is the delay due to the cables and electronics. The emission time delay introduced by the HV pulser was measured in the laboratory to be $21.2 \mu\text{s}$ [123], and the delay due to the RW cable is $10 \mu\text{s}$ which give a total delay of $31.2 \mu\text{s}$.

If we plot the pulse arrival time versus the distance between one sensor channel and different pinger holes, the sound speed v can be extracted from the linear fit. This method minimizes the effect of any time delay introduced by cables or electronic boards. Applying this method at different frequencies will show if the sound speed has any frequency dependency.

4.8.1 Frequency dependent results

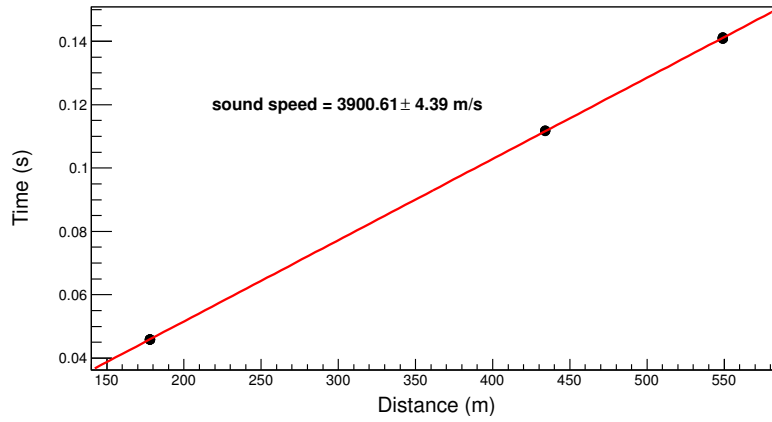
The sound speed can vary due to differences in bubble concentration, temperature, and grain orientation. To perform the sound speed frequency study, the data recorded when the pinger is at the same depth as the sensor is selected to have the same ice structure. Therefore, the sound speed does not have any effect due to the ice structure. Data recorded at two depths (250 and 320 m) are used for this study with string C (the nearest string to the pinger holes) which gives waveforms with good signal-to-noise ratio at the three studied frequencies. At a depth of 250 m, the waveforms were recorded by sensor CS5 channels, while they were recorded by sensor CS6 at a depth of 320 m. The propagation time for the pressure pulses is calculated while the pinger was at different pinger holes, using eq. 4.19 and as explained in Fig. 4.15, for the three sensor channels. The pinger depths from the payout measurements are used with maximum uncertainty of 1 m, while the estimated uncertainty is less than 1 m. The distance d between the pinger and sensor and its uncertainty are calculated using Eqs. 4.8.

Fig. 4.16 and Fig. 4.17 show the acoustic pulses propagation time versus the horizontal distance between each pinger hole and sensor hole at depths of 250 m and 320 m, respectively. Each distance has at least 3 data points from each sensor module, they are coincide to each other within the point size. This calculation is done for the three studied frequencies as shown. The sound speed v and its uncertainty are extracted from the linear fit for the three studied frequencies. The calculated sound speed versus frequency is shown in Fig. 4.18 and summarized in Table 4.5. The measured sound speed is consistent within less than 0.2% uncertainty at the studied frequency range (30,45,60 kHz). Therefore, one can say that that there is no indication for a frequency dependence of the sound speed in the South Pole ice within the studied frequency range.

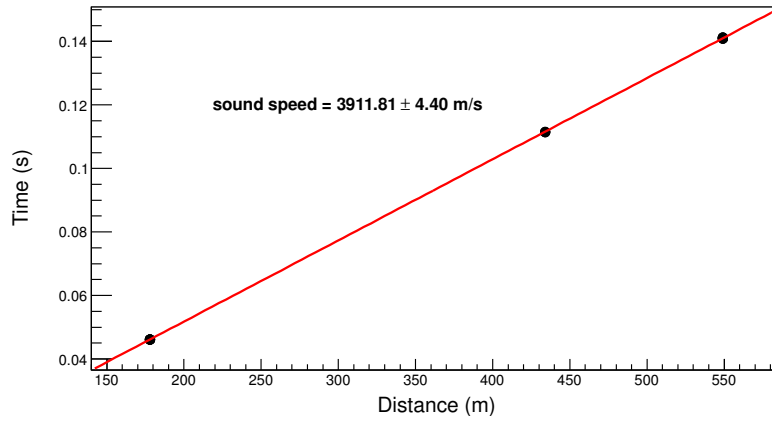
	30 kHz	45 kHz	60 kHz
250 m	3900.61 ± 4.39	3911.81 ± 4.40	3904.08 ± 5.56
320 m	3913.36 ± 5.63	3915.83 ± 5.63	3913.22 ± 5.63

Table 4.5: Measured sound speed and its uncertainty, in ms^{-1} , while the pinger and the sensor were at the same level (250 m and 320 m) for different frequencies.

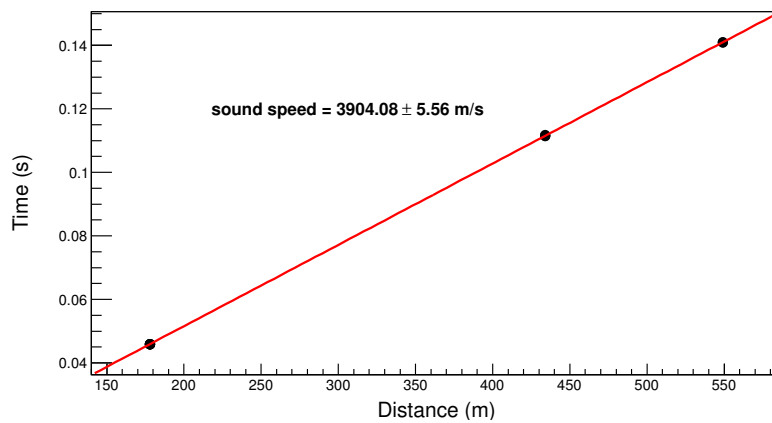
4.8. Sound speed measurements



(a)

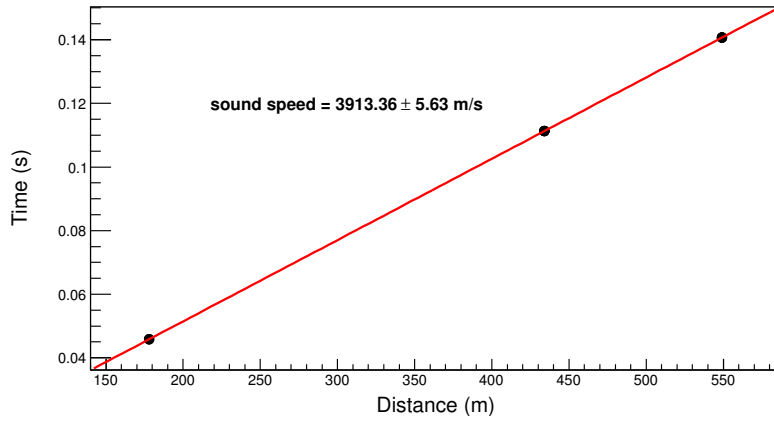


(b)

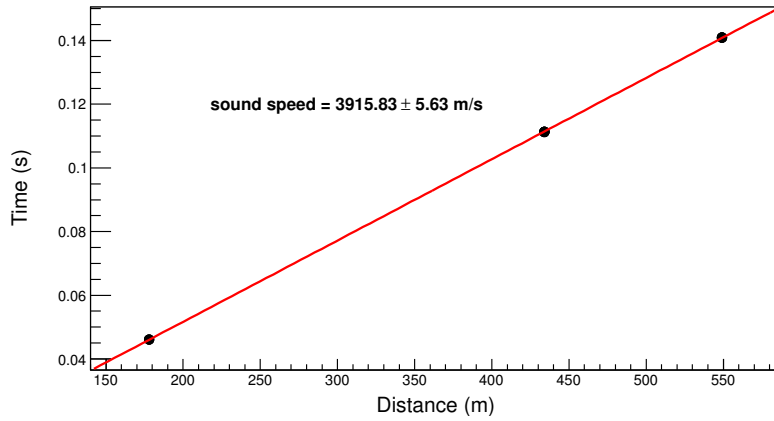


(c)

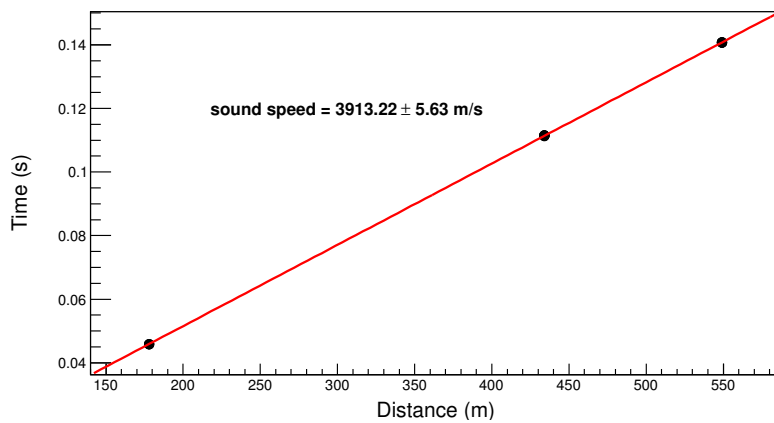
Figure 4.16: Propagation time versus distance, at depth 250 m, for different CS5 sensor channels at (a) 30 kHz, (b) 45 kHz and (c) 60 kHz.



(a)



(b)



(c)

Figure 4.17: Propagation time versus distance, at depth 320 m, for different CS6 sensor channels at (a) 30 kHz, (b) 45 kHz and (c) 60 kHz.

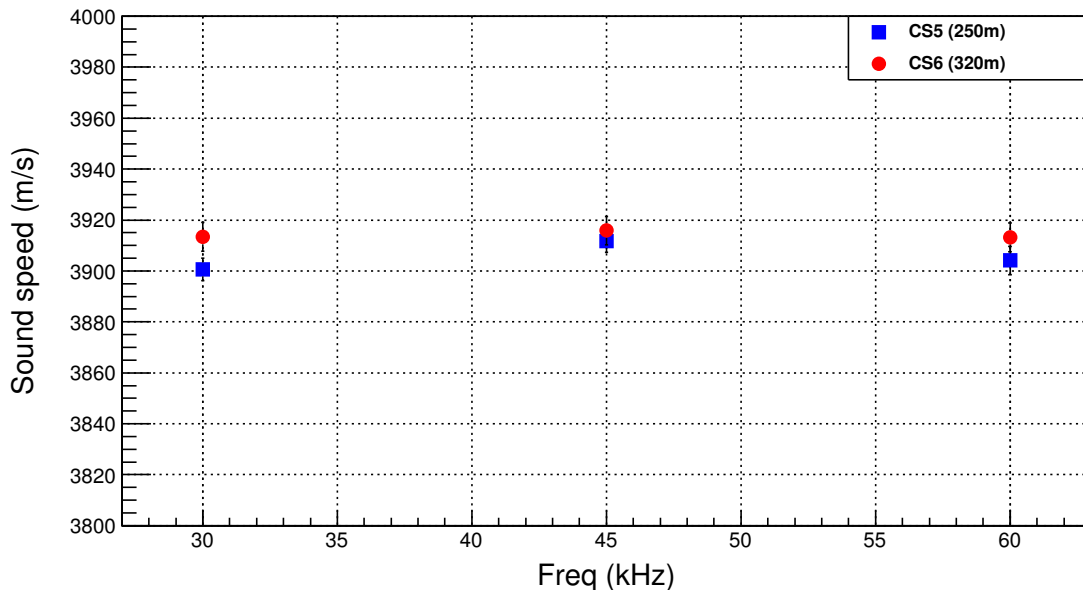


Figure 4.18: Sound speed while the pinger and the sensor were at the same level, 250 m and 320 m, for different frequencies. The error bars are $\pm 1 \sigma$.

Fig. 4.19 shows the measured sound speed, at frequency 30 kHz, and the previous measurements from 2007/2008 season. The two measurements are consistent with each other with an accuracy better than 1%. Both measurements show no depth dependence in the bulk ice (deeper than 200 m). The previous measurements were done for deep ice (500 m) and found that the sound speed gradient is consistent with zero for both pressure and shear waves [104]. Thus, deep ice is considered as a good medium to build an acoustic detector where the acoustic waves will propagate without any refraction [3]. Therefore the location of an acoustic source can be reconstructed precisely using analytical methods.

4.8.2 Ice fabric results

The ice fabric refers to the direction of the c-axes of an assemblage of ice crystals. The distribution of crystal axes indicates how random or concentrated the fabric is, or how the axes are distributed about the vertical axis. The c-axis fabric of an ice sample refers to the distribution of crystal axes. Ice crystals are anisotropic with regard to the acoustic waves, so acoustic waves propagating through the ice can determine the direction of the c-axis. Both sonic and seismic techniques were used to characterize the ice fabric. A number of studies using different techniques were used to characterize the fabric of an ice core [130].

The data recorded by string C, while the pinger stopped at 540 m depth (hole 81), is used to study the sound speed in the diagonal path which gives an indication about

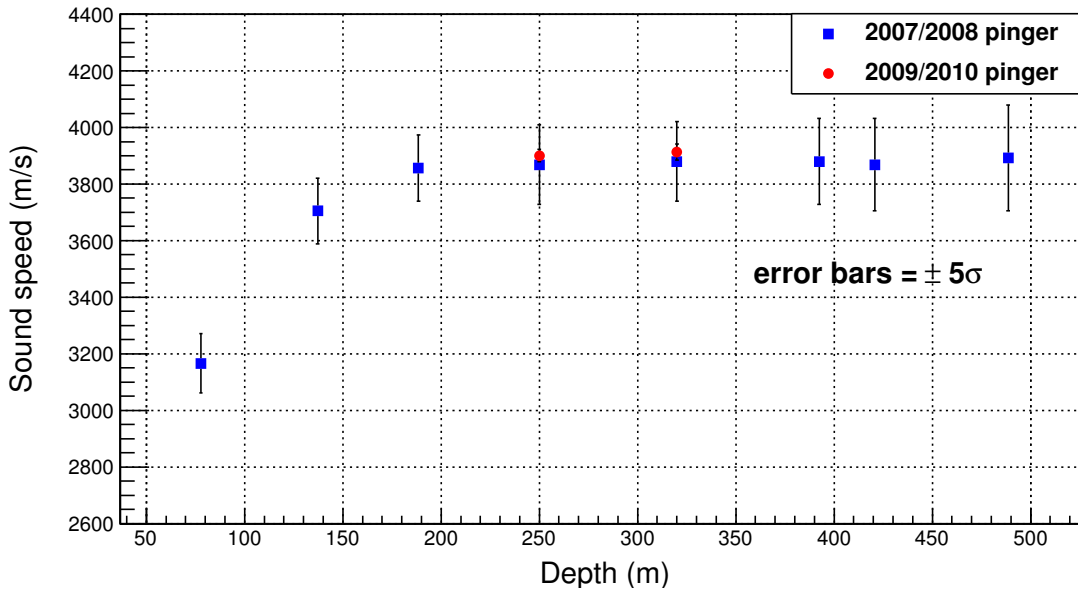


Figure 4.19: The measured sound speed, at frequency 30 kHz, versus depth. The previous measurements from 2007/2008 pinger data are shown for comparison. The error bars are 5σ to be visible.

the ice fabric. Waveforms recorded by CS4, CS5, CS6 and CS7 sensor channels are used. The propagation time for each waveform is extracted for 30 kHz pulses. The sound speed is calculated using the difference between two different diagonal paths (Δd) and their corresponding time difference (Δt). The possible combinations between the pinger and different sensors are used to get different ice cones and therefore ice paths, and hence different cone angles ($\Delta\theta$), see Fig. 4.20. Since any contribution from the depth uncertainty will change the calculated sound speed uncertainty, the actual pinger depth as estimated from the payout depth measurements (539.9535 m) with its uncertainty (0.22 m) are used. The other uncertainty sources for the horizontal distance or arrival time are treated as in the same-level calculations.

The calculated sound speed at different cone angles is summarized in Table 4.6 and shown in Fig. 4.21 with error bars of $\pm 1\sigma$. The sound speed is consistent within less than 1% uncertainty and does not show an angle or directional dependence. Therefore, the sound speed is predicted to be homogeneous and isotropic in South Pole ice between 190 m and 540 m and the grain orientation is expected to be random. The pressure waves from an interacting particle in ice can move homogeneously in the bulk ice. This gives a suitable and quite medium to build a large detector using the acoustic technique.

4.8. Sound speed measurements

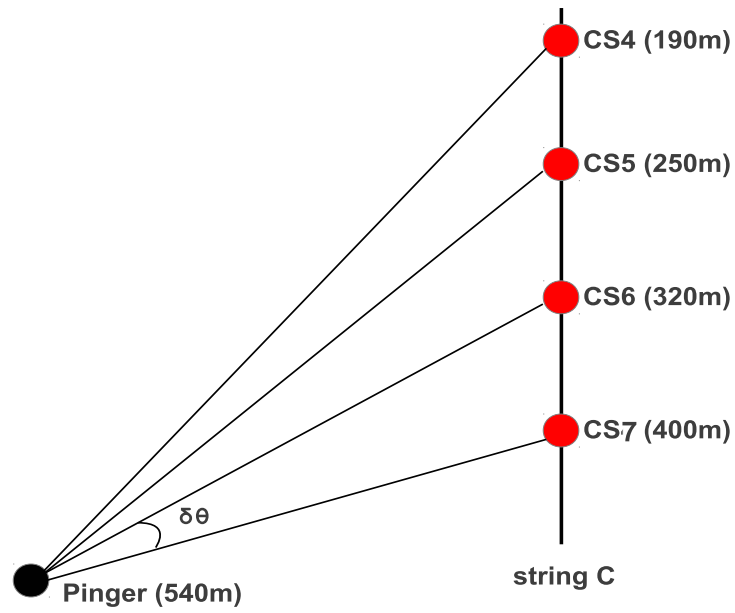


Figure 4.20: Schematic diagram for the pinger at 540 m and string C. The ice cone, with angle θ , is confined by two straight lined connecting two sensors and the pinger.

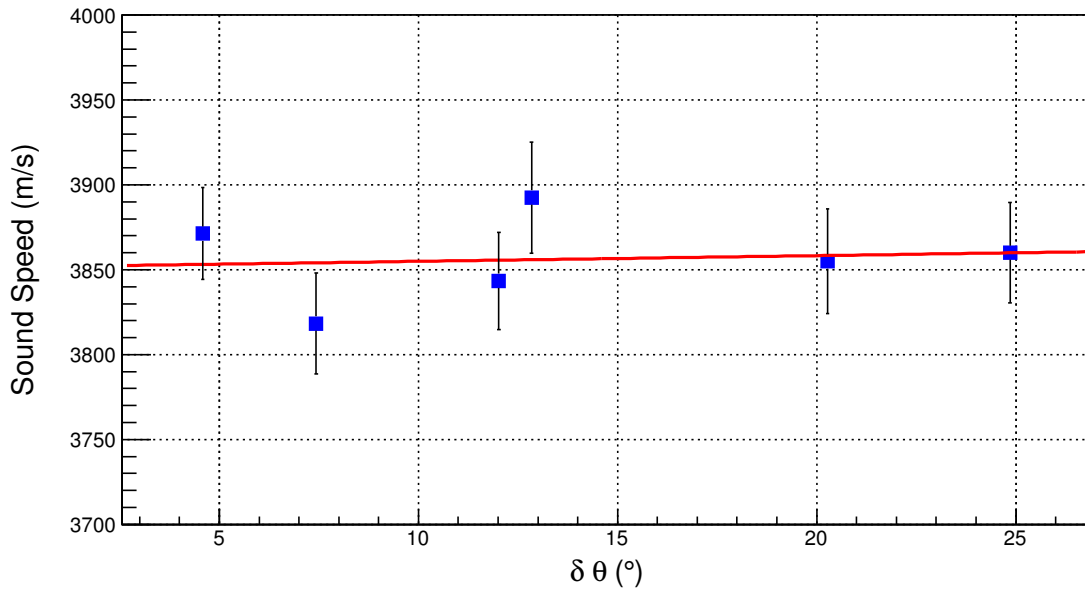


Figure 4.21: sound speed vs different angles. The error bars are $\pm 1 \sigma$.

<i>Sensors</i>	<i>Cone angle</i>	<i>Sound speed</i>
CS4-CS5	4.5838	3871.25 \pm 26.94
CS5-CS6	7.4337	3818.33 \pm 29.61
CS4-CS6	12.0175	3843.43 \pm 28.51
CS6-CS7	12.8384	3892.58 \pm 32.61
CS5-CS7	20.2721	3854.86 \pm 30.74
CS4-CS7	24.8559	3860.01 \pm 29.52

Table 4.6: Sound speed at different cone angles using different sensor combinations for string C (CS4, CS5, CS6 and CS7).

4.9 Conclusion

The pinger data from season 2009/2010 are used to perform a frequency study to the attenuation length and sound speed in the South Pole ice. SPATS sensors were used to record the pinger signals at different frequencies. From the same-level analysis, α shows no frequency dependence within the study region and therefore it is not dominated by scattering, but expected to be due to the absorption in ice. The measured values of α are consistent with the previous measurements and show no strong depth dependence.

Sound speed in bulk ice did not show any frequency or depth dependency and it is consistent with the previous measurements within a better than 1% uncertainty. The pressure pulse can move isotropically in ice in different directions showing the random ice fabric. Finally, these measurements are very useful for the further work on simulating the acoustic pulse propagation in ice, coming from interacting particles in ice, and to eventually build a large detector to detect high energy particles like a neutrino.

Simulating the Acoustic Signal from Neutrino Interactions

The acoustic signal is generated by the sudden local heating of the surrounding medium induced by the hadronic particle cascade produced at the interaction vertex by a UHE neutrino. To simulate the acoustic signal, the spatial distribution of the deposited energy by the hadronic particle cascade, is needed. The modified CORSIKA code is used to simulate the hadronic cascade in ice and to study the spatial distribution of the deposited energy, and the acoustic signal produced from these cascades. More details about the neutrino induced cascades and the generated acoustic signals will be presented.

5.1 Propagation and interaction of UHE neutrinos

The UHE neutrino arrives the Earth unperturbed because it is a weakly interacting particle. The neutrino cross section for interactions with nucleons increases with energy. As the total cross section for νN interaction increases, the corresponding interaction length decreases, and therefore the Earth will become opaque to ultra high energy neutrinos. Defining the interaction length as:

$$L_{int} = \frac{m_n}{\sigma_{tot}\rho} \quad (5.1)$$

where $\rho = 5.52 \text{ g/cm}^3$ is the mean density of the Earth, m_n is the nucleon mass and σ_{tot} is the νN cross section (valid for $E_\nu \geq 10^4 \text{ GeV}$) and given by [131]:

$$\sigma_{tot} = 1.2 \times 10^{-32} \text{ cm}^2 \left(\frac{E_\nu}{10^9 \text{ GeV}} \right)^{0.4} \quad (5.2)$$

The neutrino interaction length L_{int} is predicted to be smaller than the Earth radius R_E for energies above $3 \times 10^5 \text{ GeV}$. For an acoustic neutrino telescope, we thus consider only down-going neutrinos with energies $\geq 10^9 \text{ GeV}$ coming from above the horizon, i.e. with zenith angles $\theta < 90^\circ$. All up-going neutrinos from below the horizon are absorbed inside the Earth.

At the detector side, UHE neutrinos interact with the nucleons in the dense medium (water/ice) by DIS and generate a hadronic cascade, see § 2.1. The fraction of the initial energy E_ν that is carried by the hadronic channel E_{had} , called the "inelasticity":

$$y = \frac{E_\nu - E_{lept}}{E_\nu} = \frac{E_{had}}{E_\nu} \quad (5.3)$$

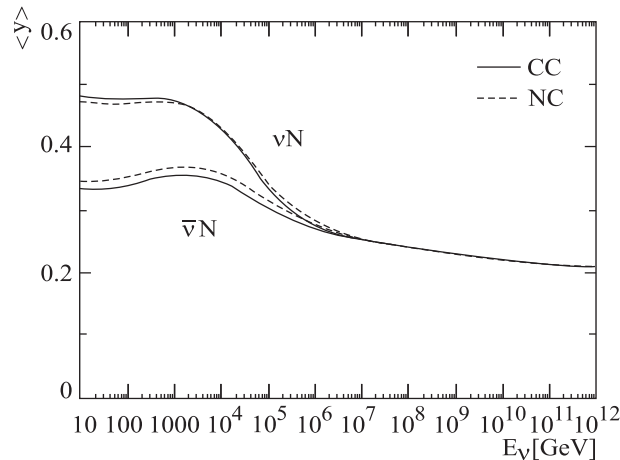


Figure 5.1: The inelasticity $\langle y \rangle$ for ν and $\bar{\nu}$ for different neutrino energies.

where y is the Bjorken scaling variable representing the collision inelasticity [132] and E_{lept} is the energy carried by the outgoing leptons. Physically y describes the fraction of the incident neutrino energy that is carried away by the hadronic cascade. Fig. 5.1 shows the mean inelasticity for ν and $\bar{\nu}$ for different neutrino energies. For high energies, the distribution is rather energy independent. The mean fraction of the neutrino's energy imparted to the hadronic cascade is approximately 20% at high energy. However, the actual value can vary from 0 – 100% [54], so that in some cases the majority of the energy of the incoming neutrino can be transferred to the hadronic cascade.

5.2 Modified CORSIKA in water/ice

CORSIKA¹ (COsmic Ray SIMulations for KAscade) [133] is the most extensive ultra high energy simulation program which has so far been developed to simulate in detail the development of extensive air showers in the atmosphere initiated by high energy cosmic ray particles. Protons, light nuclei up to iron, photons, and many other particles may be treated as primaries. The particles are tracked through the atmosphere until they undergo reactions with the air nuclei or decay. The hadronic interactions at high energies may be described by any reaction model alternatively: VENUS, QGSJET, DPMJET, SIBYLL, EPOS and HDPM. Hadronic interactions at lower energies are described either by the more sophisticated GHEISHA interaction routines or the rather simple ISOBAR model. For electromagnetic interactions the shower program EGS4 or the analytical NKG formulas may be used. On the other hand, options for the generation of Cherenkov radiation and neutrinos exist.

To build an UHE neutrino telescope using the acoustic technique, acoustic signals from interactions of UHE cosmic ray neutrinos in a dense medium have to be studied.

¹CORSIKA was developed to perform simulations for the KASCADE experiment at Karlsruhe in Germany

Since there are no experimental data on the interactions of such high energy particles, theoretical models were used to simulate them. Many efforts to simulate the acoustic pulse, in water, have been made using the Geant4 package² [134, 135]. However, GEANT4 is restricted to energies of less than 10^5 GeV for hadron showers, since the range of validity of the physics models in this package does not extend to higher energy hadrons. Comparing CORSIKA with other simulation tools like GEANT4 or ZUS [136]. In addition, GEANT4 can not simulate the LPM effect. However, ZUS [136] (another simulation tool) simulates the LPM effect but it can not simulate hadronic interactions. CORSIKA can simulate hadronic interactions with the LPM effect in wider energy range. It was modified by ACORNE group to simulate hadronic interactions in water, which could be used as a step to modify CORSIKA to work in water and ice. Therefore, CORSIKA is the best solution to carry out such high energy simulations.

As CORSIKA is devoted to cascade simulations in air, several modifications have been made in order to adapt the code to simulate a cascade in a uniform density medium. The development of cosmic ray showers in solids and liquids is essentially the same as the development in air if the column density (g/cm^2) is used instead of distance. The same treatment of the cosmic ray showers can be used for air and for solids and liquids. CORSIKA 6204 was initially modified by the ACoRNE collaboration [137], called "CORSIKA-W" (W for "Water"), to simulate the cascades in salt-water. Based on these modifications and taking them a step further to get more functionality and more flexibility, CORSIKA 6600 was used for further modification by J. Bolmont for IceCube collaboration, called "CORSIKA-IW" (IW for "Ice & Water") [138]. The main limitation of the CORSIKA-W code was that the choice of some options is already done and can not be changed by the user, e.g. the hadronic package QGSJET is selected and the use of any other hadronic interaction model is impossible. Also, the size of the simulated volume is fixed to 20 m. On the other hand, the modifications for CORSIKA-IW allow us to switch the medium from air to ice during the configuration step (see Fig. 5.2), use different simulation packages (VENUS, QGSJET and others) available with CORSIKA, and use all the other options available in CORSIKA, whenever they are relevant to a simulation in water/ice. A new datacard entry, called "VOLHEI", was added to change the height of the simulated volume. CORSIKA-IW has been used to simulate the very high energy electromagnetic cascades in the LPM regime with IceCube [139]. It was tested and compared with GEANT4 and CORSIKA-W, see Fig. 5.3.

Since only the density and chemical composition affect the interaction cross-section of high energy particles, the density and chemical composition are modified for salt-water and ice as needed in the code. In CORSIKA, the atmosphere is divided into 5 layers. In the case of ice or salt-water, we need only one of these layers. Therefore the variable density needed for an air atmosphere is modified to use a medium of constant density, $1.025 \text{ g}/\text{cm}^3$ in salt-water and $0.918 \text{ g}/\text{cm}^3$ in ice. The atmosphere's composition is defined as containing nitrogen, oxygen and argon. To maintain the structure of the program as closely as possible to the air shower version, the composition should stay the same as

²<http://geant4.web.cern.ch/geant4/>

```

Welcome to the CORSIKA extraction macro
=====

create an executable of a specific CORSIKA version

Please read the documentation for a detailed description
of the options and how to use it.

Note : press Enter (blank line) to select an option followed by "(default)"

grep: include/config.h: No such file or directory
grep: include/config.h: No such file or directory
-----

Which material do you want to use ?
1 - AIR (default)
2 - ICE
3 - SALT WATER

r - restart make
x - exit make
(only one choice possible)
    
```

Figure 5.2: Startup window for CORSIKA-IW showing the choice between different media.

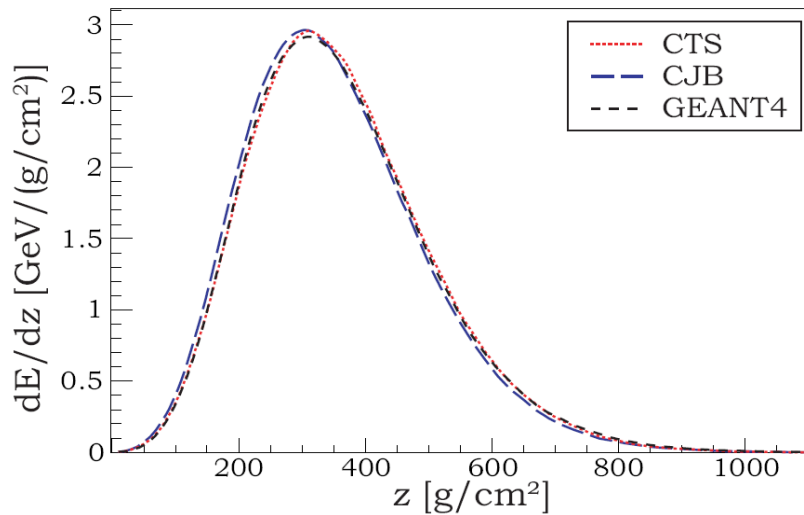


Figure 5.3: Average longitudinal profile of one hundred 1 TeV showers. Comparison between CORSIKA-IW (CJB), CORSIKA-W (CTS) and GEANT4.

the original version in air. In ice, there are only two chemical components: hydrogen and oxygen and the third component is not used (set $A = Z = 0$). In water, hydrogen, oxygen and NaCl ($A = 29.2$ and $Z = 14$, the average of sodium and chlorine) are used. The stopping power formula, which affects the energy loss for hadrons, was modified to allow the density effect in water/ice. Another important change was done to the EGS4 package, which treats the cross sections for electromagnetic processes, to re-generate the EGS input file according to the medium (ice/water).

To conclude, the modified version of CORSIKA is dedicated to simulation of particle interactions in salt water or ice. All needed options are available, as in the original version of CORSIKA. All the hadronic packages have been tested, only EPOS and DPMJET do not work properly [138].

5.3 Neutrino induced cascades in ice

The fraction of the neutrino energy carried by the hadronic component, when an UHE neutrino interacts with an ice nucleon, is used to initiate a cascade. To simulate the neutrino induced cascades in ice, a π^+ meson with energy equal to yE_ν is used to simulate the hadronic cascade using CORSIKA-IW. The average energy transferred to the hadronic cascade vary from 0.332 to 0.205 for $E_\nu = 10^5$ GeV to 10^{12} GeV [54]. π^+ represents the hadronic cascade due to the neutrino interaction. It initiates the hadronic shower simulation in ice. The QGSJET (version 01c) model is used to simulate the hadronic interactions, while EGS4 is used to simulate the electromagnetic component of the shower (more details about these models in the CORSIKA manual). The thinning option is used to reduce the computing time. In the thinning option, below a certain fraction of the primary energy (10^{-4} is used) only one of the particles emerging from the interaction is followed and an appropriate weight is given to it. The thinning level (E/E_o) represents the ratio for all secondary particles with energy E to the primary energy E_o particles. If the energy sum of all secondary particles falls below the thinning level, only one of the secondary particles is followed, selected at random. Also an appropriate weight is attributed to the surviving particle to conserve its energy. However, if the energy sum of the corresponding particles exceeds the thinning level, more than one particle is enabled to survive.

The simulation is carried out in a vertical column of 25 m long and 1 m radius. The neutrino interacts at the top of the ice column ($z = 0$), where the z axis is the axis of the column. The shower is binned into 20 g/cm^2 observation levels. To get the spatial distribution of the deposited energy from the simulated shower, the AUGERHIST option is chosen which gives the deposited energy per 1 g/cm^2 at the observation level [140]. Once the simulation is started, a particle propagates through the simulated volume losing energy via the production of secondary particles. The energy deposition from different secondary particles is recorded at each depth. The simulation is continued until the shower particles reach a pre-defined energy threshold. We used 3 MeV for electromagnetic particles and 0.3 GeV for hadrons. When a particle reaches its energy threshold, no further secondaries

will be produced and its energy is added to the 1 g/cm^2 slice where the particle stops.

5.3.1 ACORNE parameterisation

In comparison to water, not much work has been done to study hadronic showers in ice. In this work, the neutrino-induced hadronic shower is simulated. This was done by simulating the interaction of π^+ in ice, assuming that it carries the total energy given to the hadronic shower from the neutrino interaction. The ACORNE group used P as a primary particle to simulate the hadronic shower in water. The radial and longitudinal profiles were parameterised by simulating the shower generated by the proton interaction in water, using the modified CORSIKA-W. Since this parameterisation was done in g/cm^2 , it is applicable to ice too. The differential energy deposited was parameterised as follows [137]:

$$\frac{d^2E}{drdz} = L(z, E_L) \times R(r, z, E_L) \quad (5.4)$$

where;

- z : the longitudinal distance from the interaction point.
- r : the radial distance from the shower axis.
- E_L : $\log_{10}E$ where E is the total shower energy.
- $L(z, E_L)$: represents the longitudinal distribution of deposited energy.
- $R(r, z, E_L)$: represents the radial distribution of deposited energy.

The longitudinal distribution ($\frac{dE}{dz} = L(z, E_L)$) is a modified version of the Gaisser-Hillas function [141] and given by:

$$L(z, E_L) = P_{1L} \left(\frac{z - P_{2L}}{P_{3L} - P_{2L}} \right)^{\frac{P_{3L} - P_{2L}}{P_{4L} + P_{5L} + P_{6L}z^2}} \exp \left(\frac{P_{3L} - z}{P_{4L} + P_{5L} + P_{6L}z^2} \right) \quad (5.5)$$

where P_{nL} are parameterised as quadratic functions of E_L with value:

$$\frac{P_{1L}}{E} = 2.760 \cdot 10^{-3} - 1.974 \cdot 10^{-4}E_L + 7.450 \cdot 10^{-6}E_L^2 \quad (5.6)$$

$$P_{2L} = -210.9 - 6.968 \cdot 10^{-3}E_L + 0.1551 \cdot E_L^2 \quad (5.7)$$

$$P_{3L} = -41.50 + 113.9E_L - 4.103 \cdot E_L^2 \quad (5.8)$$

$$P_{4L} = 8.012 + 11.44E_L - 0.5434 \cdot E_L^2 \quad (5.9)$$

$$P_{5L} = 0.7999 \cdot 10^{-5} - 0.004843E_L + 0.0002552 \cdot E_L^2 \quad (5.10)$$

$$P_{6L} = 4.563 \cdot 10^{-5} - 3.504 \cdot 10^{-6}E_L + 1.315 \cdot 10^{-7}E_L^2 \quad (5.11)$$

where P_{1L} represents the peak energy deposited and P_{3L} the depth in the z coordinate at this peak. However, P_{2L} , P_{4L} , P_{5L} and P_{6L} are related to the shower width and shape in z .

The radial distribution ($\frac{dE}{dr} = R(r, z, E_L)$) is represented by the NKG function [141] and given by:

$$R(r, z, E_L) = \frac{1}{I} \left(\left(\frac{r}{P_{1R}} \right)^{(P_{2R}-1)} \left(1 + \frac{r}{P_{1R}} \right)^{(P_{2R}-4.5)} \right) \quad (5.12)$$

where I is given by:

$$I = \int_0^\infty \left(\left(\frac{r}{P_{1R}} \right)^{(P_{2R}-1)} \left(1 + \frac{r}{P_{1R}} \right)^{(P_{2R}-4.5)} \right) dr = P_{1R} \frac{\Gamma(4.5 - 2P_{2R})\Gamma(P_{2R})}{\Gamma(4.5 - P_{2R})} \quad (5.13)$$

where the parameters P_{nR} (with $n = 1, 2$) are represented by the quadratic form;

$$P_{nR} = A + Bz + Cz^2 \quad (5.14)$$

where the quantities A, B, C are parameterised as quadratic functions of E_L . This gave for P_{1R} :

$$A = 0.9636 - 0.2573E_L + 0.01287 \cdot E_L^2 \quad (5.15)$$

$$B = 0.0005404 + 0.0008072E_L - 0.4697 \cdot 10^{-4}E_L^2 \quad (5.16)$$

$$C = 4.488 \cdot 10^{-6} - 1.375 \cdot 10^{-6}E_L + 0.7344 \cdot 10^{-7}E_L^2 \quad (5.17)$$

and for the parameter P_{2R} :

$$A = 1.969 + 0.007727E_L - 0.8905 \cdot 10^{-3}E_L^2 \quad (5.18)$$

$$B = -5.093 \cdot 10^{-6} - 0.0001782E_L + 0.1173 \cdot 10^{-4}E_L^2 \quad (5.19)$$

$$C = -0.1069 \cdot 10^{-8} + 0.1524 \cdot 10^{-6}E_L - 0.1058 \cdot 10^{-7}E_L^2 \quad (5.20)$$

This parameterisation gives a similar acoustic signal as it is given from the CORSIKA-W showers. There is a good agreement (within 5% at the peak) between the acoustic signal computed using this parameterisation and that taken directly from the CORSIKA-W showers [137].

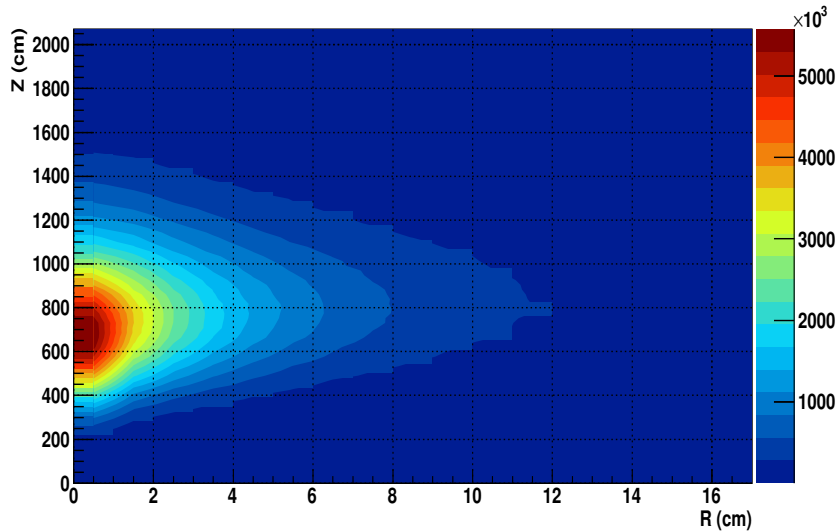


Figure 5.4: The energy density deposited by a hadronic shower (π^+) in ice started by $E_\nu = 10^{11}$ GeV neutrino. The color scale gives the energy density in GeV/cm^2 .

5.3.2 Shower properties in ice

Once the primary particle starts the interaction with a nucleon in the medium, a shower of secondary particles is generated which propagates and creates further secondaries. These particles release their energy through their interactions. To get the deposited energy from the shower, 100 showers are generated at each energy from 10^5 to 10^{12} GeV, in step of integer powers of 10, then they are averaged and binned into $20 \text{ g}/\text{cm}^2$ slices longitudinally and 1 cm annular cylinders radially. The 1 cm radial binning is used because most of the shower energy is deposited within about 5 cm around the shower axis. The simulation starts at the top of the simulated volume. The simulation in ice is carried out by using π^+ meson as a hadron carrying approximately 20% of the incident neutrino energy.

The primary particle with high energy, and hence its secondary particles, will be able to travel further in the simulated medium and distribute its energy in both longitudinal and radial directions. Therefore, the shape of the shower depends on the shower energy, but not strongly at high energies ($> 10^9$ GeV) where the energy is high enough to give similar energy distributions. Fig. 5.4 shows the energy density deposited by π^+ in ice, when the shower is started by $E_\nu = 10^{11}$ GeV. The total shower energy is deposited in a cylindrical volume of about 10 m length and 5 cm radius.

5.3.3 Longitudinal shower distribution

The hadronic cascade's particles deposit their energy in longitudinal slices as they move in the detection medium until a threshold value is reached, then it stops. The longitudinal profile of the hadronic shower varies with shower energy. The longitudinal profile

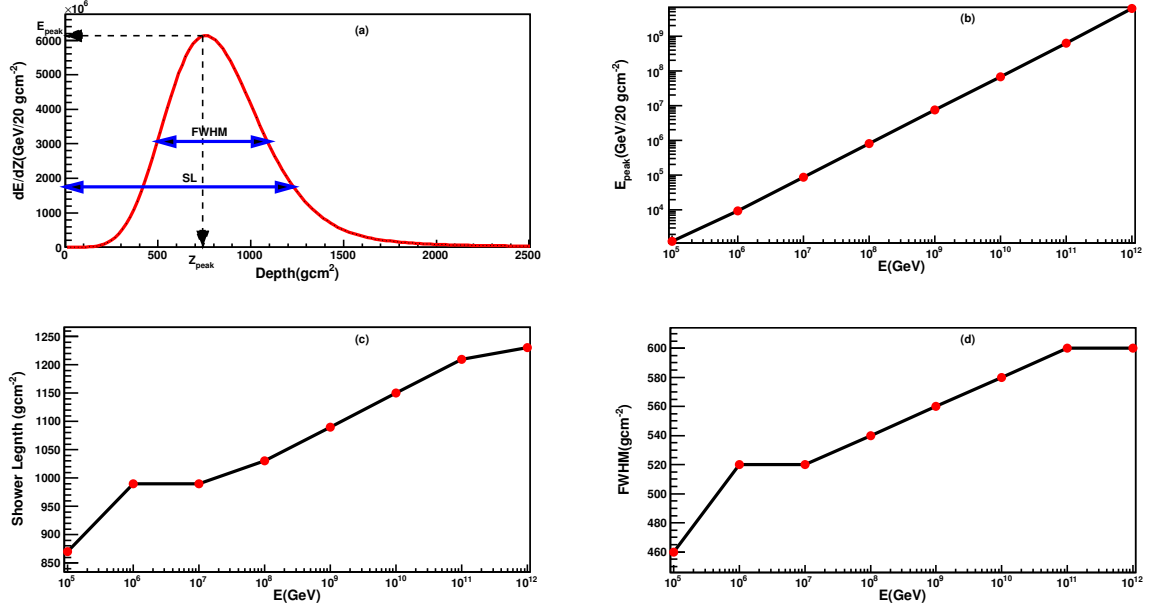


Figure 5.5: Longitudinal shower parameters. (a) Longitudinal shower started by $E_\nu = 10^{12}$ GeV. E_{peak} , Z_{peak} , SL and FWHM of the shower are shown. (b) Peak energy versus neutrino energy. (c) Shower length versus neutrino energy. (d) FWHM versus neutrino energy.

properties are shown in Fig. 5.5, they can be described by:

- **Shower length (SL):** the length where the accumulated energy is 90% of the total deposited energy. At 10^{12} GeV, it is 1.5 larger than at 10^5 GeV.
- **Peak position (Z_{peak}):** the depth where the maximum energy deposition exists or the position of the shower centroid when the radial energy is deposited equally. It varies from 466 g/cm² at 10^5 GeV to 770 g/cm² at 10^{12} GeV.
- **Peak energy (E_{peak}):** the energy at peak position Z_{peak} and its value relative to the shower energy changes from 0.038 at 10^5 GeV to 0.032 at 10^{12} GeV.
- **Full width at half maximum (FWHM):** the shower width at energy equal to $E_{peak}/2$, it increases with energy like the shower length. At 10^{12} GeV it is 1.25 times its value at 10^5 GeV.

Fig. 5.6 shows the deposited energy per 20 g/cm² slice through the shower axis from a 10^{11} GeV neutrino using CORSIKA-IW, compared to the ACORNE parameterisation. The longitudinal shower profile at different energies are presented in Appendix C. The longitudinal profile from CORSIKA-IW is consistent with ACORNE parameterisation within a 20 g/cm² shift. This shift could be due to using different particles, π^+ for this work and proton for the parameterised simulation. The difference in the cross section

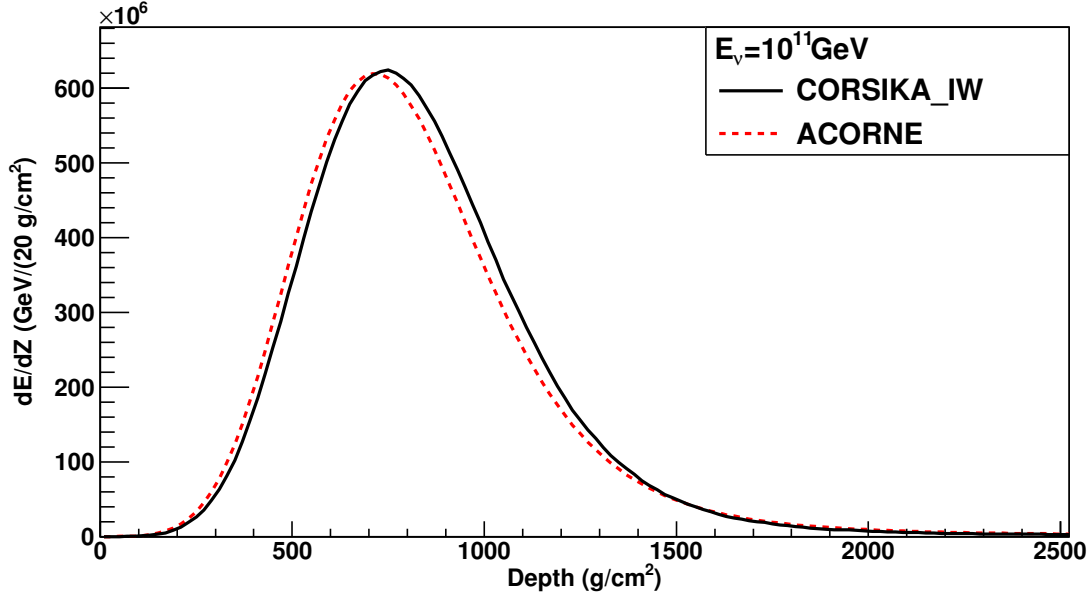


Figure 5.6: Averaged longitudinal energy deposited per 20 g/cm^2 for 100 showers at neutrino energy 10^{11} GeV versus depth in ice, using CORSIKA-IW. The longitudinal profile using the ACORNE parameterisation is shown for comparison.

could give this slight shift in depth. However, the longitudinal energy distribution for both showers has the same shower parameters and gives the same total shower energy. The deposited energy decreases with depth (age) because the radial distribution gets broader. The relation between the shower energy and the shower peak position Z_{peak} is shown in Fig. 5.7. The shower peak position increases with the shower energy.

5.3.4 Radial shower distribution

During the shower's particles journey in the medium, they propagate and lose energy radially as they do longitudinally. Fig. 5.8 shows the radial distributions of the deposited energy in ice at different depths from CORSIKA-IW compared to the ACORNE parameterisation, see Appendix C for more radial distributions at different energies. Most of the shower energy is deposited in the inner core of the shower. However, the radial energy deposition decreases with the distance from the shower axis. The radial deposited energy affects the shape of the longitudinal distribution. The acoustic signal from a shower is sensitive to the radial energy distribution, particularly the inner core near to the shower axis. The radial energy distribution from CORSIKA-IW shows agreement with the predicted distribution by ACORNE group for the inner core around the shower axis where they used the same binning width, 1 cm, as used in this work. However, the inconsistency with distances larger than 10 cm could be due to using different binning where the ACORNE used 10 cm binning while 1 cm is used in this work or the slight depth shift for

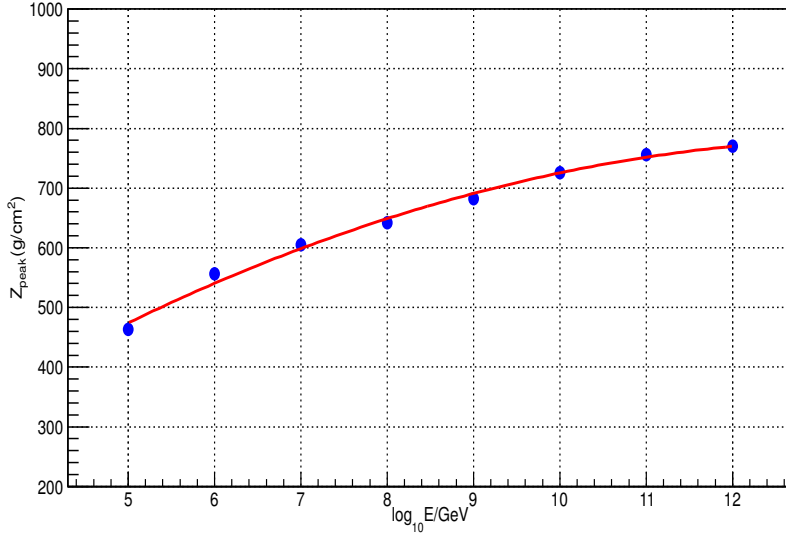


Figure 5.7: The depth of the shower peak, for averaged 100 showers, versus E using CORSIKA-IW. The line shows a quadratic fit to the data points.

the longitudinal energy deposition.

5.4 Acoustic signal

The interactions of ultra high energy neutrinos with energy $> 10^9 \text{ GeV}$ can deposit sufficient energy to generate a measurable acoustic signal in the surrounding medium. The generated acoustic energy is confined in a thin pancake, with a width of $\sim 1^\circ$, perpendicular to the shower axis. An acoustic signal propagating through a medium is attenuated by the medium. The effect of the incident neutrino energy, the distance from the source center and the angle relative to the plane perpendicular to the shower axis on both the maximum peak amplitude P_{max} and the median signal frequency will be presented.

5.4.1 Generation

As explained in § 3.1, the speed of the acoustic signal which is generated by the hadronic shower in ice is much less than the speed of the shower propagation. Therefore, the energy deposition along the length of the shower can be considered to be quasi-instantaneous, giving rise to an acoustic line-source. In the far-field ($R > 100 \text{ m}$), the acoustic emission is coherent and gives rise to bipolar pressure pulses propagating approximately at right angles to the shower axis with a velocity of 3920 m/s (in ice). According to Fraunhofer diffraction, the acoustic signal with wavelength λ produced by a hadronic shower with length L will have an angular spread which given by λ/L . This spread yields an acoustic

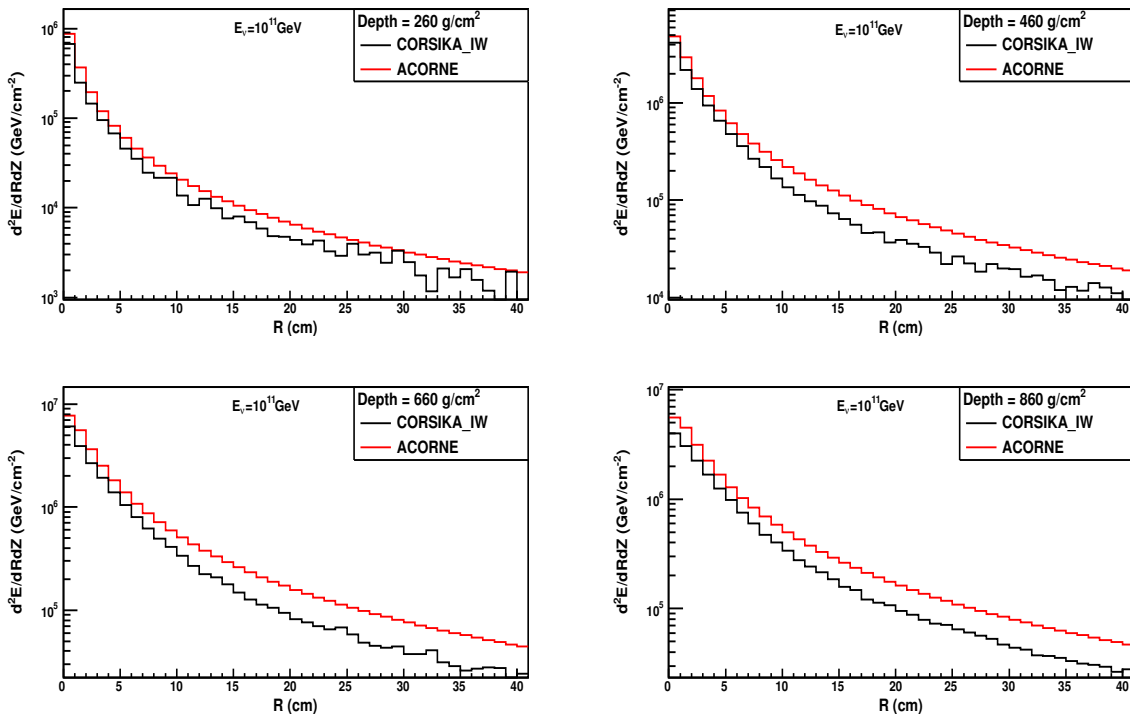


Figure 5.8: The averaged radial energy distribution at different depths for 100 showers in ice at neutrino energy 10^{11} GeV using CORSIKA-IW. The radial distribution using the ACORNE parameterisation is shown for comparison.

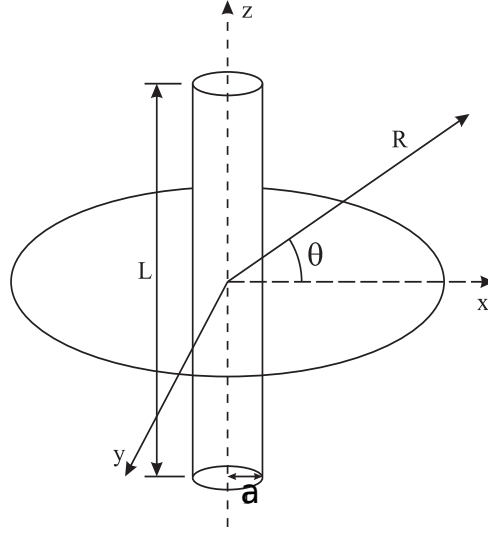


Figure 5.9: A schematic view of the deposited energy from the hadronic cascade as a cylinder, with length L and radius a . The detection point is at distance R from the shower axis and angle θ relative to the plane perpendicular to the cascade axis.

disk with a width of the order of 1 degree. In the plane perpendicular to the shower axis, where most of the acoustic energy is contained through the longitudinal shower peak position Z_{peak} , the magnitude of the pressure pulse is highest and it falls off very rapidly out of this plane. Fig. 5.9 shows more details about the geometry relevant to the shower and the thin acoustic disk, which is called "pancake", perpendicular to the shower axis.

The energy deposition has a symmetric distribution around the shower axis (i.e. z -direction). In the far field, the observer will be far away from the source (i.e. x -direction) and therefore the shower will be seen as a point-like source. However, the shower width will be seen as close to zero for the x -axis and y -axis and their energy contribution ($E(y')$ and $E(z')$) will resemble a delta-function. At time t , the wave Eq. 3.4 can be given by:

$$\begin{aligned}
 p(t) &= -\frac{\alpha}{4\pi C_p} v^2 \frac{\partial}{\partial R} \int_{S_r^R} \frac{q(\vec{r}')}{R} d\sigma \\
 &\approx -\frac{\alpha}{4\pi C_p R} v^2 \frac{d}{dx'} E(x')
 \end{aligned} \tag{5.21}$$

Each portion of the extended acoustic source is considered as a point-like source which generates a pressure wave in the homogeneous medium. At a distance R from the acoustic source center, the acoustic pulse is due to the sum of the elementary perturbations from each source portion. Since the cascade energy is deposited instantaneously, each portion of the acoustic source pops up simultaneously, and therefore reach the detection point at different times because of different distances that each contribution has to travel.

The acoustic signal amplitude at a point \vec{r} with a distance R from the shower center, in the $x - y$ plane, is computed by using Eq. 3.4. The distance between each point,

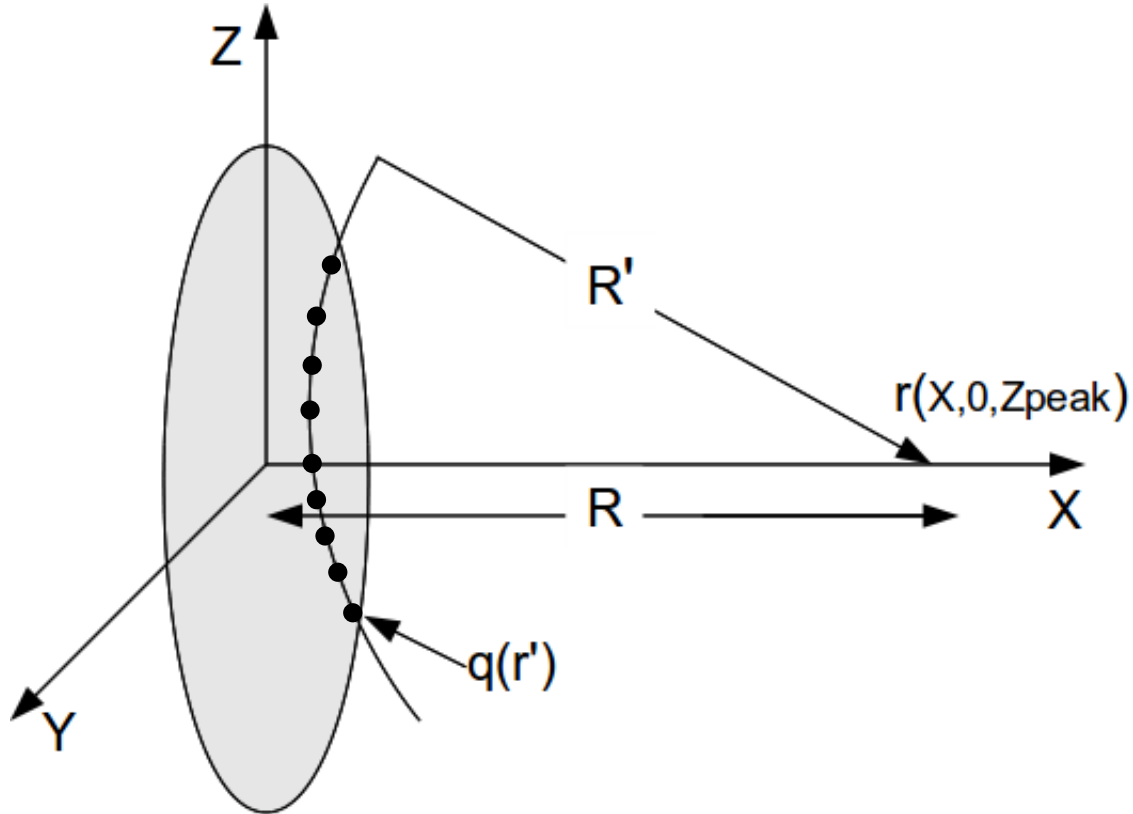


Figure 5.10: Sketch showing the integration from different shower portions. The observer is on the plane orthogonal to the shower axis and at a distance R from the shower center.

with energy density $q(\vec{r}')$, in the acoustic source and the detection point is calculated as shown in Fig. 5.10. Distances for all points in the shower where the energy is deposited are binned into a histogram with bin width dR . Each bin content is the equivalent of integrating the spatial energy deposited over the surface of a sphere, with thickness dR , which is centered at the detection point. Different bins contain the integrated energy density dE from different spherical surfaces with different radii from the detection point. The variation dR plays a role when computing the derivative as difference quotient. The smaller it is, the more accurate the computation. dR is chosen to give a 200 kHz sampling frequency rate, the same as SPATS sampling rate.

The derivative for the integrated energy, dE/dR , gives a bipolar acoustic pulse $P(t)$ at distance R from the shower center which corresponds to time $t = R \cdot v$, where v is the speed of sound in ice. Fig. 5.11 gives an example for the integrated energy density and the resulting acoustic pulse from a hadronic shower generated by a 10^{11} GeV neutrino, at a distance 1 km from the shower center on the plane perpendicular to the shower axis. The pulse is centered at $t = R \cdot v$.

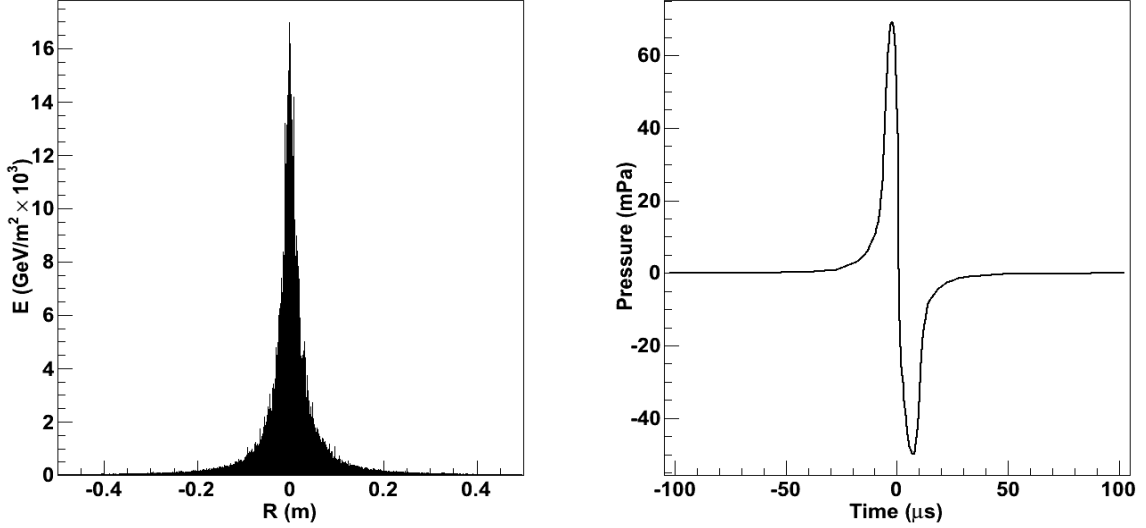


Figure 5.11: The integrated energy density (left) and the resulting acoustic pulse (right) from a 10^{11} GeV neutrino shower at a distance of 1000 m from the shower axis at the plane perpendicular to the shower axis.

5.4.2 Attenuation

An acoustic signal propagating through a medium is attenuated by the medium. This attenuation may be due to scattering and/or absorption. Recent measurements by SPATS, in §4, found that the acoustic attenuation mechanism in ice is not frequency dependent and the attenuation length is about 300 m. These measurements are consistent with the earlier results from the 2008/2009 measurements. Since the attenuation due to scattering is frequency dependent, the attenuation in ice is dominated by absorption. The measured attenuation length is factored in to the propagation of the acoustic signal in ice.

For the spherical symmetry in the far-field, the pressure amplitude is attenuated by the geometrical distance to the source as $1/R$ in addition to the amount of attenuation due to the medium (ice) $e^{-R/\lambda}$ as:

$$P(R) = P_0 \frac{R_0}{R} e^{-\alpha(R-R_0)} = P_0 \frac{R_0}{R} e^{-(R-R_0)/\lambda} \quad (5.22)$$

where:

- P is the pressure amplitude (in Pa) at a distance R from the source.
- P_0 is the pressure at a reference distance R_0 .

In the far-field ($R \gg R_0$), $R_0 = 1$ and this equation can be given by:

$$P(R) = \frac{P_0}{R} e^{-\alpha R} = \frac{P_0}{R} e^{-R/\lambda} \quad (5.23)$$

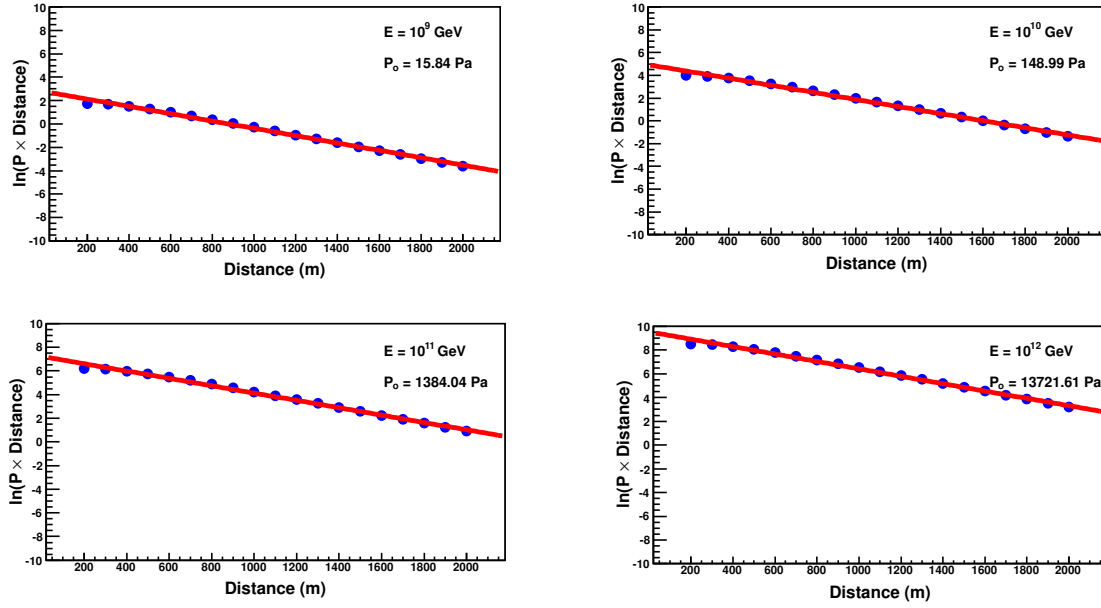


Figure 5.12: $\ln(P \times \text{distance})$ as a function of the distance from the source for different neutrino energies. The acoustic pressure at the source is calculated from the intersection of the linear fit.

this equation can be turned into the linear equation:

$$y = \ln(P \times R) = -\alpha R + \ln(P_0). \quad (5.24)$$

a linear fit can be performed to get $P_0 = e^b$ using the model:

$$y = -\alpha R + b \quad (5.25)$$

The pressure amplitude at the source increases with incident neutrino energy, as the total deposited energy. Fig. 5.12 shows the calculated P_0 , using Eq. 5.24, for different energies. P_0 varies from 15.8 nPa/GeV to 13.7 nPa/GeV with energy varying from 10^9 GeV to 10^{12} GeV. This variation is expected due to the fact that the mean inelasticity reduces slightly with energy at this energy range [54]. Therefore, the total deposited energy, and thus the deposited energy per GeV, will vary according to the inelasticity value as will the produced acoustic pressure amplitude per GeV. Fig. 5.13 shows the acoustic pressure pulse at 1 km from the shower center in the pancake plane for different incident neutrino energies. The pressure amplitude is scaled to the initial neutrino energy at the interaction point. On the other hand, the average $P_0 \sim 14.6$ nPa/GeV, could be used within this energy range to calculate the pressure amplitude at any distance for any given neutrino energy.

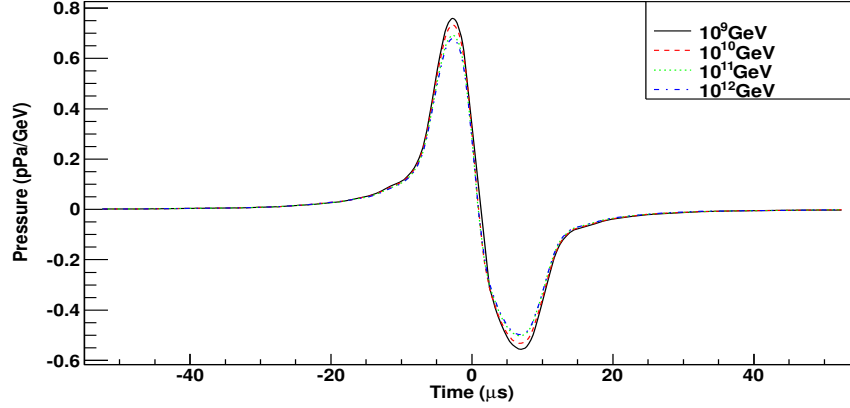


Figure 5.13: The pressure signal at 1 km from the source on the pancake plane for different neutrino energies.

5.4.3 Distance dependence

The amplitude of the acoustic signal decreases as it travels away from the source due to the attenuation. Fig. 5.14 shows the acoustic signal amplitude as a function of the distance on the plane perpendicular to the shower axis and its asymmetry ($\frac{|P_{max}| - |P_{min}|}{|P_{max}| + |P_{min}|}$) at different energies. The asymmetry of the acoustic signal amplitude is shown as a function of distance, where it is not totally symmetric around the shower axis and decreases at large distances.

The signal amplitude and frequency composition of the acoustic pressure signal are studied at different distances on the plane perpendicular to the shower axis, see Fig. 5.15. The signal amplitude, and therefore its energy, decreases with distance, but the shape of the signal spectrum and its frequency remains constant. The median frequency (F_o) of the acoustic signal, the frequency at which the accumulative intensity (or power) is 0.5 of the total accumulative intensity (or power) of the spectrum, is calculated as a function of the distance from the shower center as shown in Fig. 5.16. F_o increases slightly with distance when it is close to the shower axis, however it is found to be constant and about 43 kHz at large distances.

The signal height increases with energy at the same detection point. Fig. 5.17 shows the maximum and minimum pulse amplitudes versus energy. The linear fit shows the linear proportionality between the signal pressure and the shower energy. Simply, this relation is given by:

$$\log_{10}(P_{max}) = 0.999(\pm 0.0054)\log_{10}(E) - 12.923(\pm 0.48) \quad (5.26)$$

where P_{max} is the maximum pressure in Pa and E is the energy in GeV. The quoted errors are the statistical errors from the fit.

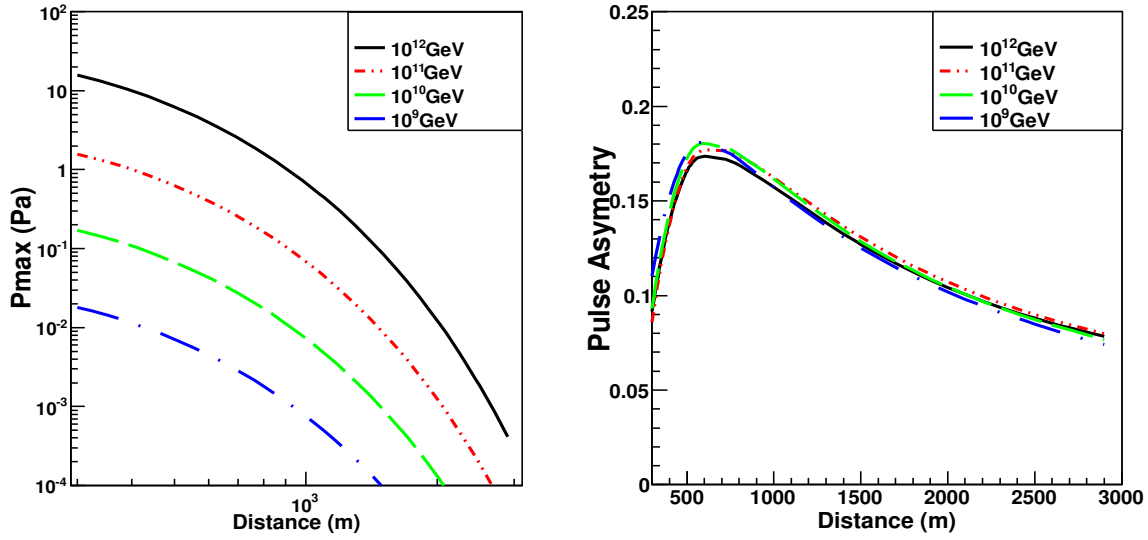


Figure 5.14: The maximum pressure signal amplitude (left) and its asymmetry (right) as a function of the distance from the shower axis on the plane perpendicular to it for different energies.

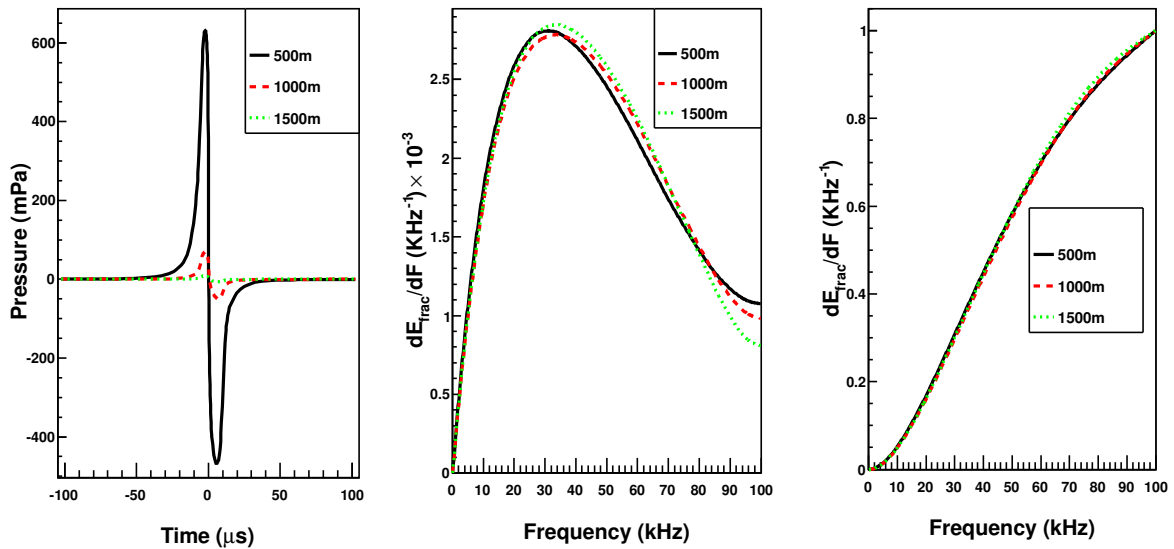


Figure 5.15: The pressure signal amplitude(left), its frequency composition (middle) and their cumulative frequency spectra (right) at different distances on the plane perpendicular to the shower axis. The shower is generated by a neutrino with energy 10^{11} GeV.

5.4. Acoustic signal

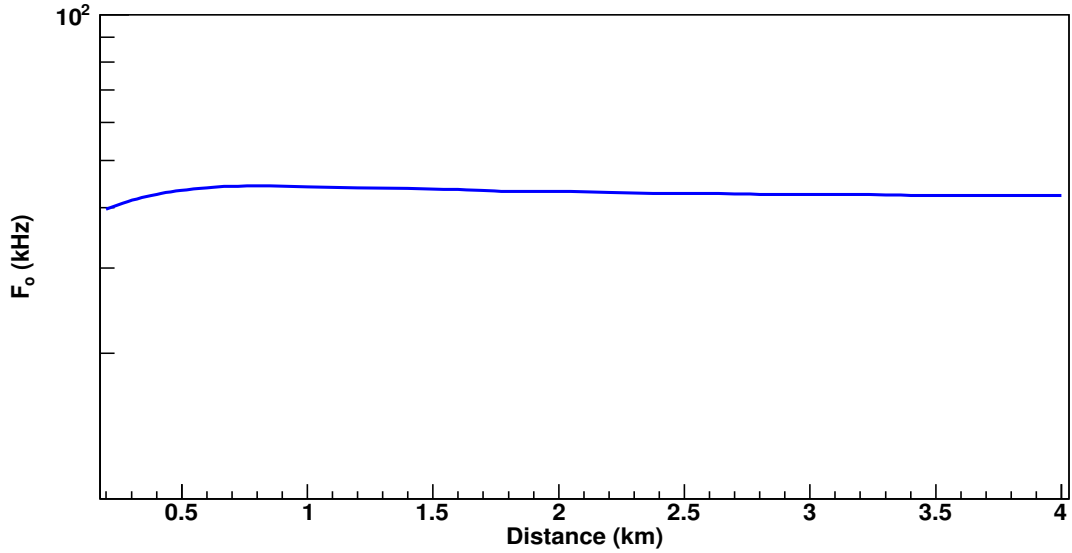


Figure 5.16: Median frequency for the acoustic signal versus distance on the plane perpendicular to the shower axis. The shower is generated by 10^{11} GeV neutrino.

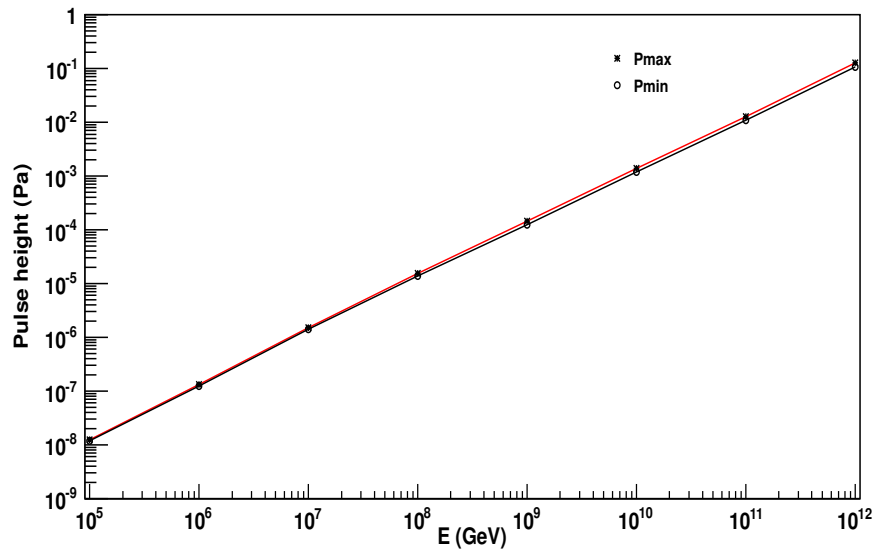


Figure 5.17: The maximum and minimum pulse heights versus energy at 1 km distance from the shower axis on the plane perpendicular plane to the shower axis.

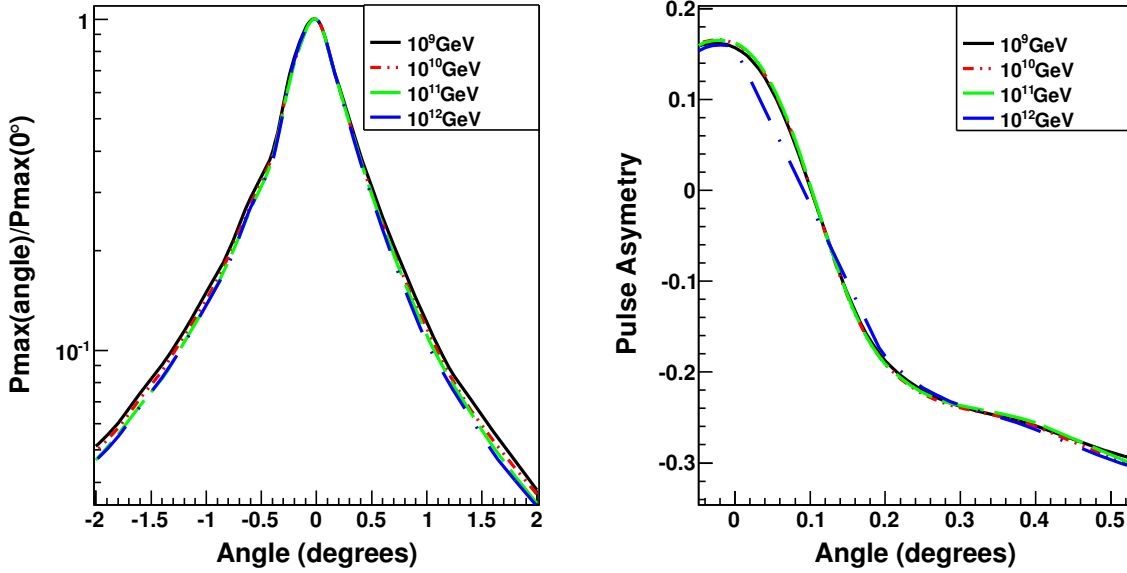


Figure 5.18: The variation of the peak signal amplitude with its angle relative to the plane perpendicular to the shower axis at 1 km (left). The angular asymmetry with angle at the same distance from the shower axis (right).

5.4.4 Angular dependence

The angular dependence of the acoustic signal amplitude is studied as a function of the angle relative to the pancake plane. Fig. 5.18 shows the angular dependence of the signal amplitude at different energies. The small spread in angles is due to the coherence in the addition of the acoustic signal from different parts of the shower. The angular spread of the acoustic pancake is about 1° , after which the signal amplitude shows a drop in its amplitude. The highest signal amplitude is at $\theta = 0^\circ$ and it decreases with the angle, the signal amplitude decreases by $\simeq 80\%$ at $\theta = 1^\circ$ relative to its value at $\theta = 0^\circ$. It is clear that, from the signal amplitude spread, the acoustic energy from the shower is confined in a disc, with $\simeq 1^\circ$ width, perpendicular to the shower axis through the shower maximum.

The asymmetry of the acoustic signal amplitude as a function of its angle relative to the pancake plane is shown in Fig. 5.18 for different energies. The signal is more symmetric with small angles and it becomes asymmetric with increases angle. For angles greater than $\approx 0.1^\circ$, the asymmetry is negative.

The amplitude and frequency composition of the acoustic pressure signal are studied at different angles relative to the pancake plane, see Fig. 5.19. The signal amplitude, and therefore its energy, decreases with angle. The median frequency of the acoustic signal decreases with angle and the shape of the signal spectrum gets broader. Fig. 5.20 shows the median frequency of the acoustic signal at different angles relative to the pancake plane, at 1 km from the shower center, generated by a 10^{11} GeV neutrino. The median

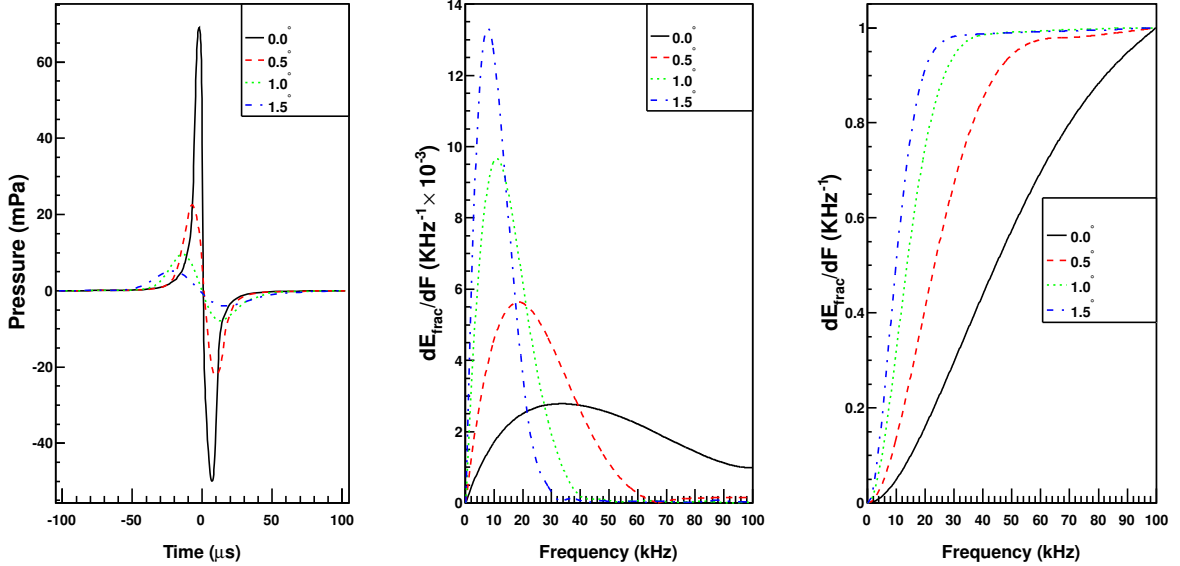


Figure 5.19: The peak pressure at 1 km, from 10^{11} GeV neutrino shower, as a function of the angle relative to the plane perpendicular to the shower axis (left), the corresponding frequency decomposition (middle) and their cumulative frequency spectra (right).

frequency decreases strongly with increasing angle.

5.5 Large acoustic neutrino detector simulation

UHE neutrinos have low fluxes and the acoustic energy from the cascade is concentrated in a thin disk perpendicular to the direction of the shower. Therefore, an array of sensors/hydrophones is required to produce an omnidirectional acoustic telescope capable of accurately reconstructing the shower location and direction. Based on the measured acoustic attenuation length in ice, the optimum design of such an array can be studied. To perform this study in ice, the propagation of the acoustic pressure signal is simulated. The pressure value at the source P_0 is calculated using Eq. 5.25, then the pressure amplitude is calculated using Eq. 5.23 by propagating the acoustic signal at different distances and different energies. Using the calculated P_0 at each energy, the acoustic signal pressure is calculated as a function of the distance from the source. Fig. 5.21 shows the propagation of the pressure amplitude at different energies above 10^9 GeV. The detection range at each energy can be seen where the pressure amplitude is above the 10 mPa trigger threshold (i.e. ambient noise). The signal-to-noise ratio increases with the neutrino energy which leads to a longer detection range. This means that the distance at which a signal can be reliably detected will increase with energy as shown in Fig. 5.22. The detection range is

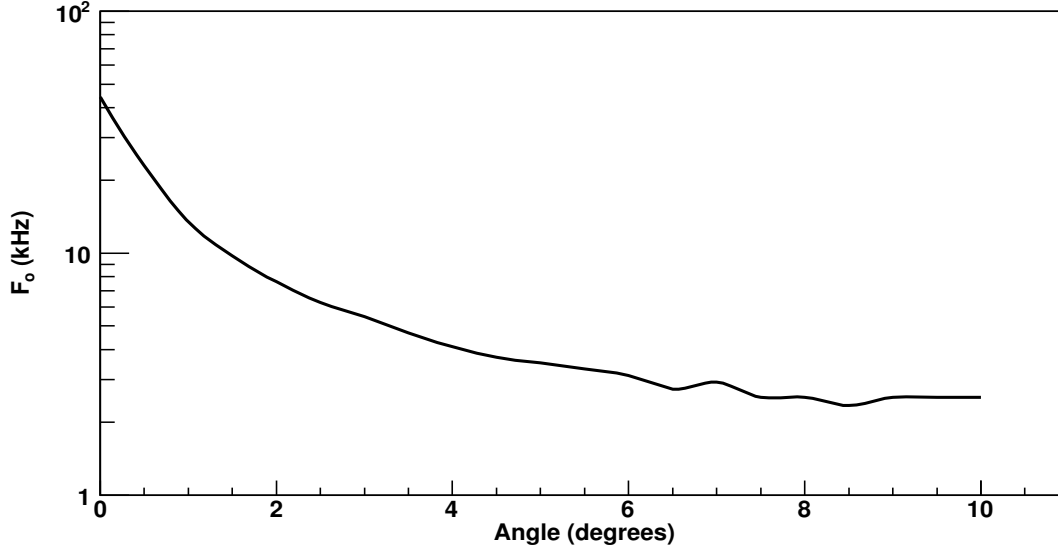


Figure 5.20: Median frequency for the acoustic signal versus angle at 1 km from the shower center. The shower is generated by 10^{11} GeV neutrino.

energy dependent and it gives an estimation of the spacing between sensors. Therefore, the detection range is used to predict the array size and spacing between sensors to build a neutrino telescope at a given neutrino energy threshold.

The simulated fiducial volume, over which the neutrino interaction vertices are simulated, is a cylinder with radius 5 km and height 2.5 km. The instrumented volume, $1 \times 1 \times 1 \text{ km}^3$ below 200 m (below the firn), is centered in the simulated volume and instrumented with a number of acoustic sensor modules (ASMs). Since the acoustic energy is confined on a very thin pancake orthogonal to the neutrino-induced shower axis, a symmetrical array of ASM with spacing larger than the pancake width degenerates geometrically and accepts only a few planes of acoustic pancakes. On the other hand, the random distribution of the ASM gives the greatest acceptance of acoustic pancakes. ASMs will be arranged randomly over the instrumented volume to avoid any geometrical effect due to the configuration of the ASMs. The simulation was done as follows:

- A number of ASMs are distributed randomly in a volume of 1 km^3 .
- 10^4 down-going neutrinos with random azimuth ($\phi = 0 - 2\pi$) and zenith ($\theta = 0, \pi$) interact in a fiducial volume, assuming the hadronic cascade has the same direction as the incident neutrino. This step is repeated for neutrino energies in half-integer powers of 10 from 10^9 GeV to 10^{15} GeV .
- The distance and the angle between each event and each ASM in the instrumented array is calculated. The peak pressure, P_{max} , as a function of neutrino energy is

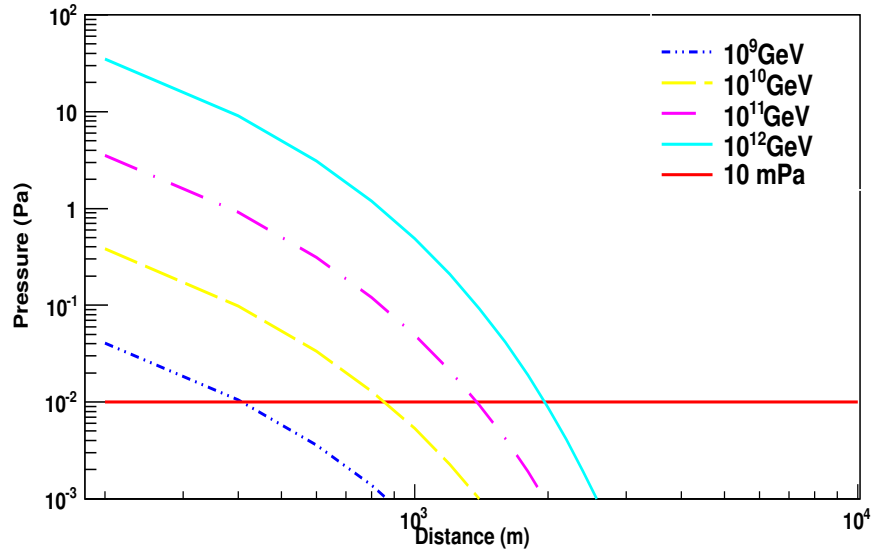


Figure 5.21: The attenuated acoustic signal amplitude versus distance at different energies, from 10^9 GeV to 10^{12} GeV from above to bottom. The 10 mPa trigger threshold is shown.

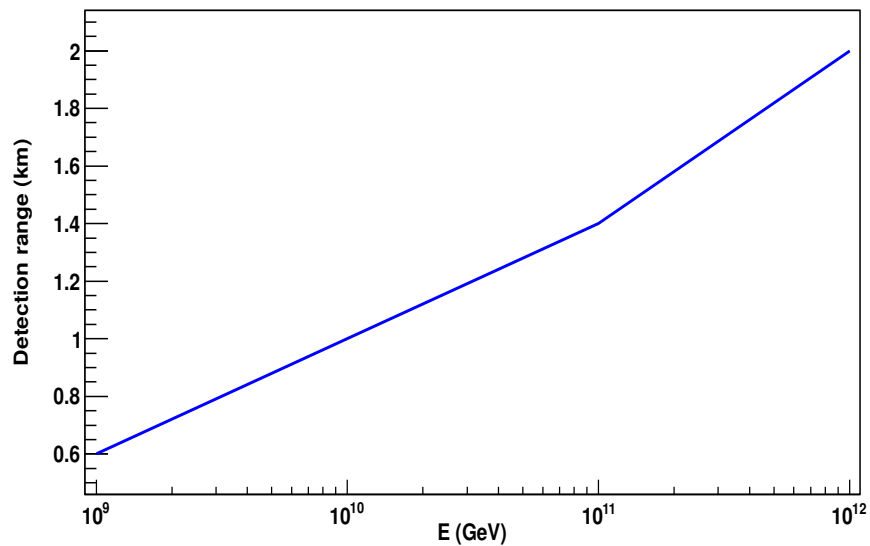


Figure 5.22: Detection range as a function of the neutrino energy.

calculated at each ASM, taking into account the angular spread of the pressure pulse.

- Any signal pressure greater than the noise level ($P_{th} = 10 \text{ mPa}$) is counted as a detected event.
- Different ASM densities are used to estimate the optimized number of ASMs required by the instrumented volume which gives a sufficient effective volume to build an acoustic array.

5.5.1 Effective volume and GZK fluxes

The effective volume V_{eff} for any given array is:

$$V_{eff} = \frac{N_{det}}{N_{gen}} V_{gen} \quad (5.27)$$

where V_{gen} is the volume over which events are generated, and N_{det} and N_{gen} are the number of events detected and generated, respectively. As seen in Eq. 5.27, V_{eff} is proportional to N_{det} for a given V_{gen} and N_{gen} . Figs. 5.23 and 5.24 show N_{det} and V_{eff} as a function of ASMs at different energies, respectively. Both V_{eff} and N_{det} increase with energy and the ASM density, especially below 10^{13} GeV. However, above 10^{13} GeV it can be seen that an increase in the instrumentation density above 200 ASM/km³ does not show a significant improvement in N_{det} and thus V_{eff} . Therefore, a density of 200 ASM/km³ is sufficient to build an acoustic detector. With high energy, a lower number of ASMs could be used because the acoustic interaction length is high enough to be detected by a distant ASM. The effective volume drops dramatically at low energies, therefore a very large acoustic array is needed to detect GZK neutrinos. A detector with a volume of 10^3 to 10^4 km³ could be sufficient to detect a few neutrinos per year.

The GZK neutrinos flux rate was calculated using the ESS GZK flux model [23]. The updated neutrino flux calculations for UHE cosmic rays and GZK neutrino production were done including CMB photons in the propagation calculation. However, the interactions with IR and optical photons were not included, these interactions could increase the yields of lower energy neutrinos. As reported in [142], one can use pure proton or mixed composition model, where the GZK flux does not change dramatically. GZK neutrinos are mostly produced by protons. In mixed composition models, the proton fraction is reduced, but one seems to get better fits to the UHE cosmic ray data if one uses a harder spectrum. The shape of the GZK spectrum may change, but the event rates for proton or mixed composition models will not differ by much.

The GZK neutrino event rate N_ν for a given detector could be predicted using the approach described in [135]. For an isotropic neutrino flux, the detector aperture is given by:

$$A(E) = \int d\Omega \sigma_{tot}(E) N(V_{eff}) P(E, \Omega) \quad (5.28)$$

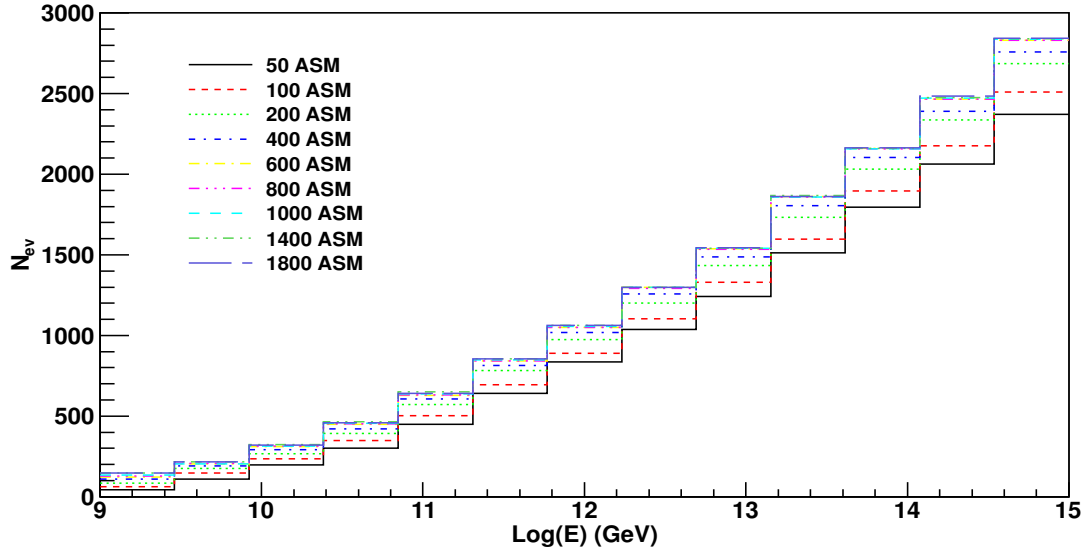


Figure 5.23: Detected events as a function of the ASM density for 1 km^3 instrumented volume, 10 mPa trigger threshold is used.

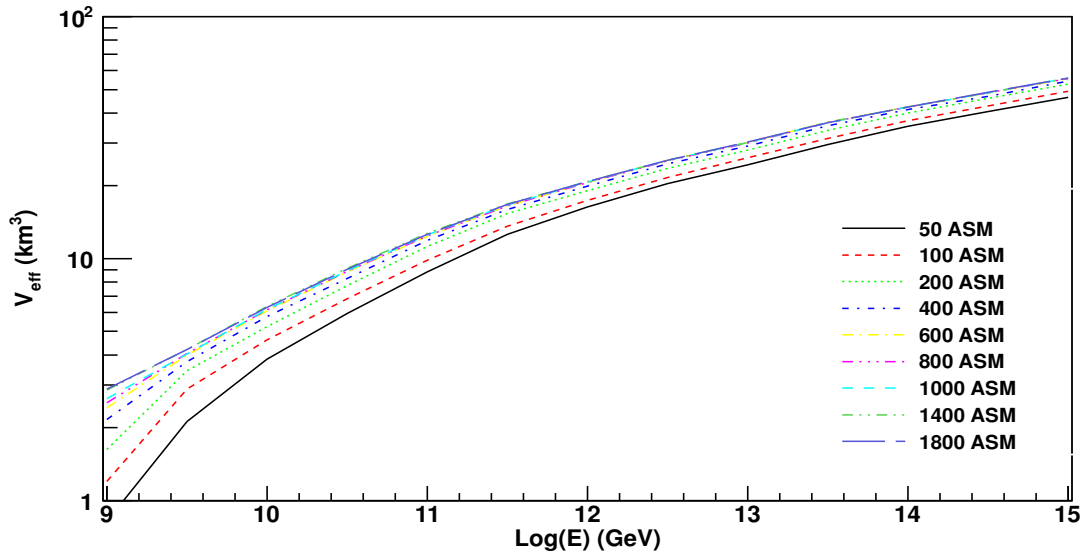


Figure 5.24: Effective volume as a function of the ASM density. The instrumented volume is 1 km^3 with $P_{th} = 10 \text{ mPa}$.

	Pure Proton	Mixed composition
N_{ν_e}	0.08	0.08
N_{ν_μ}	0.16	0.17
N_{Total}	0.24	0.25

Table 5.1: The expected total number of GZK neutrinos per 1 yr for 1 km³ detector using updated pure proton and mixed composition flux models [142].

where $N(V_{eff})$ is the total number of nucleons in the effective volume, $\sigma_{tot}(E)$ is the total (NC+CC) cross section for neutrino energy E which is given by Eq. 5.2 and $P(E, \Omega)$ is the interaction probability for a neutrino of energy E and direction Ω at the interaction point in the simulated fiducial volume. We assumed that all neutrinos coming from above the horizon ($\theta < 90^\circ$) can interact unperturbed to the fiducial volume, while the neutrinos from below ($\theta \geq 90^\circ$) are absorbed inside the earth before reaching the simulated volume. Therefore, the interaction probability is given by:

$$P(E, \Omega) = \begin{cases} 1 & \text{for } \theta < 90^\circ \\ 0 & \text{for } \theta \geq 90^\circ \end{cases} \quad (5.29)$$

and thus the detector aperture is given by:

$$A(E) = 2\pi\sigma_{tot}(E)N(V_{eff}) \quad (5.30)$$

Assuming the neutrino flux is constant in time, the number of detected neutrinos N_ν for any neutrino flavor for a given time T is given by:

$$N_\nu = T \int dE \phi(E) A(E) \quad (5.31)$$

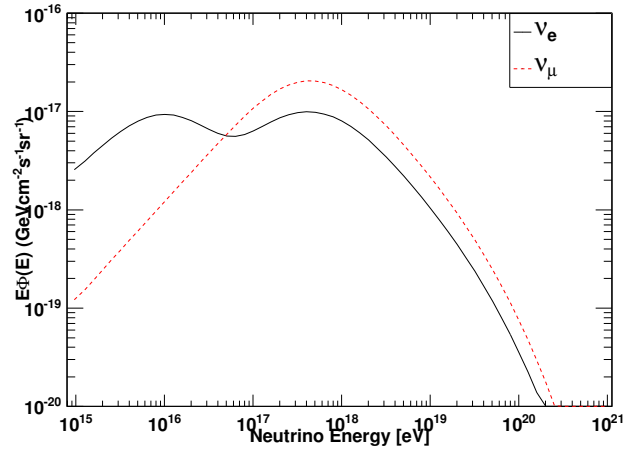
For a simulated volume of 1 km³ with 200 ASM randomly distributed, the expected neutrino event rate is calculated using $V_{eff}(E)$ and the updated ESS flux $\phi(E)$ with a cosmological constant³(or vacuum constant) $\Omega_\Lambda = 0.7$ [142] for both pure proton and mixed composition models which are shown in Fig. 5.25. The total number of observed neutrinos per 1 yr for pure proton and mixed composition models is shown in Table 5.1. The two models differ in their composition, but they give nearly the same total number of observed neutrinos ($N_{\nu_e} + N_{\nu_\mu}$) per 1 yr. With an ASM threshold of 10 mPa, ~ 0.25 GZK event per 1 yr is expected to be observed by the simulated detector.

5.6 Conclusion

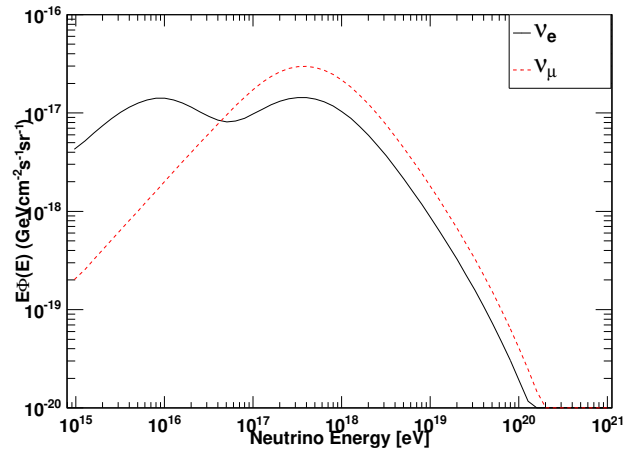
Hadronic showers, produced in ice as a result of the interaction of neutrinos, are simulated using a modified version of CORSIKA. Longitudinal and radial shower profiles are found

³Cosmological constant is a proposed form for dark energy and it is defined as a constant energy density filling space homogeneously [143]

5.6. Conclusion



(a)



(b)

Figure 5.25: The updated neutrino flux models. (a) pure proton composition model. (b) mixed composition model. From [142]

to be consistent with previous work done by the ACORNE group, specially near to the shower axis. The acoustic signal which is produced by neutrinos is simulated at different energies. The acoustic energy is found to be confined in a thin pancake, with a width of $\sim 1^\circ$, perpendicular to the shower axis. The acoustic signal is propagated in ice using the measured frequency independent attenuation length. The maximum peak amplitude P_{max} increases with neutrino energy, and it is proportional to it. The acoustic signal amplitude decreases with distance, with a constant median frequency. However, both median signal frequency and signal amplitude decrease with angle relative to the pancake plane. The effective volume of a given acoustic array and the optimal ASM density per km^3 are presented. The interaction range for EHE neutrinos is sufficient to build a large acoustic neutrino telescope in South Pole ice. A simulated volume of 1 km^3 with randomly distributed 200 ASM is expected to detect ~ 0.25 neutrino per 1 yr assuming a threshold trigger of 10 mPa.

Discussion and outlook

Over the last few decades, several dedicated neutrino telescopes have been built to detect UHE astrophysical neutrinos which are predicted from a variety of astrophysical objects. The main unanswered question concerning cosmic rays is: What is the origin and acceleration mechanism of the cosmic rays? Cosmogenic neutrinos are considered as ideal astrophysical messengers as they travel unperturbed from their source to Earth, since they rarely interact with matter. Therefore they are expected to carry information about their source: hadronic astrophysical accelerators or interaction of charged cosmic rays with the CMB.

Since the EHE neutrino flux is predicted to be very low (about 1 per km² per year), the IceCube detector could detect only ~ 1 GZK event per year. A detector with an effective volume of the order of 100 km³ is needed to detect a few GZK events per year. Acoustic and radio methods can, in principle, be used to instrument a large hybrid neutrino telescope with a good sensitivity at a reasonable cost [144]. Several studies on the radio detection in ice have been done and are planned in the near future. The South Pole Acoustic Test Setup (SPATS) is the only acoustic activity to study the acoustic detection in ice so far.

From the previous analysis, SPATS was almost be able to determine or constrain the acoustic ice properties from in-situ measurements, namely the acoustic attenuation length, the sound speed, the ambient noise level as well as the rate of transient noise events. The transient data were used to extract a limit on UHE neutrino flux. The acoustic attenuation length was predicted to be about 9 km and dominated by scattering, which is dependent on the acoustic signal frequency as f^4 . In-situ measurements by SPATS showed that the attenuation length is about 300 m and does not show frequency dependence in the region 10-30 kHz.

In this work, a complementary analysis was performed to investigate the acoustic attenuation mechanism in ice (absorption or scattering); and to study the frequency and depth dependence of the acoustic attenuation length. These measurements were done using the multi-frequency data from the 2009/2010 season with the retrievable transmitter (pinger). Further analysis related to the sound speed frequency dependence and the ice fabric of the South Pole was done. The in-situ measured attenuation length was used to perform a detailed simulation of neutrino-induced cascades and the resulting acoustic signal in ice. Further simulations were done to investigate the feasibility of a large neutrino telescope in ice.

- **Attenuation mechanism**

The acoustic attenuation length analysis was done using same-level measurements at depths of 250 m and 320 m. This analysis showed that the acoustic attenuation

length is not frequency dependent within the frequency range 30-45 kHz and its value is consistent with previous SPATS measurements ($\sim 300 \text{ m} \pm 20\%$). Therefore, it is concluded that the attenuation is dominated by absorption and not scattering. The depth dependent study did not show any strong depth dependence for the acoustic attenuation length.

- **Sound speed**

Same-level data, at 250 m and 320 m, was used to estimate the sound speed and to study sound speed frequency dependence in ice. The sound speed was found, within better than 1% accuracy, to be 3900 m/s, consistent with the previous measurements by SPATS. The measurements did not show any frequency or depth dependence below 200 m within the studied region (30-60 kHz). On the other hand, below the firn the sound speed is constant and therefore the refraction is not a challenge and the acoustic sources can be reconstructed. Therefore, South Pole ice is considered as a suitable medium for an acoustic neutrino telescope.

- **Ice fabric**

A measurement of the sound speed in a polycrystalline ice can yield an average orientation for the ice crystals and thus the ice fabric [121]. The sound speed measurements over the diagonal path could give an estimate of the c-axis orientation distribution (ice fabric) for different sectors of ice. The sound speed did not show any noticeable angular or directional dependence. Thus the acoustic pressure pulse is expected to propagate homogeneously and isotropically in the South Pole ice and the grain orientation is seen to be random. Therefore, the pressure waves from an interacting particle in ice can move homogeneously in the bulk ice. This gives a suitable and quiet medium to build a large detector using the acoustic technique.

- **Acoustic signal simulation**

The interaction of UHE neutrinos was simulated using a modified version of CORSIKA-IW. The generated hadronic cascade deposits its energy and causes local heating of the medium, which is converted into acoustic energy. This energy produces a pressure pulse in the medium. Since the acoustic energy is confined in a thin pancake orthogonal to the shower axis and the hadronic shower retains the incident neutrino direction, the detection of the pressure pulse will help to reconstruct the incident neutrino direction.

The deposited spatial energy from the hadronic shower was used to simulate the acoustic signal in ice. Hadronic shower profiles, longitudinal and radial, were studied and compared to previous work by the ACORNE group. The shower energy is deposited in a cylinder of radius $\sim 5 \text{ cm}$ and 10 m length. Most of this energy is confined in the inner core near to the shower axis.

The acoustic signal generated from the hadronic shower was propagated in ice using the in-situ measured attenuation length, $\sim 300 \text{ m}$. The attenuation length is not frequency dependent, as explained in this work. The acoustic signal amplitude was

found to decrease with distance from the source, and also with the angle relative to the pancake plane. The angular spread of the acoustic pancake was found to be $\sim 1^\circ$. The signal frequency is constant with distance but decreases with the angular deviation from the pancake plane. The maximum peak amplitude P_{max} is proportional to neutrino energy and scales with it. Also, the pressure at the source P_o is proportional to the neutrino energy.

The effective volume of a given acoustic array and the optimal ASM density per km^3 were presented. The neutrino interaction range at UHE is sufficient to build a large acoustic neutrino telescope in South Pole ice.

- **Acoustic ν -telescope**

The acoustic signal is attenuated due to the geometrical distance to the source and the medium in which it propagates. Using the measured attenuation length, the characteristics of a future, large-scale ν -telescope are determined. The effective volume for randomly distributed acoustic sensor modules (ASMs) showed that a density of $200 \text{ ASM}/\text{km}^3$ is sufficient for building a very large acoustic detector. The neutrino detection range at different energies was found to be sufficient to detect UHE neutrinos in ice. Due to the small V_{eff} relative to the detector volume and the low neutrino flux rate, a very large acoustic array is needed to detect a reasonable number of neutrinos per year.

- **Future outlook**

The drawbacks of the acoustic detection, namely the short attenuation length and the thin pancake perpendicular to the shower axis, could be compensated by using ASM with low self-noise able to measure signals at the limit of acoustic background noise, or using a very large array with a dense number of ASM. In the GZK energy range, radio detection can achieve a superior sensitivity at a reasonable cost compared to both acoustic and optical detection methods. The detection of GZK neutrinos with their low flux remains a challenge and needs a very large detector volume. A very large optical detector is expensive. The best configuration may be a large hybrid detector. A configuration of acoustic/radio arrays operating simultaneously is possible. Hybrid arrays offer the best hope of a convincing GZK neutrino detection, given the possibility of cross-calibrating the different techniques and the expected improvement in energy and direction reconstruction.

For a hybrid array, the signal time-of-flight and radio and acoustic radiation patterns can be used for event reconstruction. Comparing the geometrical arrangement of hit modules with the known radiation pattern (conical for radio, disk-like for acoustic) could be a valuable method to reject individual noise hits, reject background events, and fit for the cascade location and orientation. The plane of the acoustic pancake, a flat disk with a width of $\sim 1^\circ$, can be reconstructed from the array hit pattern. The radio Cherenkov cones have a known polarization orientation which could further enable background rejection and signal reconstruction.

Discrete Fourier Transform

A.1 Basic equations

Consider a set of N real numbers $X_j \in \mathbb{R}$ ($j = 0 \dots N - 1$). We define two new sets $\tilde{X}_j \in \mathbb{C}$ and $Y_j \in \mathbb{C}$ ($j = 0 \dots N - 1$) of N complex numbers each:

$$\tilde{X}_j := \sum_{k=0}^{N-1} X_k e^{-2\pi i \frac{jk}{N}} \quad (\text{A.1})$$

$$Y_j := \sum_{k=0}^{N-1} \tilde{X}_k e^{2\pi i \frac{jk}{N}} = \sum_{l=0}^{N-1} X_l \sum_{k=0}^{N-1} e^{2\pi i \frac{k(j-l)}{N}} = \sum_{l=0}^{N-1} X_l N \delta_{jl} = NX_j \quad (\text{A.2})$$

Since $X_j \in \mathbb{R}$ the following relation holds:

$$\tilde{X}_{N-k} = \tilde{X}_k^* \quad (\text{A.3})$$

so that there are only $\frac{N}{2} + 1$ independent values \tilde{X}_j (For simplicity we assume N to be even).

A.2 Continuous Fourier Transform

The continuous Fourier transform $\tilde{f} : \mathbb{R} \rightarrow \mathbb{C}, \omega \mapsto \tilde{f}(\omega)$ of a real function $f : \mathbb{R} \rightarrow \mathbb{R}, t \mapsto f(t)$ is defined as:

$$\tilde{f}(\omega) = \frac{1}{\sqrt{2\pi}} \int_{-\infty}^{\infty} dt f(t) e^{-i\omega t} \quad (\text{A.4})$$

with the inverse transform

$$f(t) = \frac{1}{\sqrt{2\pi}} \int_{-\infty}^{\infty} d\omega \tilde{f}(\omega) e^{i\omega t} \quad (\text{A.5})$$

Since $f(t) \in \mathbb{R}$ the following relation holds

$$\tilde{f}(-\omega) = \tilde{f}(\omega)^* \quad (\text{A.6})$$

and only non-negative frequencies ω have to be considered.

Energy conservation It is worth noticing that the total energy in the signal in the time and frequency domain are equal (Parseval's theorem):

$$\int_{-\infty}^{\infty} dt |f(t)|^2 = \int_{-\infty}^{\infty} d\omega |\tilde{f}(\omega)|^2 \quad (\text{A.7})$$

A.3 Discrete Fourier Transform

Now consider the case of a digitized signal with N samples U_j recorded at sampling intervals Δt . Then the total length of the waveform is $T = (N - 1)\Delta t$, and the Nyquist frequency is $f_{\max} = \frac{1}{2\Delta t}$. The frequency resolution is $\Delta f = \frac{f_{\max}}{N/2} = \frac{1}{N\Delta t}$.

In comparison with (A.4) we define the discrete Fourier transform (DFT) of U_j to be:

$$\tilde{U}_j := \Delta t \sum_{k=0}^{N-1} U_k e^{-2\pi i \frac{jk}{N}} \quad (\text{A.8})$$

Then the inverse transform is given by (compare to (A.5))

$$U_j := \Delta f \sum_{k=0}^{N-1} \tilde{U}_k e^{2\pi i \frac{jk}{N}} = \Delta f \Delta t N U_j = U_j \quad (\text{A.9})$$

where for the intermediate steps equations (A.2) and $\Delta t \Delta f = \frac{1}{N}$ were used.

The unit of the Fourier coefficients \tilde{U}_j is then (if U_j is measured in Volts): $[\tilde{U}_j] = \text{Vs} = \frac{\text{V}}{\text{Hz}}$.

One should notice that the Fourier coefficients \tilde{U}_j obviously depend on Δt and N so they are not a good quantity to compare different measurements or systems.

Energy conservation Notice that also in the discrete case energy is conserved (compare to (A.7)):

$$\Delta t \sum_{j=0}^{N-1} |U_j|^2 = \Delta f \sum_{j=0}^{N-1} |\tilde{U}_j|^2 \quad (\text{A.10})$$

A.4 Power Spectral Density

The energy E of the recorded signal is given by (A.10):

$$E = \Delta f \sum_{j=0}^{N-1} |\tilde{U}_j|^2 \quad (\text{A.11})$$

If $T = (N - 1)\Delta t$ is the length of the signal the average power P is given by

$$P = \frac{E}{T} = \frac{\Delta f}{(N - 1)\Delta t} \sum_{j=0}^{N-1} |\tilde{U}_j|^2 \approx \frac{2\Delta f}{(N - 1)\Delta t} \sum_{j=0}^{N/2} |\tilde{U}_j|^2 \quad (\text{A.12})$$

where in the last step (A.3) was used. For a continuous signal (e.g. noise) P is independent of the length T of the recording.

So the power P_j in the j -th frequency bin of width Δf is

$$P_j = \frac{2\Delta f |\tilde{U}_j|^2}{(N - 1)\Delta t}, \quad (j = 0 \dots N/2) \quad (\text{A.13})$$

The power spectral density PSD_j is defined as the power per unit frequency, so

$$PSD_j = \frac{P_j}{\Delta f} = \frac{2|\tilde{U}_j|^2}{(N - 1)\Delta t}, \quad (j = 0 \dots N/2) \quad (\text{A.14})$$

which is independent of both the sampling rate Δt and the number of samples N (or equivalently Δf and N).

The unit of the power spectral density is (if U_j is measured in Volts) $[PSD_j] = \text{V}^2/\text{s} = \frac{\text{V}^2}{\text{Hz}}$.

Numerical calculation The FFTW algorithm which is e.g. used in ROOT calculates DFTs using (A.1). So when one gets values \tilde{X}_j from such a calculation the PSD must be calculated as

$$PSD_j = \frac{2|\Delta t \tilde{X}_j|^2}{(N - 1)\Delta t} = \frac{2\Delta t |\tilde{X}_j|^2}{(N - 1)} \left(= \frac{|\tilde{X}_j|^2}{f_{\max}(N - 1)} \right) \quad (\text{A.15})$$

Be careful: There are several programs out there which do not calculate $\tilde{X}_j = \sum_{k=0}^{N-1} X_k e^{-2\pi i \frac{jk}{N}}$ but $\tilde{X}_j = \frac{1}{\sqrt{N}} \sum_{k=0}^{N-1} X_k e^{-2\pi i \frac{jk}{N}}$ or use even other normalization factors, so that (A.15) has to be adapted accordingly.

A.5 Relation between PSD and Signal RMS

If the mean value μ of a signal is zero:

$$\mu = \frac{1}{N} \sum_{j=0}^{N-1} U_j = 0 \quad (\text{A.16})$$

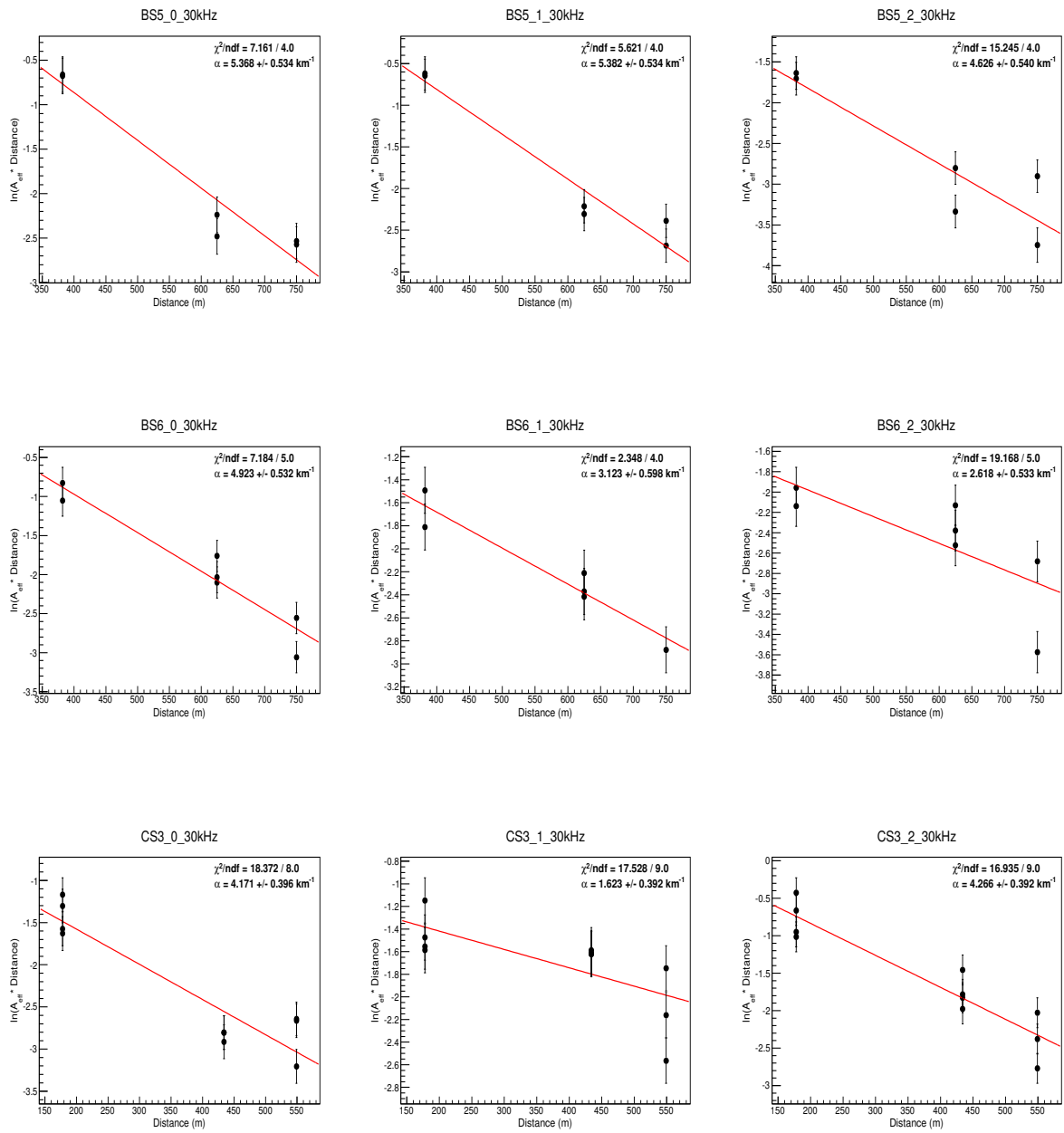
then the standard deviation σ^2 of the signal is given by

$$\begin{aligned}
 \sigma^2 &= \frac{1}{N} \sum_{j=0}^{N-1} |U_j|^2 = \frac{1}{N} \frac{\Delta f}{\Delta t} \sum_{j=0}^{N-1} |\tilde{U}_j|^2 \approx \frac{2}{N} \frac{\Delta f}{\Delta t} \sum_{j=0}^{N/2} |\tilde{U}_j|^2 \\
 &= \frac{2}{N} \frac{\Delta f}{\Delta t} \sum_{j=0}^{N/2} \frac{(N-1)\Delta t PSD_j}{2} = \frac{N-1}{N} \Delta f \sum_{j=0}^{N/2} PSD_j \\
 &\approx \Delta f \sum_{j=0}^{N/2} PSD_j
 \end{aligned}$$

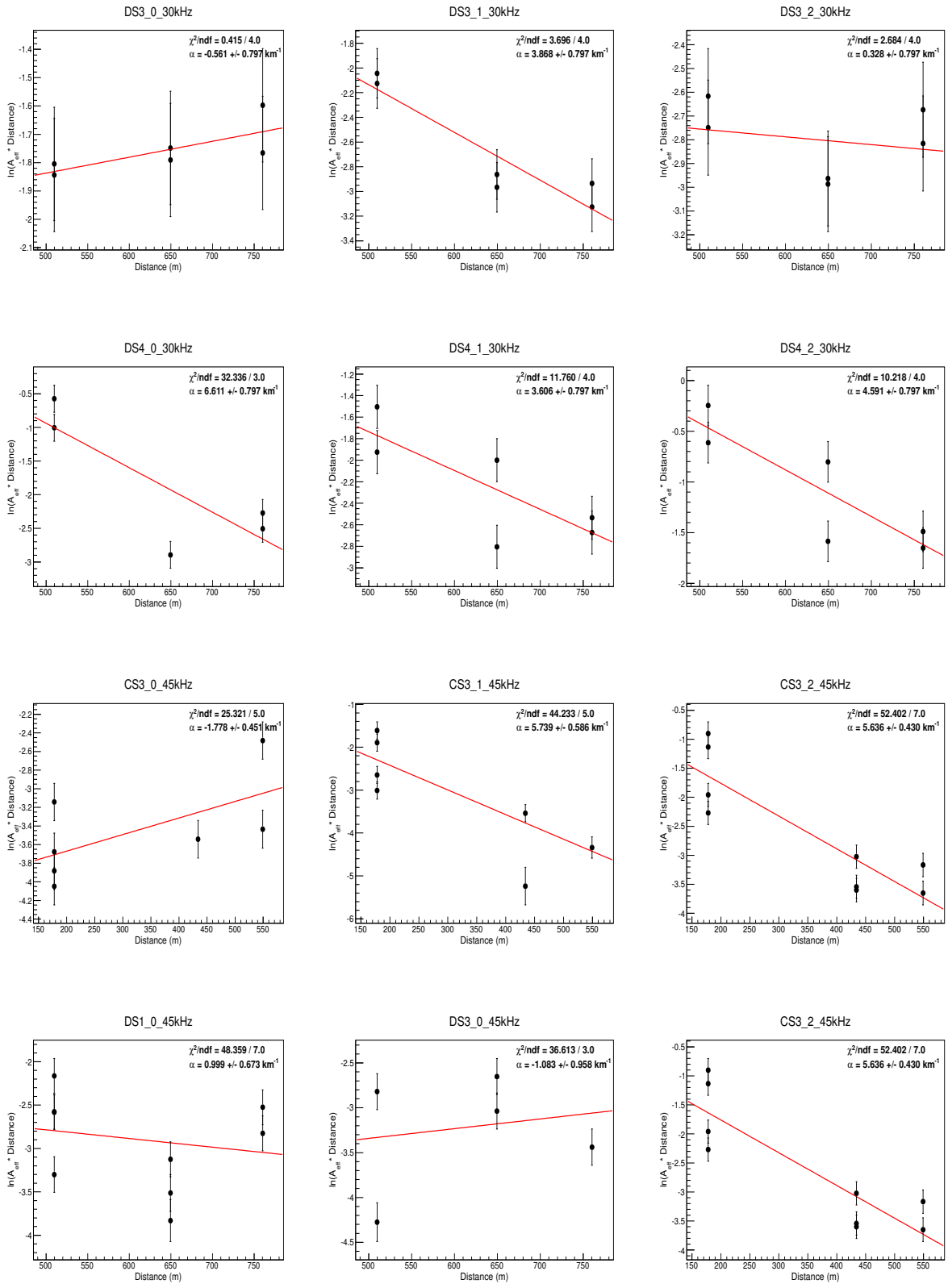
So the integral over the power spectral density is equal to the standard deviation (RMS) in the time domain.

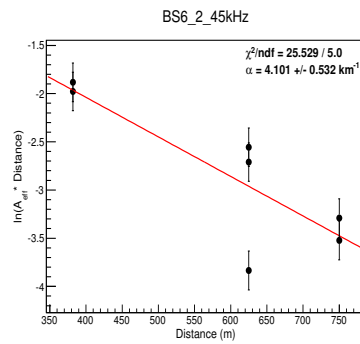
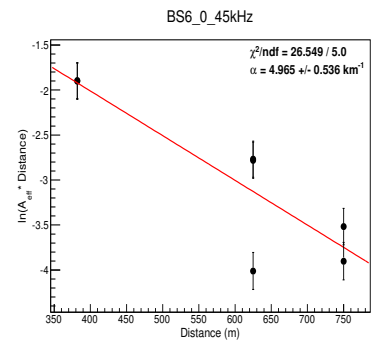
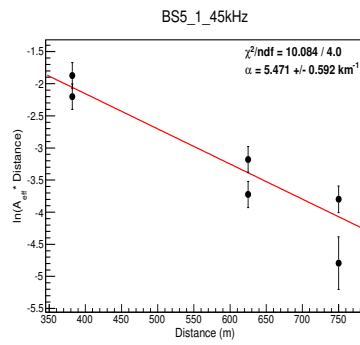
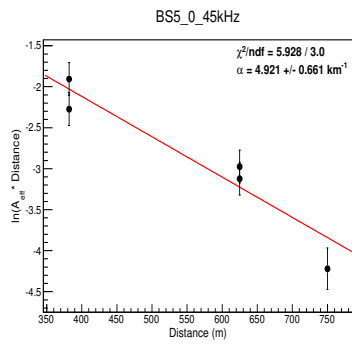
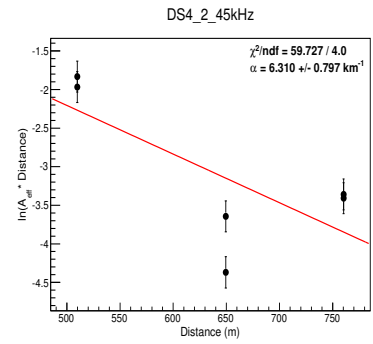
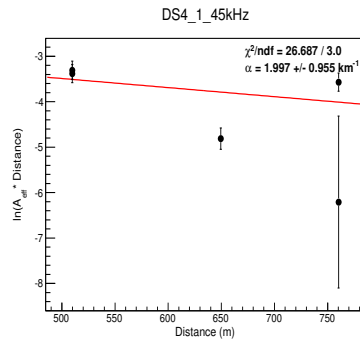
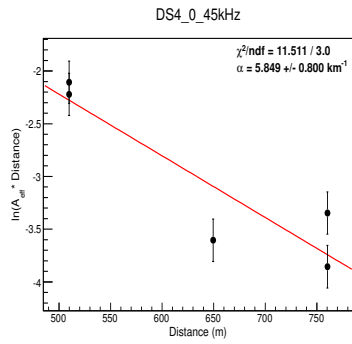
APPENDIX B

Attenuation fit



Appendix B. Attenuation fit

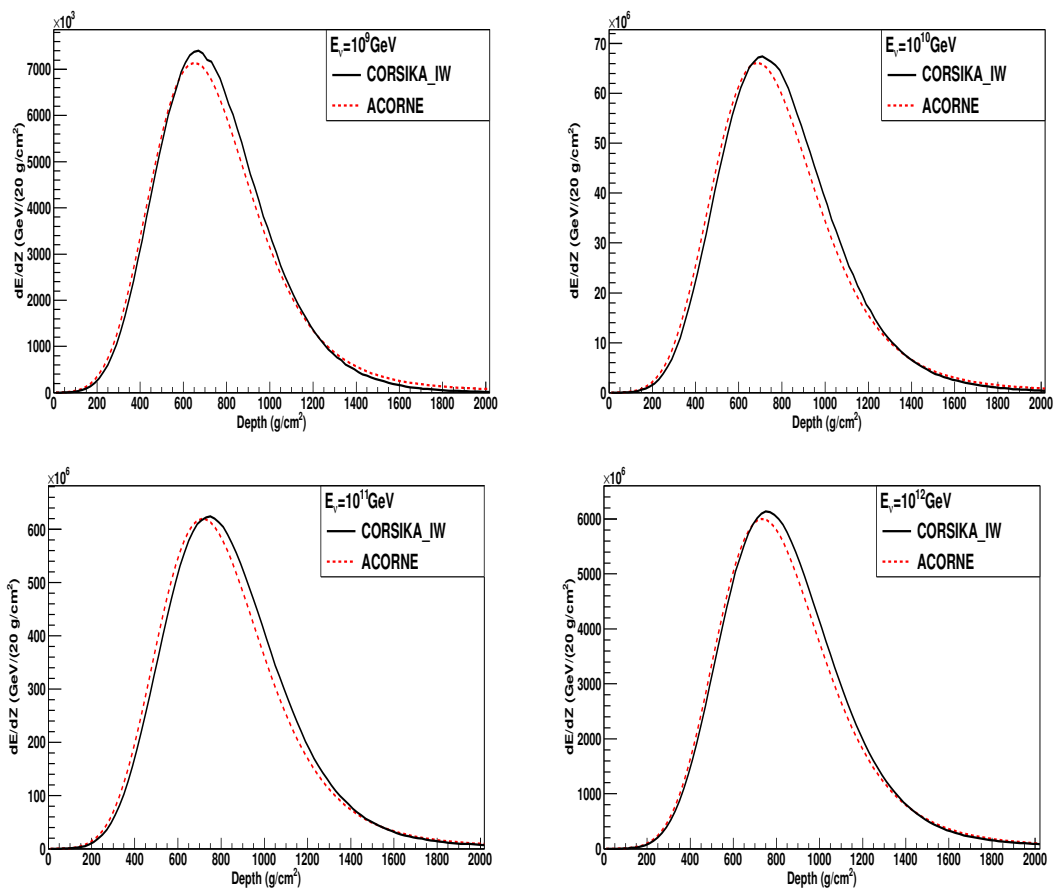




APPENDIX C

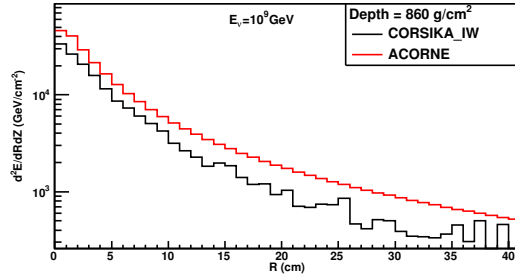
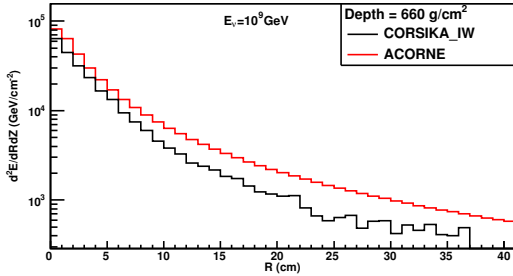
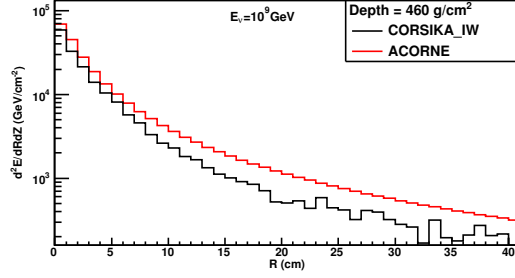
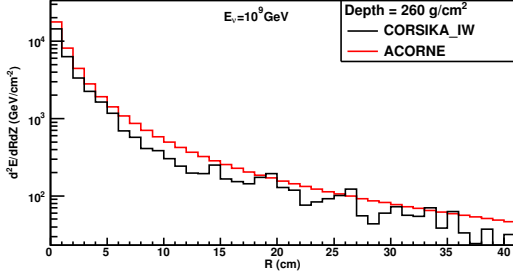
Simulation results

C.1 Longitudinal profile

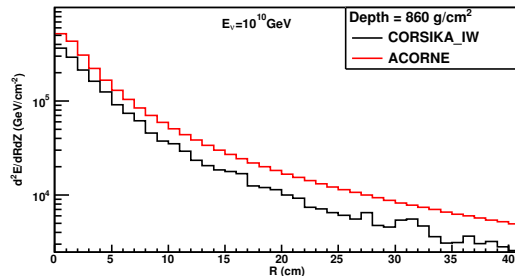
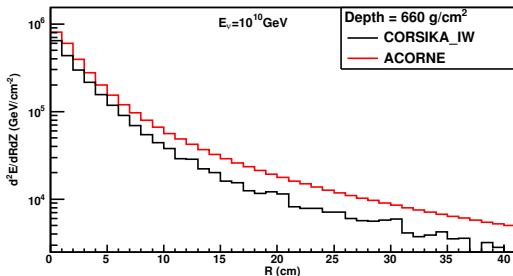
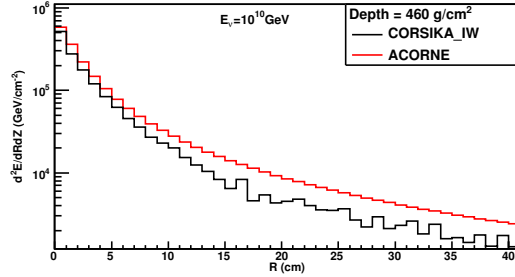
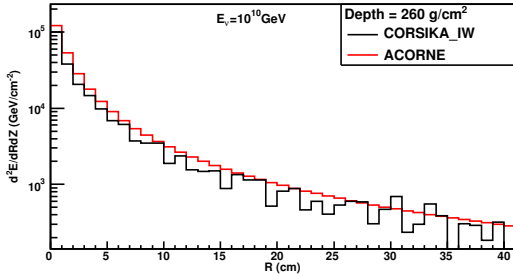


C.2 Radial profile

$$E_\nu = 10^9 \text{ GeV}$$

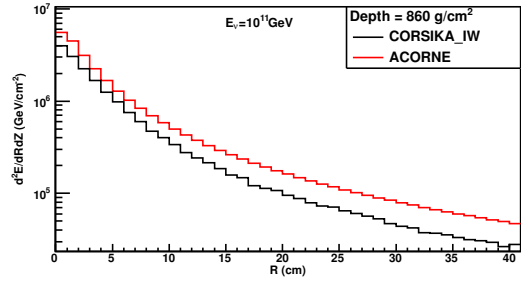
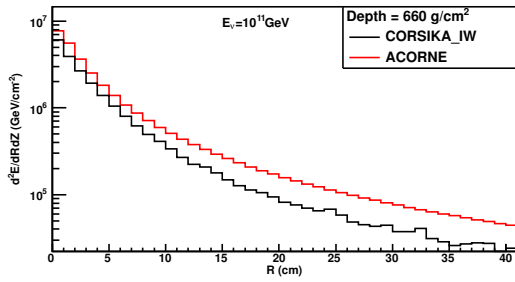
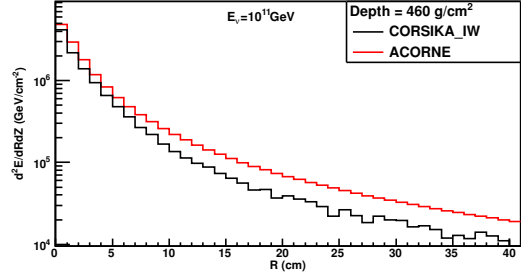
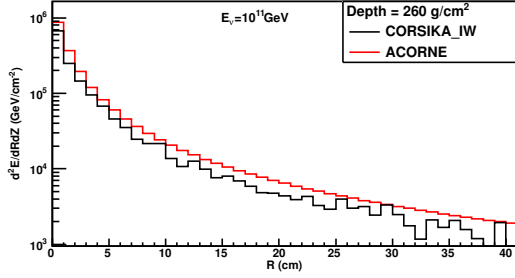


$$E_\nu = 10^{10} \text{ GeV}$$

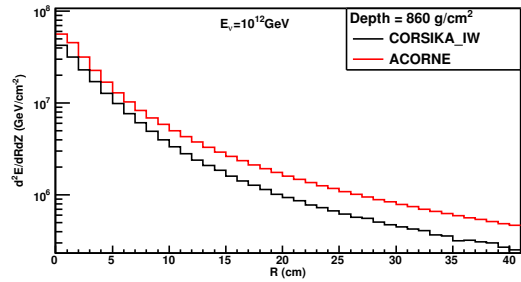
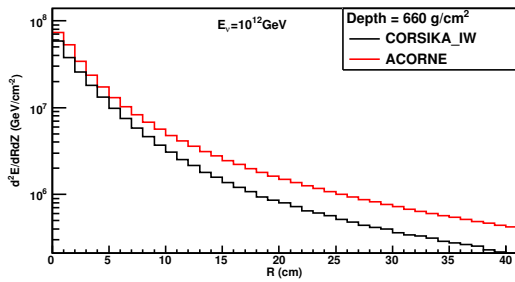
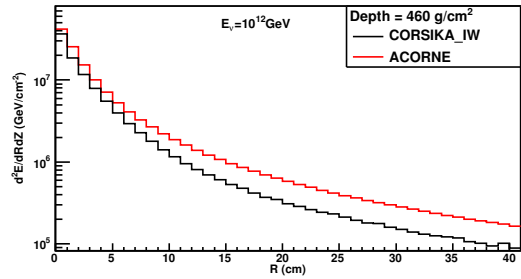
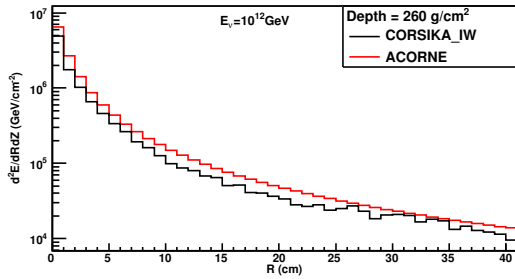


C.2. Radial profile

$$E_\nu = 10^{11} \text{ GeV}$$



$$E_\nu = 10^{12} \text{ GeV}$$



Bibliography

- [1] C. L. J. Cowan, F. Reines, F. B. Harrison, H. W. Kruse, and A. D. McGuire, “Detection of the Free Neutrino: A Confirmation,” *Science*, vol. 124, p. 103, 1956.
- [2] R. Gandhi, C. Quigg, M. H. Reno, and I. Sarcevic, “Neutrino interactions at ultrahigh-energies,” *Phys. Rev.*, vol. D58, p. 093009, 1998.
- [3] P. Price, “Comparison of optical, radio, and acoustical detectors for ultrahigh-energy neutrinos,” *Astroparticle Physics*, vol. 5, no. 1, pp. 43 – 52, 1996.
- [4] P. B. Price, “Attenuation of acoustic waves in glacial ice and salt domes,” *Journal of Geophysical Research*, vol. 164, pp. 267–278, 2006.
- [5] A. M. Hillas, “The Origin of Ultra-High-Energy Cosmic Rays,” *Ann. Rev. Astron. Astrophys.*, vol. 22, pp. 425–444, 1984.
- [6] R. Bionta *et al.*, “Observation of a neutrino burst in coincidence with supernova 1987a in the large magellanic cloud,” *Phys. Rev. Lett.*, vol. 58, pp. 1494–1496, Apr 1987.
- [7] S. Swordy, “Astroparticle physics at chicago.” <http://astroparticle.uchicago.edu>, 1997.
- [8] T. K. Gaisser, *Cosmic Rays and Particle Physics*. Cambridge, 1990.
- [9] K. Greisen, “End to the cosmic ray spectrum?,” *Phys. Rev. Lett.*, vol. 16, pp. 748–750, 1966.
- [10] G. T. Zatsepin and V. A. Kuzmin, “Upper limit of the spectrum of cosmic rays,” *JETP Lett.*, vol. 4, pp. 78–80, 1966.
- [11] J. Abraham *et al.*, “Measurement of the energy spectrum of cosmic rays above 10^{18} eV using the Pierre Auger Observatory,” *Physics Letters B*, vol. 685, no. 4-5, pp. 239 – 246, 2010.
- [12] R. Abbasi *et al.*, “Measurement of the flux of ultra high energy cosmic rays by the stereo technique,” *Astroparticle Physics*, vol. 32, no. 1, pp. 53 – 60, 2009.
- [13] E. Fermi, “On the Origin of the Cosmic Radiation,” *Phys. Rev.*, vol. 75, pp. 1169–1174, 1949.
- [14] E. Fermi, “Galactic Magnetic Fields and the Origin of Cosmic Radiation,” *Astrophysical Journal*, vol. 119, pp. 1–6, 1954.

- [15] B. Baret and V. V. Elewyck, “High-energy neutrino astronomy: detection methods and first achievements,” *Reports on Progress in Physics*, vol. 74, no. 4, pp. 1–35, 2011.
- [16] K. Lai *et al.*, “Determination of the neutrino flavor ratio at the astrophysical source,” *Phys. Rev. D*, vol. 80, p. 103005, 2009.
- [17] D. V. Ahluwalia, “Ambiguity in source flux of cosmic and astrophysical neutrinos: Effects of bi-maximal mixing and quantum-gravity induced decoherence,” *Mod. Phys. Lett.*, vol. A16, pp. 917–926, 2001.
- [18] A. A. Penzias and R. W. Wilson, “A Measurement of Excess Antenna Temperature at 4080 Mc/s,” *Astrophysical Journal*, vol. 142, pp. 419–421, 1965.
- [19] D. Hooper, S. Sarkar, and A. M. Taylor, “The intergalactic propagation of ultra-high energy cosmic ray nuclei,” *Astropart. Phys.*, vol. 27, pp. 199–212, 2007.
- [20] F. W. Stecker, “Photodisintegration of ultrahigh-energy cosmic rays by the universal radiation field,” *Phys. Rev.*, vol. 180, pp. 1264–1266, 1969.
- [21] J. Cronin, “Summary of the workshop,” *Nuclear Physics B - Proceedings Supplements*, vol. 28, no. 2, pp. 213 – 225, 1992.
- [22] R. Aloisio, V. Berezhinsky, and A. Gazizov, “Ultra High Energy Cosmic Rays: The disappointing model,” *Astropart. Phys.*, vol. 34, pp. 620–626, 2011.
- [23] R. Engel, D. Seckel, and T. Stanev, “Neutrinos from propagation of ultra-high energy protons,” *Phys. Rev.*, vol. D64, p. 093010, 2001.
- [24] E. Waxman and J. Bahcall, “High Energy Neutrinos from Astrophysical Sources: An Upper Bound,” *Phys. Rev.*, vol. D59, p. 023002, 1999.
- [25] J. K. Becker, “High-energy neutrinos in the context of multimessenger physics,” *Phys. Rept.*, vol. 458, pp. 173–246, 2008.
- [26] S. D. Wick, T. W. Kephart, T. J. Weiler, and P. L. Biermann, “Signatures for a cosmic flux of magnetic monopoles,” *Astropart. Phys.*, vol. 18, pp. 663–687, 2003.
- [27] T. J. Weiler, “Cosmic ray neutrino annihilation on relic neutrinos revisited: A mechanism for generating air showers above the Greisen-Zatsepin-Kuzmin cut-off,” *Astropart. Phys.*, vol. 11, pp. 303–316, 1999.
- [28] K. Mannheim, R. J. Protheroe, and J. P. Rachen, “On the cosmic ray bound for models of extragalactic neutrino production,” *Phys. Rev.*, vol. D63, p. 023003, 2001.
- [29] D. Hooper, A. Taylor, and S. Sarkar, “The impact of heavy nuclei on the cosmogenic neutrino flux,” *Astropart. Phys.*, vol. 23, no. 1, pp. 11 – 17, 2005.

- [30] A. Achterberg *et al.*, “Multi-year search for a diffuse flux of muon neutrinos with AMANDA-II,” *Phys. Rev.*, vol. D76, p. 042008, 2007.
- [31] K. J. Palladino, *The ANITA-I Limit on Gamma Ray Burst Neutrinos*. PhD thesis, Ohio State University, 2009.
- [32] L. S. Sparke *et al.*, *Galaxies in the universe*. Cambridge, 2000.
- [33] T. Stanev, *High energy cosmic rays*. Springer, 2004.
- [34] J. Abraham *et al.*, “Correlation of the highest-energy cosmic rays with nearby extragalactic objects,” *Science*, vol. 318, no. 5852, pp. 938–943, 2007.
- [35] R. Antonucci, “Picture of a unified model of an active galactic nucleus.” Website:<http://web.physics.ucsb.edu/ski/skipicture-1.html>, 2012.
- [36] A. Dar, “The GRB/XRF-SN Association,” *ArXiv Astrophysics e-prints*, 2004.
- [37] E. Nakar, “Short-Hard Gamma-Ray Bursts,” *Phys.Rept.*, vol. 442, pp. 166–236, 2007.
- [38] E. Waxman, “GRB after-glow: Supporting the cosmological fireball model, constraining parameters, and making predictions,” *Astrophys. J.*, vol. 485, p. L5, 1997.
- [39] S. Dado and A. Dar, “The cannonball model of long GRBs-overview,” *AIP Conf.Proc.*, vol. 1111, pp. 333–343, 2009.
- [40] P. Mészáros, “Gamma-ray bursts: accumulating afterglow implications, progenitor clues, and prospects,” *Science*, vol. 291, no. 5501, pp. 79–84, 2001.
- [41] E. Waxman, “Extra galactic sources of high energy neutrinos,” *Phys. Scripta*, vol. T121, pp. 147–152, 2005.
- [42] R. Abbasi *et al.*, “An absence of neutrinos associated with cosmic-ray acceleration in γ -ray bursts,” *Nature*, vol. 484, no. 7394, pp. 351–354, 2012.
- [43] R. Abbasi *et al.*, “First search for extremely high energy cosmogenic neutrinos with the IceCube neutrino observatory,” *Phys. Rev. D*, vol. 82, p. 072003, 2010.
- [44] J. Abraham *et al.*, “Limit on the diffuse flux of ultrahigh energy tau neutrinos with the surface detector of the Pierre Auger Observatory,” *Phys. Rev. D*, vol. 79, p. 102001, 2009.
- [45] R. Abbasi *et al.*, “An upper limit on the electron-neutrino flux from the HiRes detector,” *The Astrophysical Journal*, vol. 684, no. 2, p. 790, 2008.

- [46] N. Kurahashi, J. Vandenbroucke, and G. Gratta, “Search for acoustic signals from ultrahigh energy neutrinos in 1500 km³ of sea water,” *Phys. Rev. D*, vol. 82, p. 073006, 2010.
- [47] S. Bevan, “Data analysis techniques for UHE acoustic astronomy,” *Nucl. Instrum. Meth.*, vol. A604, pp. S143–S148, 2009.
- [48] R. Abbasi *et al.*, “Background studies for acoustic neutrino detection at the South Pole,” *Astropart. Phys.*, vol. 35, pp. 312–324, 2012.
- [49] I. Kravchenko *et al.*, “Rice limits on the diffuse ultrahigh energy neutrino flux,” *Phys. Rev. D*, vol. 73, p. 082002, 2006.
- [50] P. Gorham *et al.*, “Observational Constraints on the Ultra-high Energy Cosmic Neutrino Flux from the Second Flight of the ANITA Experiment,” *Phys. Rev.*, vol. D82, p. 022004, 2010.
- [51] N. G. Lehtinen, P. W. Gorham, A. R. Jacobson, and R. A. Roussel-Dupré, “Forte satellite constraints on ultrahigh energy cosmic particle fluxes,” *Phys. Rev. D*, vol. 69, p. 013008, Jan 2004.
- [52] P. W. Gorham *et al.*, “Experimental limit on the cosmic diffuse ultrahigh energy neutrino flux,” *Phys. Rev. Lett.*, vol. 93, p. 041101, 2004.
- [53] R. Fiore *et al.*, “Ultra-high energy neutrino nucleon interactions,” *Phys. Rev.*, vol. D68, p. 093010, 2003.
- [54] R. Gandhi, C. Quigg, M. H. Reno, and I. Sarcevic, “Ultrahigh-energy neutrino interactions,” *Astroparticle Physics*, vol. 5, no. 2, pp. 81 – 110, 1996.
- [55] S. L. Glashow, “Resonant Scattering of Antineutrinos,” *Phys. Rev.*, vol. 118, pp. 316–317, 1960.
- [56] J. Kwiecinski, A. D. Martin, and A. M. Stasto, “Penetration of the earth by ultrahigh energy neutrinos predicted by low x QCD,” *Phys. Rev.*, vol. D59, p. 093002, 1999.
- [57] C. Amsler *et al.*, “Passage of particles through matter,” *Phys. Lett.*, vol. B667, 2008.
- [58] J. Alvarez-Muniz and E. Zas, “EeV Hadronic Showers in Ice: The LPM effect,” 1999. arXiv 9906.347.
- [59] L. D. Landau and I. Pomeranchuk, “Electron cascade process at very high-energies,” *Dokl. Akad. Nauk Ser. Fiz.*, vol. 92, pp. 735–738, 1953.
- [60] A. B. Migdal, “Bremsstrahlung and pair production in condensed media at high-energies,” *Phys. Rev.*, vol. 103, pp. 1811–1820, 1956.

- [61] J. Alvarez-Muniz and E. Zas, “The LPM effect for EeV hadronic showers in ice: implications for radio detection of neutrinos,” *Phys. Lett.*, vol. B434, p. 396, 1998.
- [62] M. A. Markov, “On high energy neutrino physics,” *Proceedings of the 1960 Annual International Conference on High-Energy Physics*, p. 578, 1960.
- [63] F. Halzen and S. R. Klein, “IceCube: An Instrument for Neutrino Astronomy,” *Rev.Sci.Instrum.*, vol. 81, p. 081101, 2010.
- [64] A. Haungs, “Radio Detection of Particles from the Cosmos,” *Nucl.Instrum.Meth.*, vol. A604, pp. S236–S243, 2009.
- [65] J. Alvarez-Muñiz, E. Marqués, R. A. Vázquez, and E. Zas, “Coherent radio pulses from showers in different media: A unified parametrization,” *Phys. Rev. D*, vol. 74, p. 023007, Jul 2006.
- [66] G. A. Askarian, “Excess negative charge of an electron-photon shower and its coherent radio emission,” *Sov. Phys.*, vol. JETP14, p. 441, 1962.
- [67] G. A. Askarian *Atomnaya Energiya*, vol. 3, p. 152, 1957.
- [68] V. S. Berezinskii and G. T. Zatsepin, “Possible experiments with very high energy cosmic neutrinos: the DUMAND project,” *Sov. Phys. Usp.*, vol. 20, no. 5, pp. 361–380, 1977.
- [69] R. J. Wilkes *et al.*, “DUMAND-II progress report,” Presented at Conf. on Intersection between Particle and Nuclear physics, Tucson, AZ, May 24–29, 1991.
- [70] V. Aynutdinov *et al.*, “The BAIKAL neutrino experiment: Physics results and perspectives,” *Nucl. Instrum. Meth.*, vol. A602, pp. 14–20, 2009.
- [71] J. A. Aguilar *et al.*, “First results of the instrumentation line for the deep-sea ANTARES neutrino telescope,” *Astropart. Phys.*, vol. 26, pp. 314–324, 2006.
- [72] R. Arnold *et al.*, “Technical design and performance of the NEMO-3 detector,” *Nucl. Instrum. Meth.*, vol. A536, pp. 79–122, 2005.
- [73] P. Sapienza, “The NEMO project: Achievements and perspectives,” *J. Phys. Conf. Ser.*, vol. 120, p. 062010, 2008.
- [74] P. A. Rapidis, “The NESTOR underwater neutrino telescope project,” *Nucl. Instrum. Meth.*, vol. A602, pp. 54–57, 2009.
- [75] M. Ackermann *et al.*, “Search for Ultra High-Energy Neutrinos with AMANDA-II,” *Astrophys. J.*, vol. 675, p. 1014, 2008.
- [76] A. Achterberg *et al.*, “First year performance of the IceCube neutrino telescope,” *Astropart. Phys.*, vol. 26, pp. 155–173, 2006.

- [77] P. W. Gorham *et al.*, “Initial results from the ANITA 2006-2007 balloon flight,” *J. Phys. Conf. Ser.*, vol. 136, p. 022052, 2008.
- [78] R. Nichol *et al.*, “Radio detection of high-energy particles with the ANITA experiment,” *Nucl. Instrum. Meth.*, vol. 626-627, Supplement, pp. S30–S35, 2011.
- [79] I. Kravchenko, “Limits on the Ultra-High Energy Electron Neutrino Flux from the RICE Experiment,” *Astropart. Phys.*, vol. 20, p. 195, 2003.
- [80] J. Abraham *et al.*, “Upper limit on the diffuse flux of UHE tau neutrinos from the Pierre Auger Observatory,” *Phys. Rev. Lett.*, vol. 100, p. 211101, 2008.
- [81] I. Kravchenko *et al.*, “Updated Results from the RICE Experiment and Future Prospects for Ultra-High Energy Neutrino Detection at the South Pole,” *Phys.Rev.*, vol. D85, p. 062004, 2012.
- [82] S. W. Barwick *et al.*, “ARIANNA: A New Concept for UHE Neutrino Detection,” *J. Phys. Conf. Ser.*, vol. 60, pp. 276–283, 2007.
- [83] H. Landsman *et al.*, “AURA—A radio frequency extension to IceCube,” *Nucl. Instrum. Meth.*, vol. 604, no. 1-2, pp. S70–S75, 2009.
- [84] P. Allison *et al.*, “IceRay: An IceCube-centered Radio-Cherenkov GZK Neutrino Detector,” *Nucl. Instrum. Meth.*, vol. A604, pp. S64–S69, 2009.
- [85] P. W. Gorham *et al.*, “Experimental limit on the cosmic diffuse ultrahigh energy neutrino flux,” *Phys. Rev. Lett.*, vol. 93, p. 041101, Jul 2004.
- [86] P. W. Gorham, K. M. Liewer, R. Milincic, C. J. Naudet, D. Saltzberg, and D. Williams, “Status of Goldstone Lunar Ultra-High Energy Neutrino Experiment (GLUE),” *Part. Astrophys. Instrum.*, vol. 4858, no. 1, pp. 171–178, 2003.
- [87] H. J. A. Rottgering *et al.*, “LOFAR: Opening up a new window on the Universe,” in *Proceedings of Conference on Cosmology, Galaxy Formation and Astro-Particle Physics on the Pathway to the SKA*, 2006. astro-ph/0610596.
- [88] M. Chiba *et al.*, “Measurement of attenuation length for radio wave in natural rock salt samples concerning ultra high energy neutrino detection,” *Int. J. Mod. Phys.*, vol. A21S1, pp. 25–29, 2006.
- [89] R. Milincic, “The status of SalSA detector,” *AIP Conf. Proc.*, vol. 928, pp. 77–82, 2007.
- [90] D. Saltzberg *et al.*, “Introduction to the SalSA, a salt dome shower array as a GZK neutrino observatory,” *Int. J. Mod. Phys.*, vol. A21S1, pp. 252–253, 2006.

- [91] J. Alvarez-Muniz, E. Marques, R. A. Vazquez, and E. Zas, “Simulations of radio emission from electromagnetic showers in dense media,” *Int. J. Mod. Phys.*, vol. A21S1, pp. 55–59, 2006.
- [92] S. Danaher, “First data from ACoRNE and signal processing techniques,” *J. Phys. Conf. Ser.*, vol. 81, p. 012011, 2007.
- [93] J. Aguilar *et al.*, “Amadeus—the acoustic neutrino detection test system of the antares deep-sea neutrino telescope,” *Nucl. Instrum. Meth.*, vol. 626-627, pp. 128–143, 2011.
- [94] V. Aynutdinov *et al.*, “The BAIKAL neutrino experiment: Physics results and perspectives,” *Nucl. Instrum. Meth.*, vol. A602, pp. 14–20, 2009.
- [95] G. Riccobene, “Long-term measurements of acoustic background noise in very deep sea,” *Nucl. Instrum. Meth.*, vol. 604, no. 1-2, Supplement, pp. S149–S157, 2009.
- [96] J. Vandenbroucke, G. Giorgio, and N. Lehtinen, “Experimental study of acoustic ultra-high-energy neutrino detection,” *Astrophys. J.*, vol. 621, pp. 301–312, 2005.
- [97] Y. Abdou *et al.*, “Design and performance of the south pole acoustic test setup,” *Nucl. Instrum. Meth.*, vol. 683, no. 0, pp. 78–90, 2012.
- [98] P. B. Price *et al.*, “Temperature profile for glacial ice at the South Pole: Implications for life in a nearby subglacial lake,” *PNAS*, vol. 99, pp. 7844–7847, 2002.
- [99] D. G. Albert, “Theoretical modeling of seismic noise propagation in firn at the South Pole, Antarctica,” *Geophys. Res. Lett.*, vol. 25(23), pp. 4257–4260, 1998.
- [100] S. Boser, *Acoustic Detection of Ultra-High-Energy Cascades in Ice*. PhD thesis, Humboldt Universität, Berlin, 2006.
- [101] B. Semburg *et al.*, “HADES - Hydrophone for Acoustic Detection at South Pole,” *Nucl. Instrum. Meth.*, vol. A604, no. 1-2, Supplement 1, pp. S215 – S218, 2009. Conference ARENA 2008.
- [102] B. Semburg, *HADES - an acoustic sensor for neutrino detection in ice Calibration, characterization and measurements*. PhD thesis, Bergische Universität, Wuppertal, 2011.
- [103] D. Tosi, *Measurement of acoustic attenuation in South Pole ice with a retrievable transmitter*. PhD thesis, Humboldt Universität, Berlin, 2010.
- [104] R. Abbasi *et al.*, “Measurement of sound speed vs. depth in South Pole ice for neutrino astronomy,” *Astropart. Phys.*, vol. 33, pp. 277–286, 2010.

- [105] R. Abbasi *et al.*, “Measurement of Acoustic Attenuation in South Pole Ice,” *Astropart. Phys.*, vol. 34, pp. 382–393, 2011.
- [106] J. Vandenbroucke, *Experimental study of acoustic ultra-high-energy neutrino detection*. PhD thesis, Berkeley University, USA, 2009.
- [107] F. Descamps, *Feasibility of acoustic neutrino detection in ice with the South Pole Acoustic Test Setup*. PhD thesis, Ghent University, Belgium, 2010.
- [108] G. A. Askarian, B. A. Dolgoshein, A. N. Kalinovsky, and N. V. Mokhov, “Acoustic detection of high-energy particle showers in water,” *Nucl. Instrum. Meth.*, vol. 164, pp. 267–278, 1979.
- [109] J. G. Learned, “Acoustic radiation by charged atomic particles in liquids: an analysis,” *Phys. Rev.*, vol. D19, p. 3293, 1979.
- [110] L. R. Sulak *et al.*, “Experimental Results on the Acoustic Detection of Particle Showers,” Presented at Int. Conf. on Neutrino Physics and Astrophysics, Elbrus, USSR, Jun 18-24, 1977.
- [111] T. Bowen, “Sonic particle detection,” *Proceedings of the 23rd ICRC*, vol. 6, pp. 277–282, 1978.
- [112] L. M. Lyamshev, *Radiation acoustics*. CRC press LLC, 2004.
- [113] S. Bevan *et al.*, “Study of the acoustic signature of UHE neutrino interactions in water and ice,” *Nucl. Inst. Meth.*, vol. A607, no. 2, pp. 398–411, 2009.
- [114] L. G. Dedenko *et al.*, “Acoustic signal from neutrinos of ultrahigh-energy and background conditions for an acoustic neutrino telescope in the Ionian Sea,” *Bull. Russ. Acad. Sci. Phys.*, vol. 58, pp. 2075–2077, 1994.
- [115] N. H. Fletcher, *The chemical physics of ice*. Cambridge monographs on physics, 1970.
- [116] M. Choukroun and O. Grasset, “Thermodynamic model for water and high-pressure ices up to 2.2 GPa and down to the metastable domain,” *J. Chem. Phys.*, vol. 127, p. 124506, 2007.
- [117] J. R. Blackford, “Sintering and microstructure of ice: a review,” *J. of Phys.*, vol. D40, no. 21, pp. R355–R385, 2007.
- [118] P. B. Price, “Kinetics of conversion of air bubbles to air hydrate crystals in antarctic ice,” *Science*, vol. 267, no. 5205, pp. 1802–1804, 1995.
- [119] L. Hansen, “Ice crystal structure.” <http://www.iceandclimate.nbi.ku.dk/>, 2012.

- [120] J. G. Weihaupt, “Seismic and gravity studies at the South Pole,” *Geophysics*, vol. 28, pp. 331–359, 1963.
- [121] P. B. Price, “Mechanisms of attenuation of acoustic waves in Antarctic ice,” *Nucl. Instrum. Meth.*, vol. A325, pp. 346–356, 1993.
- [122] D. A. Meese, P. B. Price, and J. Vandenbroucke, “Mechanisms for attenuation of 10-30 kHz acoustic waves at -51°C in glacial ice near South Pole,” *J. Geophys. Res.*, 2009. In preparation.
- [123] T. Karg. Private communication, 2009.
- [124] S. Boll, “A spectral subtraction algorithm for suppression of acoustic noise in speech,” in *Acoustics, Speech, and Signal Processing, IEEE International Conference on ICASSP '79.*, vol. 4, pp. 200 – 203, apr 1979.
- [125] M. Berouti, R. Schwartz, and J. Makhoul, “Enhancement of speech corrupted by acoustic noise,” in *Acoustics, Speech, and Signal Processing, IEEE International Conference on ICASSP '79.*, vol. 4, pp. 208 – 211, apr 1979.
- [126] N. Esfandian and E. Nadernejad, “Quality improvement of speech signals using lpc analysis,” in *Adv. Studies Theor. Phys.*, vol. 2, pp. 673 – 685, 2008.
- [127] T. Karg, “DFT (internal report).” <https://docushare.icecube.wisc.edu/>, 2009.
- [128] F. James and M. Roos, “MINUIT: A System for Function Minimization and Analysis of the Parameter Errors and Correlations,” *Comput. Phys. Commun.*, vol. 10, pp. 343–367, 1975.
- [129] “The ROOT System Home Page.” <http://root.cern.ch/>, 2008.
- [130] L. Wilen, C. Diprinzio, R. Alley, and N. Azuma, “Development, principles, and applications of automated ice fabric analyzers,” *Microscopy Research and Technique*, vol. 62, no. 1, pp. 2–18, 2003.
- [131] J. P. Ralston, D. W. McKay, and G. M. Frichter, “The Ultrahigh-energy neutrino-nucleon cross-section,” 1996.
- [132] J. D. Bjorken and E. A. Paschos, “Inelastic electron-proton and γ -proton scattering and the structure of the nucleon,” *Phys. Rev.*, vol. 185, pp. 1975–1982, Sep 1969.
- [133] D. Heck *et al.*, “Report fzka 6013.” <http://www-ik.fzk.de/corsika/>, 1998.
- [134] V. Bertin and V. Niess, “Acoustic signal computations in the Mediterranean Sea,” *J. Phys. Conf. Ser.*, vol. 81, p. 012019, 2007.

- [135] T. Karg, *Detection of ultra high energy neutrinos with an underwater very large volume array of acoustic sensors: A simulation study*. PhD thesis, Universität Erlangen-Nürnberg, 2006.
- [136] E. Zas, F. Halzen, and T. Stanev, “Electromagnetic pulses from high-energy showers: Implications for neutrino detection,” *Phys. Rev. D*, vol. 45, pp. 362–376, Jan 1992.
- [137] S. Bevan *et al.*, “Simulation of ultra high energy neutrino induced showers in ice and water,” *Astroparticle Physics*, vol. 28, no. 3, pp. 366 – 379, 2007.
- [138] J. Bolmont, “CORSIKA-IW (private communication),” 2008.
- [139] “The IceCube Collaboration: contributions to the 30th International Cosmic Ray Conference (ICRC 2007),” 2007.
- [140] M. Risse and D. Heck, “Energy release in air showers,” *Astropart. Phys.*, vol. 20, p. 661, 2004.
- [141] P. Sokolsky, *Introduction to Ultra High Energy Cosmic Rays*. Addison-Wesley, 1989.
- [142] R. Engel, D. Seckel, and T. Stanve, “<ftp://ftp.bartol.udel.edu/sekel/ess-gzk/>.”
- [143] S. M. Carroll, “The cosmological constant,” *Living Reviews in Relativity*, vol. 4, no. 1, 2001.
- [144] D. Besson, S. Boeser, R. Nahnauer, P. B. Price, and J. A. Vandenbroucke, “Simulation of a hybrid optical / radio / acoustic extension to IceCube for EHE neutrino detection,” *Int. J. Mod. Phys.*, vol. A21S1, pp. 259–264, 2006.